SEMMELWEIS EGYETEM DOKTORI ISKOLA

Ph.D. értekezések

3260.

MOHAMMAD NOUR EDDIN MAHMOUD ALDAHABI

Funkcionális Idegtudományok

című program

Programvezető: Dr. Sperlágh Beáta, egyetemi tanár

Témavezető: Dr. Nusser Zoltán, kutatóprofesszor

Differential Synaptic Vesicle Priming States Determine Synaptic Strength at Hippocampal Glutamatergic Synapses

Ph.D. thesis Mohammad Nour Eddin Mahmoud Aldahabi

János Szentágothai Neurosciences Division Doctoral College, Semmelweis University





Supervisor: Zoltan Nusser, DSc

Official reviewers: Gergely Zachar, PhD

Gábor Molnár, PhD

President of the Complex exam committee: Gábor Gerber, DMD, PhD

Complex examination committee: Zita Puskár, M.D, PhD

Tibor Zelles, PhD

Katalin Schlett, PhD

Budapest, 2025

Table of Contents

L	ist of abbre	viations	5
1.	INTROI	DUCTION	7
	1.1. The	e Hippocampal Formation	7
	1.1.1.	Anatomical Structure	7
	1.1.2.	Circuitry	8
	1.2. Ex	citatory and Inhibitory Neurons of Hippocampal CA1	9
	1.2.1.	CA1 Pyramidal Cells	9
	1.2.2.	Interneuron Diversity	9
	1.3. Hip	ppocampal CA1 Local Network	13
	1.3.1.	Excitatory Input to CA1 PCs	14
	1.3.2.	Inhibitory Input to CA1 PCs	14
	1.4. Syn	naptic Transmission	16
	1.5. Syn	naptic Strength and Short-Term Plasticity	17
	1.5.1.	Postsynaptic Target Cell Type-Dependent Differences in Sh	ort-Term
	Plasticity	y	18
	1.5.2.	Functional Roles of STP in Hippocampal Networks	19
	1.6. Ex	ocytosis of Synaptic Vesicles	19
	1.6.1.	The Molecular Bases of Synaptic Vesicles Docking/Priming	19
	1.6.2.	Docking & Priming of SVs is a Dynamic Process	22
	1.6.3.	The Molecular Bases of Synaptic Vesicle Fusion	23
	1.6.4.	The Role of Voltage-Gated Ca ²⁺ Channels in SV Fusion	24
	1.6.5.	The Sequential Two-Step Priming Model	26
2.	OBJECT	ΓIVES	28
	2.1. Dis	stinct Localization of Molecules in Post- and Presynaptic Compart	tments in
	a Target Co	ell Type-Dependent Manner	28

2.2.2.2.1		Different Effective [Ca ²⁺] Reaching Docked SVs
		. Differential Presynaptic Action Potential-Evoked [Ca ²⁺] Influx 29
	2.2.2	2. Differential Coupling Distances Between Presynaptic VGCCs and the Sensors of SV Fusion
	2.3.	Differential Occupancy of RSs by SVs
	2.4.	Differential Priming State of Docked SVs
3.	. M ET	THODS32
	3.1.	Animals
	3.2.	Virus Injection
	3.3.	Slice Preparation
	3.4.	Electrophysiological Recordings
	3.5.	Pharmacological Manipulation
	3.6.	Perforated Patch-Clamp Recordings
	3.7.	Two-Photon Laser Scanning Microscopy
	3.8.	Tissue Processing After Paired Whole-Cell Patch-Clamp Recordings 36
	3.9.	Multiplexed Postembedding Immunolabeling
	3.10.	EM Tomography
	3.11.	SDS-Digested Freeze-Fracture Replica Labelling
	3.12.	Modelling Short-Term Plasticity
	3.13.	Parameter Optimization for the PC – O-LM IN Connections
4.	RES	ULTS39
	4.1.	Differential Synaptic Strength and STP Patterns from CA1 PC – FSIN vs PC –
	O-LM	IN
	4.2. Dendri	Munc13-2 Selectively Localizes to Synapses Targeting mGluR1α+- tes
	4.3.	Munc13-2 Puncta Disappear in the Stratum Oriens of Elfn1 Knock out
	Mice	43

	4.4.	Conditional Knock out of Munc13-2 Does not Affect mGluR7 Expression 45	
	4.5. Knocking out Elfn-1 Increases eEPSCs at PC – O-LM IN Connec		
	Munc	3-2 Has no Obvious Role in Regulating Pv at These Synapses	
	4.6. Target	Larger Densities of VGCCs Surround Release Sites in FSIN versus O-LM IN-	
	4.7.	Differential [Ca ²⁺] Influx is not the Primary Driver of Synaptic Strengthences	
	4.8. Promin	Differential Synaptic Vesicle Priming States Impact Release Probability More nently	
	4.8.1 IN	1. Similar Docked Vesicles Densities in AZs Innervating FSIN and O-LM	
	4.8.2 PC -	2. Differential Effect of PDBU Indicates Distinct Priming in PC – FSIN vs - O-LM IN Synapses	
	4.9. Differe	Modeling Both Synapses by a Two-Step Priming Model Highlights Their ences	
	4.9.	1. Short-Term Plasticity Characterization at PC – FSIN Connections 61	
	4.9.2 Mod	2. Modeling PC – FSIN Synapses with a Sequential Two-Step Priming lel	
	4.9.3	3. Short-Term Plasticity at PC – O-LM IN Synapses	
	4.9.4 Very	4. Modeling Synaptic Transmission at PC – O-LM IN Connections Suggests v Low Occupancy of Release Sites by Well-Primed SVs	
5	. DIS	CUSSION70	
	5.1. Postsy	Distinct Localization of Presynaptic Munc13-2 and mGluR7 in an Elfn1 naptic-Dependent Manner	
	5.2.	[Ca ²⁺] Influx Is Not the Primary Determinant of Pv	
	5.3.	The Priming State of SVs Has a Greater Impact on Pv	
	5.4.	Munc13-1 as a Prominent Molecule Regulating Pv	

	5.5.	Three Model Parameters Sufficient to Transform PC – FSIN into PC – O-L	M		
	IN Mo	N Model			
	5.6.	Modeling Captures Slightly Lower P_{fusion} at $PC-O\text{-LM}$ IN Connections	75		
	5.7.	Modeling Shows Larger Proportion of Well-Primed SVs at PC - FS	IN		
	Compa	ared to PC – O-LM IN Connections	75		
	5.8.	STF at PC – O-LM IN Synapses	76		
	5.9.	What Are the Structural Correlates of SVs in LS and TS?	76		
6.	CON	ICLUSIONS	78		
7.	SUM	1MARY	79		
8.	REF	ERENCES	81		
9.	BIB	LIOGRAPHY OF PUBLICATIONS1	03		
	9.1.	Publications Related to the Thesis:1	03		
	9.2.	Publications Not Related to the Thesis:1	03		
1(). ACK	NOWLEDGMENTS1	04		

List of abbreviations

4-AP 4-aminopyridine **GTA** Grand total average **AAC** Axo-axonic cells HVA High-voltage-activated **ACSF** Artificial cerebrospinal fluid IN Interneuron AIS **IPSC** Inhibitory post synaptic current Axon initial segment AP Action potential LS Loosely docked and primed state ΑZ Active zone LVA Low-voltage-activated **BSA** Bovine serum albumin MWU test Mann-Whitney U-test CA Cornu ammonis **NND** Nearest neighbor distance **CCK** Cholecystokinin O-LM IN Oriens-lacunosum **CCKBC** Cholecystokinin-expressing moleculare interneuron basket cells PC Pyramidal Cell Chrna2 Nicotinic acetylcholine receptor α2 subunit **PDBU** Phorbol 12,13-dibutyrate CNS Central nervous system PF Protoplasmic plasma membrane face DG Dentate Gyrus Pfusion Synaptic vesicle fusion EC Entorhinal cortex probability EF Extracellular plasma membrane PIP Phosphatidylinositol phosphate face **PM** Plasma membrane Elfn1 Extracellular leucine-rich repeat fibronectin containing 1 protein Probability that docking site is P_{occ} occupied by synaptic vesicles \mathbf{EM} Electron microscopy PPR Paired-pulse ratio **EPSC** Excitatory post synaptic current PTP Post-tetanic potentiation **FSIN** Fast-spiking interneurons

P_{TS}	Proba	Probability that an SV in tightly		ΓD Short-term depression		
	docked state		STF	Short-term facilitation		
• •		naptic vesicle release		Short-te	Short-term plasticity	
PV Parva		-	str.	Stratum	Stratum	
		ilbumin	SV	Synaptic vesicles		
PVBC Parvalbumin-expressing basket cell			TS	Tightly docked and primed state		
		nteracting molecule	TSL	Labile tightly docked and		
		RIM binding proteins	VAM	-	primed state Vesicle-associated	
RMSI	D	Root-mean-square deviation Release site			membrane protein 2	
RS	Releas			C	Voltage gated Ca ²⁺ channel	
SDS-I	FRL	SDS-digested freeze- fracture replica	vGluT2 VIAAT VIP Vasoa		Vesicular glutamate transporter-2	
SNAP	P-25	Synaptosomal-associated protein 25			Vesicular inhibitory amino acid transporter	
SNAF	RE	Soluble NSF attachment protein receptor			tive intestinal peptide	
SST	Soma	tostatin				

1. INTRODUCTION

This thesis starts with a broad overview of the hippocampus, including its structure and neural circuits. It then focuses on the neuron types found in the CA1 region of the hippocampus, the area of focus for this research. Finally, the introduction will delve into synaptic transmission and its molecular mechanisms, providing the necessary background for the investigation into the functional differences between a strong and weak glutamatergic synapse formed by CA1 pyramidal cells (PCs).

1.1. The Hippocampal Formation

The hippocampal formation, located within the medial temporal lobe of the brain, is a complex network composed of millions of neurons. Information flows unidirectionally through its distinct subfields, which include the dentate gyrus (DG), hippocampus proper, subiculum, presubiculum, parasubiculum, and entorhinal cortex (EC) (1). This basic cellular organization and fiber pathway is largely conserved across mammalian species (1). Research has established the hippocampal formation's crucial role in various cognitive functions, including spatial memory (2), episodic memory (3), cognitive map formation (1) and attentional control (4).

1.1.1. Anatomical Structure

The hippocampus's characteristic shape comes from the layered structure of the DG and

cornu ammonis (CA; Figure 1). The DG has three layers: a sparsely populated molecular layer, a densely packed granule cell layer (containing principal cells), the the and polymorphic cell layer (hilus) enclosed by the V or U-shaped granule cell layer (5). The CA, as seen in Figure 1, is a continuous layer of PCs, is divided into CA1, CA2, and CA3, with CA1 having the most

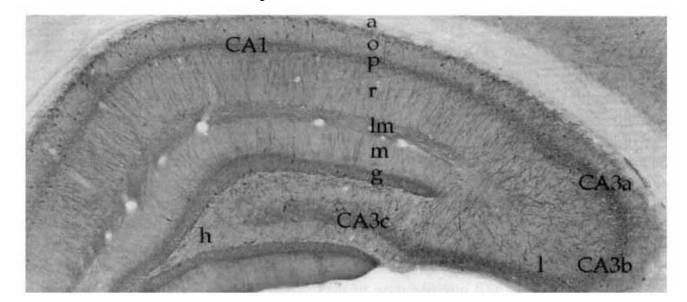


Figure 1: Coronal section through the dorsal hippocampus, immunostained for parvalbumin. o, CA1 stratum oriens; p, stratum pyramidale; r, stratum radiatum; lm, stratum lacunosum-moleculare; m, dentate molecular layer (stratum moleculare); g, granule cell layer; h, hilus proper; l, stratum lucidum; CA3a-c, subregions of the CA3 field. Adopted from (7).

densely packed PCs. The pyramidal cell layer (stratum pyramidale) is surrounded by

stratum (str.) oriens, a less dense layer containing inhibitory interneurons (INs) and the basal dendrites of the PCs. The alveus, a thin fiber layer, lies outside the str. oriens. On the other side of the PC layer is the str. radiatum, containing the PCs' apical dendrites and where the interconnections between CA3 PCs and CA3 to CA1 (Schaffer collaterals) occur (*Figure 2*). The most superficial portion of the hippocampus is known as the str. lacunosum-moleculare, where fibers from the EC innervate the distal dendrites of CA1 PCs (*Figure 2*) (5). In CA3 only (not CA1 or CA2), the str. lucidum is present (*Figure 1*). This is where mossy fibers from granule cells innervate CA3 PCs (1). Various inhibitory INs are found in all layers (strata) (6–8).

1.1.2. Circuitry

Input from the neocortex enters the hippocampus primarily through the EC, specifically its layers II and III (Figure 2), which are thus considered the initial stage of hippocampal processing of sensory information. Layer II of the EC projects via the perforant pathway to both the DG and CA3, while layer III projects to the subiculum and CA1. The former initiates the trisynaptic loop which starts with: (1) DG granule cells project via mossy fibers to CA3 PCs; (2) CA3 PCs project via Schaffer collaterals

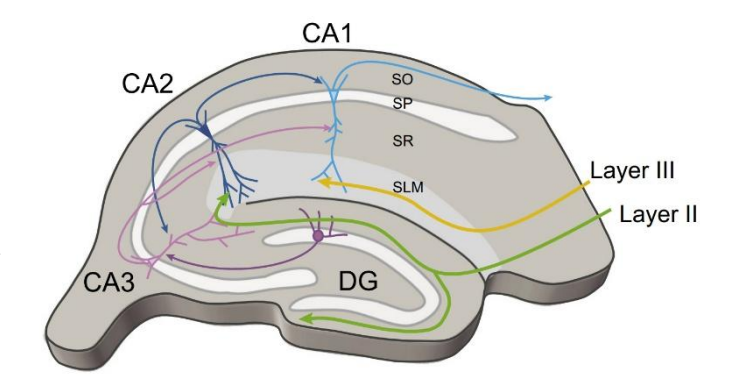


Figure 2: This diagram illustrates the primary excitatory circuitry within the hippocampus. The entorhinal cortex serves as the main source of input, with layer II (green) projecting to both the dentate gyrus (DG) granule cells (purple) and the distal apical dendrites of CA3 (pink) and CA2 (dark teal) pyramidal neurons. The DG granule cells then relay this information to CA3 via the mossy fibers. CA3 pyramidal neurons, in turn, connect to both CA2 and CA1 (blue) pyramidal neurons through the Schaffer collaterals. CA1 also receives direct input from layer III of the entorhinal cortex (yellow). Adopted from (9).

to CA1 PCs; and (3) CA1 PCs project to the subiculum and deep layers of the EC, completing the loop (*Figure 2*). This unidirectional flow distinguishes the hippocampal circuit from the reciprocal connectivity observed in the neocortex (1, 7). The CA1 region of the hippocampus is one of the most extensively studied and relatively simple cortical areas, offering valuable insights into neuronal and synaptic diversity.

1.2. Excitatory and Inhibitory Neurons of Hippocampal CA1

1.2.1. CA1 Pyramidal Cells

Within the CA1 region, PCs exhibit heterogeneity, notably a clear subdivision between deep and superficial CA1 PCs exist along the radial axis (perpendicular to the CA1 PC layer), an observation made by early anatomists (10). Beyond this positional distinction, CA1 PCs display differences in neurogenesis timing, molecular composition, structure, and physiological properties (11):

- 1. Superficial layer PCs, located near the str. radiatum, are characterized by their dense packing and distinct expression of neurochemical markers, such as calbindin and zinc (8, 12, 13). Notably, these PCs also exhibit a larger somatic *h*-current, which contributes to a depolarizing sag (13).
- 2. Deeper PCs, located closer to the str. oriens, do not express calbindin (8, 12, 13), possess larger soma, and originate earlier during embryonic neurogenesis compared to superficial CA1 PCs (14).

The radial heterogeneity described is further compounded by spatial gradients that occur along the dorsoventral (15) and proximodistal (16) axes of the hippocampus.

CA1 PCs innervate a variety of target cells, including local INs, subicular pyramidal cells (17), and numerous extrahippocampal regions such as the hypothalamus, thalamus, amygdala, prefrontal cortex, retrosplenial cortex, and septum (18–20).

In rats, a single CA1 PC receives approximately 30,000 excitatory and 1,700 inhibitory synaptic inputs. The quantity, relative proportion, strength and spatial distribution of these inputs influence synaptic integration and ultimately determine the output of the PCs, namely the generation of action potentials (21). These CA1 PCs are modulated by a diverse population of GABAergic INs that provide both general inhibition and precise temporal control of PCs activity.

1.2.2. Interneuron Diversity

Within the hippocampus, diverse GABAergic INs are distributed across all layers. In the CA1 region alone, at least 21 distinct IN subtypes exist (*Figure 3*), each targeting specific subcellular compartments of the PCs and exerting inhibitory control within discrete temporal windows (8).

These INs are classified based on a combination of anatomical features (including soma location and dendritic/axonal arborization), the subcellular domains of PCs they innervate, their molecular expression profiles, and their intrinsic electrophysiological properties (22). The most well-known examples of CA1 INs are:

- Basket cells
- Bistratified cells
- Axo-axonic or Chandelier cells
- IN selective INs
- Oriens-lacunosum moleculare cells

Basket cells are named for their characteristic axonal arborization, which forms basket-like structures of synaptic boutons around the soma and proximal dendrites of PCs (23, 24). These cells are categorized as either parvalbumin-expressing (PVBCs; *Figure 3 (type 2)*) or cholecystokinin-expressing basket cells (CCKBCs; *Figure 3 (type 3 & 4)*). PVBCs constitute approximately 14% (around 5,530 cells) of CA1 INs, representing 1.5% of all CA1 neurons (25). Notably, PVBCs predominantly target CA1 PCs (99% of their output synapses), with a single basket cell capable of inhibiting between 1,500 and 2,500 PCs in this region (7, 25, 26).

Cholecystokinin-expressing basket cells (*Figure 3 (type 3 & 4)*) constitute approximately 9% (around 3,600 cells) of all CA1 hippocampal INs, representing 1% of the total CA1 neuronal population (25). Sharing similar anatomical characteristics with PVBCs, CCKBCs exhibit a preference for perisomatic axonal arborizations, targeting the soma and proximal dendrites of PCs (27). However, they are estimated to contact roughly half the number of PCs compared to PVBCs, approximately 1,250 (25, 28). While PVBC somata are typically located within or adjacent to the str. pyramidale (str. oriens and str. radiatum), CCKBC somata are predominantly found in the str. radiatum, with a notable concentration at the str. lacunosum-moleculare border and fewer present in the str. pyramidale and str. oriens (23, 28-30). CCKBCs are molecularly classified into at least two distinct subtypes: those characterized by the coexpression of vasoactive intestinal peptide (VIP; Figure 3 (type 3)) and those identified by the coexpression of vesicular glutamate transporter 3 (Figure 3 (type 4)) (31,32).

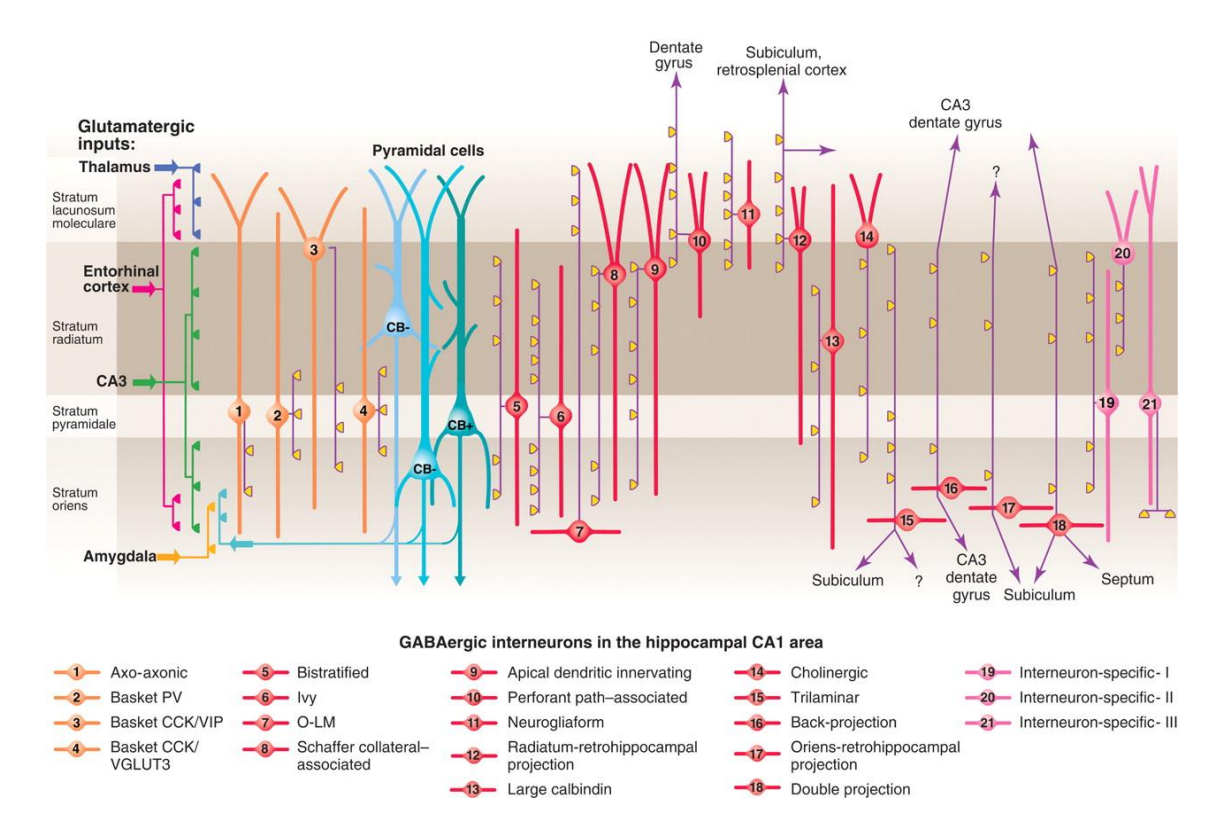


Figure 3: Pyramidal cells are accompanied by at least 21 classes of interneuron in the hippocampal CA1 area.

The main terminations of five glutamatergic inputs are indicated on the left. The somata and dendrites of interneurons innervating pyramidal cells (blue) are orange, and those innervating mainly other interneurons are pink. Axons are purple; the main synaptic terminations are yellow. Note the association of the output synapses of different interneuron types with the perisomatic region (left) and either the Schaffer collateral/commissural or the entorhinal pathway termination zones (right), respectively. VIP, vasoactive intestinal polypeptide; VGLUT, vesicular glutamate transporter; O-LM, oriens-lacunosum moleculare. Adopted from (8).

Bistratified cells are characterized by their axonal projections (*Figure 3 (type 5)*), which extend both above and below the str. pyramidale, innervating the basal and apical dendrites of PC in the str. oriens and str. radiatum, respectively (24, 33). These INs comprise approximately 6% (around 2,200 cells) of the CA1 INs population (25). The majority of bistratified IN somata (almost 70%) are located within the str. pyramidale, with approximately one quarter residing in the str. oriens and a small percentage found in the str. radiatum (24). Individual bistratified INs innervate approximately 1,600 PCs, forming 5-10 synapses with each target cell (24). Representing approximately 25% of parvalbumin (PV)-expressing hippocampal INs (34), bistratified cells differ from PVBCs by their potential co-expression of somatostatin (SST) and neuropeptide Y (NPY) (33–35).

Axo-axonic cells (AACs; *Figure 3 (type 1)*), also known as chandelier cells due to their distinctive axonal arborizations resembling candlesticks, constitute approximately 4% (around 1,500 cells) of CA1 hippocampal INs (25). Their dense axonal arborization within the str. pyramidale and superficial str. oriens exclusively targets the axon initial segment (AIS) of up to approximately 1,200 PCs (36–38). The primary axonal branches of AACs run horizontally along the str. pyramidale border, emitting vertical collaterals that form 2-15 boutons innervating the AIS of PCs (37). This unique AIS targeting is thought to provide highly effective inhibition of AP initiation in PCs (39, 40). Parvalbumin expression is a key molecular marker for hippocampal AACs (34, 41).

Within the CA1 str. pyramidale, PV-containing cells consist of approximately 60% basket cells, 25% bistratified cells, and 15% AACs (34). Parvalbumin-positive INs (PV+ INs) are frequently categorized as "fast-spiking" cells (FSINs) because of their capacity to maintain high-frequency action potential (AP) firing with minimal spike-frequency adaptation or accommodation (42, 43). This rapid firing is primarily attributed to their perisomatic expression of Kv3 type voltage-gated K⁺ channels, which facilitate rapid repolarization (43, 44). This fast-spiking phenotype enables these INs to exert precise and potent inhibitory control, playing a critical role in modulating neuronal excitability and network oscillations within the hippocampus (7).

While cholecystokinin (CCK) is expressed in CCKBCs, it is also present in a diverse population of dendrite-targeting INs that primarily innervate principal cell dendrites. These INs constitute 3-5% (approximately 1,500 cells) of CA1 INs (25), residing predominantly in the str. radiatum, with some concentration near the str. radiatum/str. lacunosum-moleculare border (27, 29, 30, 45). Among these are Schaffer collateral-associated cells (*Figure 3 (type 8)*), whose axonal projections overlap with the CA3 Schaffer collateral input to the CA1 region. Schaffer collateral-associated cells exhibit extensive arborization in the str. radiatum and, to a lesser extent, in the str. oriens, targeting the oblique and basal dendrites of PCs (23, 27, 29). In contrast, apical dendrite-innervating INs (*Figure 3 (type 9)*) selectively innervate the main apical shaft of PCs, avoiding the oblique and basal dendrites (30). Perforant path-associated cells (*Figure 3 (type 10)*) represent another distinct group, with axons that overlap with the EC input within the str. lacunosum-moleculare, specifically targeting the distal apical tufts of CA1 PCs (30, 45).

While the majority of the aforementioned INs primarily target PCs, a separate class, known as "interneuron-selective interneurons" (*Figure 3 (type 19-21)*), predominantly innervates the dendrites and soma of other, dendrite-targeting INs (24, 46), thereby establishing a disinhibitory circuit (47). These interneuron-selective interneurons commonly express the calcium-binding proteins calretinin or VIP (46).

The oriens-lacunosum moleculare (O-LM) IN (Figure 3 (type 7)), first described by Lacaille et al. (1987), is characterized by a distinctive anatomical organization (48). In the CA1 region, O-LM cell somata and dendrites are confined to the str. oriens and alveus, while their axons ascend with minimal branching through the str. pyramidale and str. radiatum, terminating in a prominent arborization within the str. lacunosum-moleculare. Approximately 7% of the O-LM IN axon remains in the str. oriens, with over 90% extending into the str. lacunosum-moleculare, forming symmetrical synapses with the distal apical dendrites of PCs (26, 49). O-LM INs constitute about 4.5% (approximately 1,650 cells) of the total hippocampal CA1 IN population (25). This unique morphology positions O-LM INs to function within a classic feedback inhibitory circuit. The specific location of their somata and horizontal dendrites dictates that they primarily receive excitatory input from CA1 PCs, subsequently distributing inhibitory signals back to the distal apical dendritic tufts of these same PCs in the str. lacunosum-moleculare. This arrangement effectively modulates excitatory input from the EC and nucleus reuniens to CA1 PCs (50–53). Each O-LM IN is estimated to contact around 1,450 PCs, forming an average of approximately 10 synapses per connection (25, 26). Mature O-LM INs express SST, although SST expression is not exclusive to O-LM INs; some bistratified INs also express SST, and O-LMs only represent about 40% of SST-expressing INs. O-LM cells are further identified by the expression of metabotropic glutamate receptor 1a (mGluR1α), and somato-dendritic labeling for the extracellular leucine-rich repeat fibronectin containing 1 protein (Elfn1) (35, 54–56). Selective targeting of O-LM INs has been achieved using a driver line based on nicotinic acetylcholine receptor α2 subunit promoter activity (Chrna2-Cre mice) (53, 57).

1.3. Hippocampal CA1 Local Network

The ultimate activity of CA1 PCs is governed by the balance and temporal integration of the excitatory and inhibitory inputs they receive. CA1 PC dendrites, which extend across multiple strata from the str. oriens to the str. lacunosum-moleculare, receive both excitatory and inhibitory inputs. The following sections will discuss some of these inputs, their innervation patterns along the CA1 PC dendritic tree, and the underlying circuitry.

1.3.1. Excitatory Input to CA1 PCs

CA1 pyramidal cells receive excitatory input primarily from two sources: the Schaffer collaterals/commissural fibers originating from CA3 PCs (58) and the entorhinal fibers projecting from layer III pyramidal cells of the EC (*Figure 2*) (59). It was also found that CA1 PCs innervate each other, but this is less prominent (60). The Schaffer collaterals and commissural fibers from CA3 PCs innervate CA1 PC dendrites within the str. oriens and str. radiatum, with up to 92% of *in vivo*-labeled CA3 PC axons predominantly targeting dendritic spines of CA1 PC (61). While the majority of perforant pathway entorhinal fibers terminate in the str. lacunosum-moleculare, a smaller subset reaches this region via the alveus and str. oriens, forming the alvear pathway (62). Within the str. lacunosum-moleculare, entorhinal cortical boutons target primarily PC dendritic spines and shafts, comprising up to 90% of the connections (61). Furthermore, CA1 PCs receive additional input via synapses on their distal apical dendrites from the nucleus reuniens of the thalamus and the basolateral nucleus of the amygdala (63–66).

1.3.2. Inhibitory Input to CA1 PCs

As previously noted, CA1 PCs are subject to a diverse array of GABAergic INs that provide inhibitory control across all PC compartments, from basal dendrites to distal apical tufts. These INs orchestrate temporal regulation of PC activity through dynamic timing of synaptic interactions, contributing to distinct brain states and cognitive processes (8).

Some of these INs are excited by extrinsic sources, resulting in feedforward inhibition of CA1 PCs. Others receive excitatory input from local CA1 PCs, forming feedback inhibitory circuits. Importantly, some IN subtypes can participate in both feedforward and feedback inhibition, receiving input from both extrinsic sources and local CA1 PCs. This flexibility enhances the dynamic range of inhibition and enables the hippocampus to respond to diverse inputs and behavioral demands.

1.3.2.1. Feedforward Inhibitory Input

Parvalbumin-positive and somatostatin-positive INs are the most abundant and functionally significant IN subtypes in the cerebral cortex, including the hippocampus (7, 67, 68). CA1 PCs and PV+ INs share excitatory input from sources such as CA3 PCs, the EC, the medial septum, and the subiculum. Although CA1 SST+ INs also receive inputs from these sources, tracing data indicate that SST+ cells receive predominantly excitatory connections within CA1 and limited input from CA3 or EC (69–71). Activation of CA1 PCs and these INs results in feedforward inhibition of CA1 PCs (72, 73). PV+ INs receive significantly stronger excitatory input from CA3 PCs, the EC, and the medial septum compared to SST+ INs (71). Thus, compared with SST+ cells, PV+ inhibitory cells are a primary mediator of feedforward inhibition from longer-distance input sources. This feedforward inhibition narrows the time window within which excitatory inputs summate to reach the threshold for spike generation. In rat hippocampal CA1 PCs, this window has been shown to be very narrow (less than 2 ms), caused by the short delay with which disynaptic feedforward inhibition follows monosynaptic excitation (72).

1.3.2.2. Feedback Inhibitory Input

Recurrent collaterals from CA1 PCs preferentially innervate INs within the str. oriens and alveus, forming 54% of their local synaptic connections with these INs (61). Conversely, INs are estimated to make approximately 92% of their GABAergic synapses onto PCs (25). This reciprocal connectivity establishes a feedback inhibitory circuit that regulates PC firing and prevents excessive excitation. Chronic silencing of CA1 PC transmission using Cre-dependent expression of tetanus toxin light chain has been shown to significantly reduce this feedback inhibition, consequently impacting the power, duration, and intrinsic frequency of ripple oscillations (74).

Both PV+ and SST+ INs receive excitatory input from CA1 PCs. Therefore, in addition to mediating feedforward inhibition, PV+ INs also provide feedback inhibition to PCs. As previously mentioned, PV+ IN subtypes (PVBC, bistratified, and AAC) target distinct PC subcellular domains. These diverse IN classes are also known to fire APs in precise temporal patterns during hippocampal network oscillations, thereby inhibiting different PC domains in an oscillatory phase-locked manner (33, 75–78). PV+ INs exert a potent

and rapid inhibitory influence on PC firing, and the high-frequency firing capacity of PV+ FSINs enables rapid and efficient PC inhibition.

Somatostatin-positive INs tend to target the dendrites of PCs. For instance, O-LM INs innervate the apical dendrites of CA1 PCs in the str. lacunosum-moleculare, in close proximity to EC input (51). Consequently, these INs modulate synaptic integration in the apical dendrites through feedback inhibition. Given that local CA1 PC collaterals provide the majority of input to O-LM INs (at least 75%) (51), this form of inhibition requires sufficient activity in the Schaffer collaterals to activate CA1 PCs, which then excite O-LM INs. This, in turn, can limit the effectiveness of EC afferents in driving the same population of PCs (51, 53).

PV+ and SST+ INs function synergistically to regulate the balance of excitation and inhibition within the CA1 network, shaping the timing, precision, and synchrony of neuronal activity (50, 74).

Signal transduction between these neurons primarily occurs through chemical synapses, highlighting their importance in neuronal information processing. This thesis will focus on the synaptic transmission and mainly the connections between CA1 PCs and FSINs, as well as those between PCs and O-LM INs.

1.4. Synaptic Transmission

Synaptic transmission mediates signal transduction between neurons. The foundational mechanisms and time course of this process were initially described approximately 70 years ago by Bernard Katz and his colleagues. Their "quantal hypothesis of neurotransmission" proposed that neurotransmitter is released in discrete, all-or-none units, termed quanta (79). This hypothesis posited that neurotransmitter is released in multiples of a fundamental packet, or quantum, which was subsequently identified as corresponding to the release of individual synaptic vesicles (SVs).

Upon arrival of an AP at the nerve terminal, voltage-gated Ca²⁺ channels (VGCC) open, leading to a localized, transient increase in intracellular Ca²⁺ concentration at the active zone (exceeding 1000-fold), creating what are termed [Ca²⁺] nanodomains (80). This elevated [Ca²⁺] triggers the fusion of SVs at the AZ within a few hundred microseconds (81), releasing neurotransmitters into the synaptic cleft. The released neurotransmitter

molecules bind to ionotropic postsynaptic receptors (e.g. AMPA, NMDA and kainite receptors in the central nervous system [CNS] for Glutamate or GABA_A receptors for GABA), increasing their opening probability and generating excitatory or inhibitory postsynaptic currents (EPSCs or IPSCs, respectively). The amplitude of the postsynaptic current is determined by the number of presynaptic vesicles released, the amount of neurotransmitter per vesicle, the number and conductance of postsynaptic ionotropic receptors, and the open probability of the receptors.

1.5. Synaptic Strength and Short-Term Plasticity

Synaptic efficacy, intuitively defined as the capacity of a presynaptic input to influence postsynaptic output (82), reflects the strength of communication between neurons. It is primarily determined by the probability and amount of neurotransmitter released from the presynaptic neuron, and the number of postsynaptic receptors activated. Synaptic efficacy can be considered a function of these two factors (79, 83–85). These synaptic parameters are subject to activity-dependent dynamic changes, a phenomenon known as synaptic plasticity, which can manifest across different timescales, including short-term and long-term plasticity. Short-term plasticity (STP), initially described by Del Castillo and Katz at the neuromuscular junction, is a use-dependent plastic process exhibiting either facilitation or depression (79). Several forms of STP have been identified in the central nervous system (86):

- 1. Short-term depression (STD) occurs when two closely timed presynaptic stimuli elicit a smaller second postsynaptic response, with this depression lasting from hundreds of milliseconds to seconds.
- Short-term facilitation (STF), conversely, involves a larger second response to a closely following stimulus, with effects also lasting hundreds of milliseconds to seconds.
- 3. Post-tetanic potentiation (PTP)/Augmentation refers to the sustained enhancement of synaptic transmission following high-frequency presynaptic stimulation, with effects lasting from tens of seconds to minutes.

1.5.1. Postsynaptic Target Cell Type-Dependent Differences in Short-Term Plasticity

Three decades ago, it was demonstrated that a single motor neuronal axon can form synapses of varying strength and exhibit distinct STP patterns depending on the specific postsynaptic muscle target (87). Similar postsynaptic target cell type-dependent differences in STP have also been observed in the rodent CNS (52, 88–92). For example, in the cerebellum, granule cell parallel fibers show sustained facilitation when synapsing onto Purkinje or stellate cells, but when synapsing onto basket cells, it displays STD following initial paired-pulse facilitation (*Figure 4B*) (93).

Similarly, in the neocortex and hippocampus, PCs form strong synapses with high probability of SV release (Pv) and STD when innervating PV-expressing FSINs. In

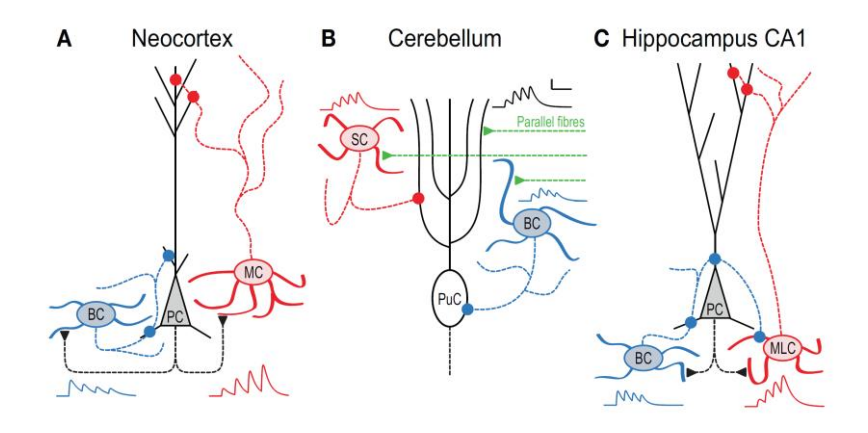


Figure 4: Target-cell specific STP remaps spiking across the somato-dendritic axis in local circuits.

- (A) In cortical circuits, pyramidal cell (PC) inputs to basket cells (BCs) exhibit short-term depression, while those to Martinotti cells (MCs) are facilitating (95). Consequently, high-frequency PC firing (251, 252) activates MCs later than BCs. BCs then innervate PCs perisomatically (Buchanan et al., 2012), whereas MCs primarily contact the apical dendrite (253).
- **(B)** In the cerebellum, parallel fiber (PF) synapses onto Purkinje cells (PuC) and stellate cells (SC) both facilitate. Conversely, PF connections to BCs depress. This differential STP causes high-frequency PF activity to activate SCs later than BCs, resulting in early-onset somatic inhibition and late-onset dendritic inhibition of PuCs (93).
- (C) Within the hippocampus, CA1 PCs connect to two distinct IN types with contrasting STP. Onsettransient BCs receive depressing input and target PCs perisomatically, while late-transient O-LM INs (Martinotti-like cells [MLC]) receive facilitating input and target dendrites. Therefore, during 50 Hz firing, the inhibition of PCs shifts from somatic to dendritic compartments (50). All synaptic traces presented were simulated based on data from (50, 93, 254). This figure was adopted from (255).

contrast, when the same PC axons innervate SST-expressing IN, such as Martinotti cells

in the neocortex and the mGluR1 α -expressing O-LM IN cells in the hippocampus, they form weak synapses with low Pv and STF (Figure 4A & C) (52, 88–92, 94, 95). This differential target cell type-dependent Pv and STP at hippocampal PC – O-LM IN and PC – FSIN synapses will be investigated in this study.

1.5.2. Functional Roles of STP in Hippocampal Networks

Functional synaptic heterogeneity expands the computational capabilities of neuronal networks, enabling neurons to communicate through multiple forms of synaptic plasticity and Pv. This allows individual neurons to transmit a diverse array of signals within the network (96, 97). For example, the differential STP and excitatory input from CA1 PCs onto distinct IN subtypes facilitates a rapid shift in recurrent inhibition from the soma to the apical dendrites of these PCs ($Figure\ 4C$). This shift is achieved through the sequential recruitment of two inhibitory circuits: one involving "onset-transient" INs, such as FSINs, which respond to the onset of AP trains due to the depressing input from CA1 PCs and inhibit the somatic and perisomatic regions of these PCs; the other involving "late-persistent" INs, such as O-LM INs, which are activated in proportion to the AP firing rate due to the facilitating input received from CA1 PCs and thus shifting the inhibition to the distal apical dendrites (50). The molecular mechanisms underlying differences in Pv and STP necessitate a deeper understanding of the SV exocytosis process, which will be addressed in the following section.

1.6. Exocytosis of Synaptic Vesicles

Synaptic signaling between nerve cells is initiated by the presynaptic exocytosis of neurotransmitter-containing SVs, a process mediated by the sequential steps of SV tethering, SV priming and concurrent membrane attachment (docking) at the AZ, and Ca²⁺-triggered SV fusion. Over the past three decades, key proteins regulating SV exocytosis have been identified. These proteins govern the functional processes of SV docking/priming and the fusion of these SVs with the plasma membrane (PM) upon Ca²⁺ influx (98).

1.6.1. The Molecular Bases of Synaptic Vesicles Docking/Priming

Over 2,000 proteins contribute to synapse formation and function (99). While the precise number of proteins involved in SV exocytosis remains unknown, many of the complex

molecular interactions underlying SV docking/priming and subsequent Ca²⁺-triggered fusion have been identified. Neuronal SNARE (soluble NSF attachment protein receptor) proteins are crucial for exocytosis, including syntaxin-1, SNAP-25 (synaptosomal-associated protein 25), and synaptobrevin-2/VAMP2 (vesicle-associated membrane protein 2; *Figure 5*). These SNARE proteins are considered the engine of membrane fusion (100). Synaptobrevin-2 and syntaxin-1 each possess a transmembrane region that anchors them to the SV membrane and the presynaptic AZ membrane, respectively (100, 101). The assembly of these three SNARE molecules forms a *trans*-ternary SNARE complex, which "zips" together, bringing the SV and AZ plasma membranes into close proximity (98). For precise and efficient fusion, this SNARE assembly is regulated by four key proteins: Munc18 and Munc13, which ensure proper SV priming (102); and synaptotagmin-1 (103, 104) and complexin (105, 106), which control the synchronized SV fusion triggered by Ca²⁺ (*Figure 5*).

Knocking out either Munc18 or Munc13 abolished SV priming and SV release (107–111) demonstrating their essential roles in SV exocytosis. These molecules collaborate to facilitate proper SNARE complex assembly. Munc18, by capturing free syntaxin-1 (102, 112, 113), prepares the environment for Munc13 to catalyze the transition from a closed Syntaxin-Munc18 conformation to a tripartite Munc18-1/syntaxin-1/Munc13 complex (102, 114, 115). Subsequently, Munc13 directly interacts with and recruits synaptobrevin-2 and SNAP-25, forming a functional *trans*-ternary SNARE complex (102, 116, 117), promoting the eventual formation of the SNARE-synaptotagmin-complexin complex (118, 119). This complex renders the SV fusion-competent and capable of synchronous release (Figure 5). Beyond its priming function, Munc13 also prevents SV de-priming by mitigating the NSF and α -SNAP-mediated inhibition of fusion (113, 120, 121). Furthermore, Munc13 is a component of a protein complex involving RIM (Rab interacting molecule) protein. In this complex, RIM coordinates three distinct functions: 1) binding to vesicular Rab proteins, mediating vesicle docking; 2) binding to the central priming factor Munc13, activating priming; and 3) binding to the Ca²⁺ channel, both directly and indirectly through RIM-BP (RIM binding proteins), positioning Ca²⁺ channels in close proximity to the docked vesicle (98).

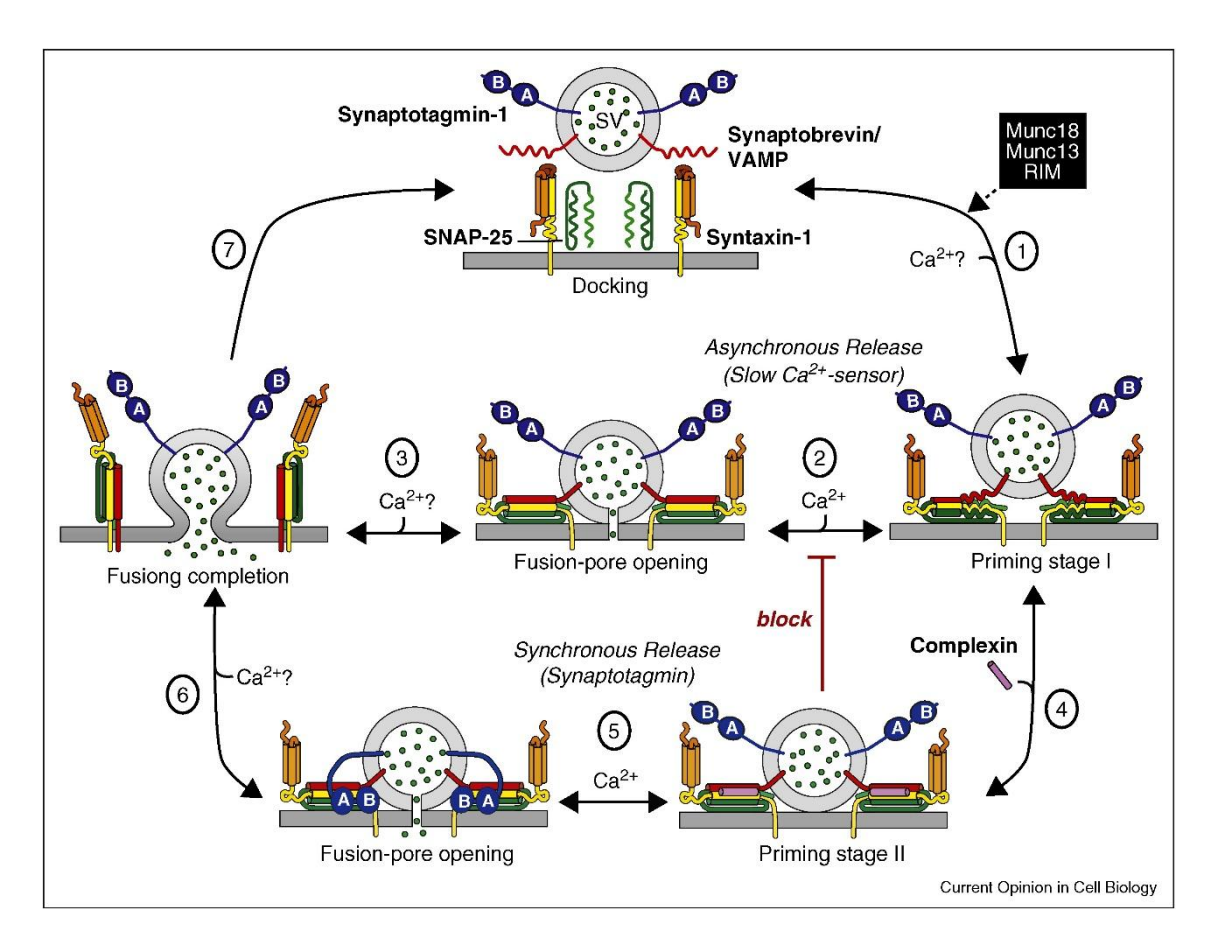


Figure 5: Model of the molecular steps mediated synaptic vesicle exocytosis.

Synaptic vesicles are docked at the active zone of a presynaptic terminal with unassembled SNARE complexes (top) and are then primed for release by partial SNARE-complex assembly that is catalyzed by Munc18, Munc13, and RIM (step 1). At least in inhibitory synapses, this priming process might be further modulated by ELKS2. The primed vesicles form the substrate for two main pathways of Ca²⁺-triggered neurotransmitter release: asynchronous release (steps 2 and 3), in which full assembly of SNARE complexes leads to fusion-pore opening followed by complete fusion (step 3); and synchronous release (steps 4, 5, and 6), in which 'superpriming' by binding of complexins to assembled SNARE complexes (step 4) activates and freezes SNARE complexes in a metastable state (referred to as priming stage II). This stage is then substrate for fast Ca²⁺-triggering of release when Ca²⁺-binding to synaptotagmin-1 induces its binding to phospholipids and to SNARE complexes, with the latter reaction displacing complexin and resulting in fusion-pore opening (step 5) and full fusion (step 6). Both the synchronous and the asynchronous release pathway can mediate spontaneous 'mini' release, depending on the local Ca²⁺microdomain. Synaptotagmin and complexin clamp (block, in red) the unidentified slow Ca2+-sensor that mediates the asynchronous release; this clamping is relieved when Ca²⁺ binds to synaptotagmin-1, allowing competition between synaptotagmin-1 and the asynchronous Ca2+-sensor during high-frequency stimulation. Adopted from (122).

1.6.1.1. Munc13s as a Regulatory Hub in SV Priming

Mammals possess three homologous Munc13 genes (123). Of these, Munc13-1 and Munc13-2 are expressed in hippocampal PCs (124). While Munc13-1 has a single variant,

Munc13-2 exists as two principal splice variants in CA1 PCs: the brain-specific bMunc13-2 and the ubiquitously expressed ubMunc13-2 (111, 123, 125–128). The C-terminal and central regions of Munc13-1, bMunc13-2, and ubMunc13-2 share conserved structures, including the C₂C, MUN, C₂B, and C₁ domains. These domains are functionally essential for SV priming activity and exhibit structural similarities to vesicle tethering factors (128–130). Notably, only Munc13-1 and ubMunc13-2 possess an additional N-terminal C₂A domain, which binds RIM (131, 132).

The multi-domain architecture of Munc13s allows their functions to be finely modulated by various proteins and second messengers, such as [Ca²⁺], diacylglycerol (DAG), Phosphatidylinositol phosphates (PIPs), and calmodulin. For instance, the C₂A domain of Munc13-1 forms homodimers that inhibit its docking and priming functions; this inhibition is relieved upon RIM binding (131, 133). Conversely, the MUN domain of Munc13-1 plays a pivotal role in vesicle priming by significantly accelerating the transition from the closed syntaxin-1–Munc18-1 complex to the SNARE complex. This is achieved by facilitating syntaxin-1 opening, a process reliant on weak interactions between the MUN domain and the syntaxin-1 SNARE motif (115). When the SV is tethered to the plasma membrane, the central Munc13-1 domains (C₁ and C₂B) anchor to the plasma membrane, while the C₂C domain interacts with the SV membrane (134). In its inactive state, the C₁-C₂B domains provide basal inhibition to Munc13, preventing SV fusion. This inhibition renders Munc13 activity susceptible to Ca²⁺, DAG, or PIPdependent control, thereby modulating synaptic strength (135, 136). The activity of the C₁ domain can be enhanced by DAG binding (produced by phospholipase C [PLC] upon increased intracellular [Ca²⁺]) or by phorbol esters like Phorbol 12,13-dibutyrate (PDBU), which consequently boost neurotransmitter release (137-140). Furthermore, Munc13-1 priming activity is also modulated by Ca²⁺ binding to the C₂B domain, which increases its affinity for PIP and PIP2. Significantly, mutations that increase Ca²⁺-dependent PIP2 binding have been shown to potentiate neurotransmitter release (141).

1.6.2. Docking & Priming of SVs is a Dynamic Process

As previously established, the priming process involves the tethering and docking of SVs to specialized release sites, as well as the assembly of macromolecular complexes that mediate Ca²⁺-dependent triggering of exocytosis (100). Docking, priming, and SNARE

complex assembly are dynamic and reversible processes (120, 142, 143), and that even at rest the docked and primed SV states may be labile and very dynamic (144). Biochemical studies have shown that the ternary SNARE complex can transition between "loose" and "tight" *trans* conformations (145, 146). A recent study combining fast freezing after a release-stimulating pulse with high-pressure electron microscopy ("zap and freeze"), examined the dynamics of docking (147). Shortly (5 ms) after an AP, the docked SV pool is depleted by fusion, with a concurrent increase in the number of SVs within the 10 nm range. Within 14 ms, new vesicles are recruited, fully replenishing the docked pool. However, this docking within 14 ms is transient; vesicles either undock or fuse within 100 ms. These findings demonstrate that SV recruitment to release sites is rapid and reversible, and show, for the first time, that Ca²⁺ elevation elicits docking within milliseconds. The same study suggests further changes in docking probability at later times following the AP, indicating a multi-step pathway with complex kinetics for incoming SVs (147). Another study shows that synaptotagmin-1 supports this transient, Ca²⁺-dependent, tight SV attachment to the PM following an AP within 10-50 ms (148).

These studies, along with recent electron microscopy data on the different tethering and docking/priming states of SVs and their molecular underpinnings (108, 149, 150), suggest a dynamic, Ca²⁺-dependent interchange between two primed SV states. Specifically, they propose that docked SVs fluctuate between a loosely docked and primed state (LS), where SNARE complexes are only partially zippered, and a tightly docked and primed state (TS), where zippering has progressed further, rendering the SVs fusion-competent (144, 151).

1.6.3. The Molecular Bases of Synaptic Vesicle Fusion

Calcium is essential for triggering synchronous SV fusion and neurotransmitter release. Although the *trans*-SNARE complex assembles independently of Ca²⁺, other factors confer the Ca²⁺ sensitivity necessary for SV fusion. The speed, temporal precision, and efficacy of Ca²⁺-dependent SV fusion are mediated by proteins like synaptotagmin-1 and complexins (*Figure 5*) (152–156). Synaptotagmin-1, a protein with two C2 domains, serves as the primary Ca²⁺ sensor for synchronous neurotransmitter release (119, 152). C2 domains are generally recognized as Ca²⁺-dependent or -independent membrane-targeting modules (157–159). Synaptotagmin1 knockout significantly reduces

synchronous SV release (160). Current research and existing data support a "release-of-inhibition" model for the initiation of Ca²⁺-triggered SV fusion. In a Ca²⁺-independent manner, synaptotagmin-1 interacts with the partially zippered SNARE complex, the plasma membrane, phospholipids, and other components to establish a primed, pre-fusion SV state. However, fusion is inhibited until Ca²⁺ arrives and binds to synaptotagmin-1's C2 domains, perturbing the lipid bilayer, facilitating membrane bridging, and ultimately activating fusion (159, 161–163).

The second group of fusion regulators are the complexins, a family of small (Molecular weight = 15–18 kDa) cytosolic proteins that bind tightly and in a 1:1 stoichiometry to assembled SNARE complexes (155, 164, 165). Mammals encode four complexin paralogs (Complexin 1-4) through four distinct genes. Complexins 1 and 2 are predominantly expressed in the CNS, while complexin 3 is weakly expressed in some brain regions, including the cerebral cortex and hippocampus.

In synapses expressing complexin 1/2, knockout of either paralog does not result in obvious functional deficits, suggesting functional redundancy (156, 166). However, double knockout of complexins 1/2, as well as triple knockout of complexins 1/2/3, alters synaptic function. For instance, the amplitude of AP-evoked EPSCs recorded from hippocampal autapses is reduced by over 65% compared to wild-type autapses (166). Complexins do not bind Ca²⁺, and their interaction with the *trans*-SNARE complex is Ca²⁺-independent. Working in concert with the Ca²⁺-sensing protein, synaptotagmin-1, complexins contribute to the Ca²⁺-dependent control of SV fusion. It has been proposed that complexins function post-priming by stabilizing the trans-SNARE complex to maintain SVs in a fusion-competent state (156, 167), or by acting as a fusion clamp, arresting the *trans*-SNARE complex and preventing premature fusion prior to synaptotagmin-1 activation by Ca²⁺ (168–171). The fusion-clamp model posits that complexins hinder fusion at rest, and synaptotagmin-1 is required to relieve the clamping activity upon Ca²⁺ arrival (169). One undisputed role of complexins is their facilitation of fast, AP-evoked synchronous neurotransmitter release (162).

1.6.4. The Role of Voltage-Gated Ca²⁺ Channels in SV Fusion

Calcium ions are essential for triggering neurotransmitter release. Voltage-gated Ca²⁺ channels in the plasma membrane are the primary source of Ca²⁺ at nerve terminals. Like

other voltage-gated ion channels, the opening probability of VGCCs changes in response to membrane potential fluctuations, allowing Ca^{2+} influx down a steep electrochemical gradient upon AP arrival. VGCCs are composed of a pore-forming $\alpha 1$ subunit and several auxiliary subunits (β , $\alpha 2$, and δ). These subunits exhibit multiple isoforms and splice variants, generating a diverse array of possible subunit combinations (172).

1.6.4.1. Types of Voltage-Gated Ca²⁺ Channels

Voltage-gated Ca^{2+} channels are classified into five groups (L, P/Q, N, R, and T-type) based on their pharmacological/biophysical properties, their tissue distribution and the sequence of their $\alpha 1$ subunits, which form the ion-conducting pore (172). The T-type channel is exclusive in being a low-voltage-activated (LVA) channel, with an activation threshold of approximately -70 mV. The other four types are high-voltage-activated (HVA) channels, with a threshold around -20 mV (173). The current nomenclature, based on the primary amino acid sequence of $\alpha 1$ subunit and the order of discovery, classifies VGCCs into $Ca_V 1.1-1.4$, $Ca_V 2.1-2.3$, and $Ca_V 3.1-3.3$ (174).

Numerous studies have investigated the VGCCs involved in SV release at presynaptic nerve terminals. These studies typically use specific Ca²⁺ channel blockers to assess the impact on postsynaptic responses. Results indicate that P/Q-type and N-type channels play a major role in neurotransmitter release at many synapses, including excitatory synapses in the hippocampus (175–178) and inhibitory synapses in the cerebellum and spinal cord (176). At some synapses, a single VGCC type mediates Ca²⁺ influx at presynaptic terminals. For example, at the rat calyx of Held synapse, Ca_v2.1 (P/Q-type) almost exclusively mediates release by postnatal day 10 (179). Other synapses, such as the glutamatergic synapses in the hippocampus utilize both Ca_v2.1 and Ca_v2.2 (P/Q- and N-type) to trigger neurotransmitter release (176, 178).

Given the predominant role of VGCCs in synaptic transmission, precise regulation of presynaptic VGCC activity is crucial for timely and accurate neurotransmitter release. This regulation is achieved through a variety of factors, including auxiliary subunits, membrane potential, G protein-coupled receptors, calmodulin, Ca^{2+} -binding proteins, protein kinases, various interacting proteins, alternative splicing, and genetic variations. For example, the unique long and coiled C-tail of the $\alpha 1$ subunit can interact with numerous proteins, as demonstrated by proteomic screening (180). For instance, RIM has

been shown to interact with the VGCC (181). The association of RIM with Cav2 increases channel activity and promotes synaptic transmission (182). Furthermore, RIM can bind to the β subunit and enhance its positive regulation of channel function (182). It is conceivable that SV fusion is influenced by the type of VGCCs present in the AZ, their regulation, their density within the AZ, and the distance between the VGCCs and the SV release sites (RSs).

Given the complexity of SV exocytosis underlying synaptic transmission, numerous models have been developed to simplify and describe this process. One such model, the sequential two-step priming model, which is used in this study, will be discussed in the following section.

1.6.5. The Sequential Two-Step Priming Model

A recently published two-step priming model posits two sequential docking/priming states. This model can be referred to as the Loose state/Tight state (LS/TS) docking model (*Figure 6*) (144, 151). The LS docking state describes an intermediate docked state where the vesicle is positioned at a small distance (5–10 nm) from the PM. Only upon transitioning to the TS, in close contact with the PM, does the vesicle become fusion-competent.

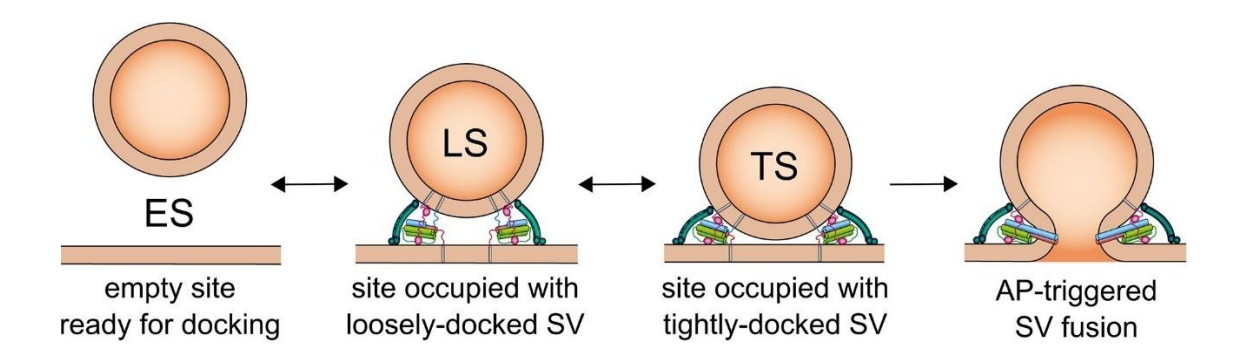


Figure 6: Basic sequential model for priming and fusion.

SVs dock to an empty release site (ES) and undergo two priming steps to sequentially transition to the LS and TS states. Only SVs in state TS are fusion competent. Adopted from (151).

The LS/TS docking model (similar to an alternative replacement site/docking site model (183) proposes that vesicles exist in a dynamic equilibrium between these two sequential

states at rest, prior to exocytosis. Forward priming rates are Ca^{2+} -sensitive, increasing with intracellular $[Ca^{2+}]$. Furthermore, only SVs within the TS pool can fuse upon AP arrival. This model has successfully reproduced STP and its diversity observed at calyx of Held synapses (151). Electron microscopy (EM) studies provide support for the existence of morphologically distinct docking states of SVs (108, 149, 184). According to this model, Pv is a function of SV fusion probability (P_{fusion}) and the probability (P_{TS}) that an SV is in the TS ($Pv = P_{fusion} * P_{TS}$).

2. OBJECTIVES

This study aims to address the question: What mechanisms regulate postsynaptic target cell type-dependent Pv and STP? Despite intensive research over the past two decades, the molecular mechanisms underlying differences in Pv and STP remain incompletely understood, and a unified picture has yet to emerge (91, 185, 186). In the current study, we focus on two distinct synapses: the hippocampal CA1 PC – FSIN connection, which exhibits high Pv and STD, and the PC – O-LM IN connection, which displays low Pv and STF, to investigate how PCs regulate Pv in a target cell-type-dependent manner. The following subsections will outline the potential mechanisms that will be explored as key objectives of this study.

2.1. Distinct Localization of Molecules in Post- and Presynaptic Compartments in a Target Cell Type-Dependent Manner

The first molecule identified with postsynaptic target cell type-dependent localization in the presynaptic AZ of PCs was mGluR7. It was found to be selectively enriched in hippocampal PC AZs that innervate SST/mGluR1α-expressing INs (187), and its constitutive activity contributes to the low postsynaptic response amplitude at this synapse (188). Interestingly, mGluR7 is recruited to the AZ by Elfn1, which is selectively expressed by SST/mGluR1α+ INs and located in the excitatory postsynaptic densities where Elfn1 trans-synaptically binds and activates mGluR7 (56, 189, 190). Ectopic expression of Elfn1 in PV+ INs in the hippocampus altered the STP from depression to moderate facilitation through an unknown mechanism (56).

Although presynaptic neurotransmitter receptors can strongly influence neurotransmitter release and STP, synapses still exhibit diverse functional properties even in the presence of numerous presynaptic receptor blockers. This diversity likely stems from the heterogeneous molecular components of the AZ matrix that mediate SV docking, priming, and release (191). Among these components are members of the Munc13 protein family, and Munc13-containing supramolecular complexes. Munc13-1 and Munc13-2, are expressed in hippocampal PCs (124). Experiments in cultured autaptic neurons suggest that Munc13-1 and Munc13-2 confer different STP to synapses. In 90% of axon terminals of cultured PCs, Munc13-1-primed vesicles have high *Pv*, and the synapses

display STD, while in 10% of boutons, the presence of Munc13-2, in the absence of Munc13-1, confers low Pv and STF (124). As this correlation appears to hold in other synapses (192, 193), the following concept has emerged: high-Pv synapses that show STD are equipped with Munc13-1, which enables tight docking of readily releasable SVs, whereas low-Pv synapses that display STF employ Munc13-2, and vesicles are loosely docked, requiring an increase in intracellular $[Ca^{2+}]$ to become release-competent (144). Munc13-2 immunolabeling in the hippocampus has shown an uneven distribution of the protein, with strong staining in the str. oriens of the CA1 area (125), where most of the dendrites of mGluR1 α + INs are located. This raises the question of whether the low Pv of CA1 PC to mGluR1 α + IN synapses could result from the presence of Munc13-2 as a priming factor. Therefore, the localization and the role of Munc13-2 in the low-Pv synapse of the PC – O-LM IN connection has been investigated in this study.

A second potential factor influencing differential Pv, which will be examined, is the variation in effective Ca^{2+} concentration that triggers the final step of exocytosis: SV fusion.

2.2. Different Effective [Ca²⁺] Reaching Docked SVs.

Given the steep dependence of SV release on [Ca²⁺] (194), the most apparent difference between PC – FSIN and PC – O-LM IN connections was hypothesized to be a significant difference in the "effective" [Ca²⁺] that SVs "see" at their RSs. This difference could arise from either a greater number (conductance) of VGCCs or a shorter distance between these channels and the Ca²⁺ sensor responsible for SV fusion. Both potential possibilities will be addressed.

2.2.1. Differential Presynaptic Action Potential-Evoked [Ca²⁺] Influx

Nearly two decades ago, Koester & Johnston (2005) reported smaller presynaptic [Ca²⁺] transients in cortical PC axon terminals innervating bitufted (SST-expressing) INs compared to multipolar FSINs. A more recent study in CA3 hippocampus corroborated these findings in the hippocampus (186), but the difference in presynaptic [Ca²⁺] was only 30% between the high-Pv parvalbumin-targeting boutons and the low-Pv mGluR1 α -targeting boutons. Therefore, it is essential to investigate this potential factor in our study. Even if this relatively small difference will be consistent with CA3, variations in the

coupling distance between Ca^{2+} channels and SVs (91, 195, 196) could still explain the significant Pv disparity observed between PC – FSIN and PC – O-LM IN connections.

2.2.2. Differential Coupling Distances Between Presynaptic VGCCs and the Ca²⁺ Sensors of SV Fusion

Examining the effects of fast and slow Ca²⁺ buffers on release (91), concluded that a longer coupling distance between presynaptic VGCCs and the Ca²⁺ sensor on SVs might contribute to the low Pv observed at PC – SST IN synapses in juvenile neocortex. The simplest explanation for this result is a lower presynaptic VGCC density at the low-Pv synapses. A previous study from our laboratory tested this hypothesis and found only a 15% difference in VGCC density (186). However, it became clear that coupling distance cannot be predicted from VGCC density alone, as docked SVs and VGCCs are not randomly distributed within AZs. Indeed, distinct, non-random nanoscale topologies of SVs and VGCCs have been proposed at different synapses. A recent study (196) provided compelling evidence that synaptic strength cannot be predicted from the magnitude of presynaptic Ca²⁺ influx and VGCC density. Cerebellar parallel fiber synapses exhibit low Pv and paired-pulse facilitation, whereas molecular layer INs synapses have higher Pv and display STD. Interestingly, AP-evoked Ca²⁺ influx and VGCC density are significantly higher at the weak parallel fiber synapses. However, examination of the nanoscale arrangements of RSs and VGCCs revealed a larger coupling distance at the weak synapse. At parallel fiber AZs, VGCCs are excluded from an approximately 50 nm area surrounding RSs, whereas, in the strong IN synapses, a much smaller number of VGCCs are clustered immediately adjacent to the RSs (15-20 nm) (196). Because these results clearly demonstrate the need to understand the nano-topologies of RSs and VGCCs to predict synaptic strength, we investigated this aspect for PC – FSIN and PC – O-LM IN synapses using high-resolution EM SDS-digested freeze-fracture replica immunolabeling (SDS-FRL) in the hippocampal CA1 area of adult mice.

2.3. Differential Occupancy of RSs by SVs

An alternative explanation for the low Pv observed at PC – O-LM IN synapses is the low occupancy of RSs by SVs. Pv can be conceptualized as a function of the probability that an RS (or docking site) is occupied by an SV (P_{occ}) and the probability with which a docked vesicle is released (P_{fusion}) upon AP arrival ($Pv = P_{occ} * P_{fusion}$) (151, 197–199).

While dissecting the individual contributions of these two factors is challenging, Malagon et al., 2020 analyzed release at cerebellar parallel fiber-MLIN simple synapses and found that P_{occ} under physiological [Ca²⁺]_e (1.5 mM) is only 0.2, primarily accounting for the low Pv at these synapses. Therefore, another possible mechanism underlying the low Pv at PC – O-LM IN synapses is a low P_{occ} , which we also investigate here using a combined *in vitro* physiological and pharmacological approach, together with EM tomography.

2.4. Differential Priming State of Docked SVs

It has been shown (200–202) that heterogeneity of docked SVs with respect to their priming states at rest can explain distinct Pv. Similarly, the dynamics between different states during repetitive synaptic activity can cause pronounced differences in STP (144, 200–208). This concept is captured by a recently published sequential, two-step priming model (explained previously in section 1.6.5.) that assumes two sequential states of docking/priming prior to exocytosis, namely TS and LS (151).

According to this model, Pv is a function of P_{fusion} and the probability (P_{TS}) that an SV is in the TS ($Pv = P_{fusion} * P_{TS}$). If we assume that SVs at O-LM IN-innervating synapses are primarily in the LS state at rest, while a large fraction of SVs are already in the TS in FSIN-innervating synapses, then differences in P_{TS} , rather than P_{fusion} , might be the primary reason for the observed Pv differences at these two synapse types. This hypothesis was tested by applying a set of simple and complex presynaptic stimulation protocols to PC – FSIN and O-LM IN connections. Subsequently, mathematical modeling of the resulting EPSCs was performed using the sequential two-step priming model (151) to investigate the key differences between these two connection types.

3. METHODS

3.1. Animals

For electrophysiological recording, two hundred and three adult (P48-90) male and female transgenic mice used (Chrna2-Cre) OE25Gsat/Mmucd, were (RRID:MMRRC 036502-UCD, on C57BL/6J background (53) crossed with reporter line (Gt(ROSA)26Sor CAG/LSL tdTomato). Ai9 Ai14 For Elfn1-KO or electrophysiological recording, 15 adult (P50-70)male C57BL/6N-*Elfn1*^{tm1.1}(KOMP)Vlcg/MbpMmucd (RRID:MMRRC 047527-UCD, C57BL/6N on background (189) and 5 heterozygous littermate control mice were used. For Munc13-2 35 (P50-70)conditional KO recording, adult C57BL/6N-Unc13b^{TM1a(KOMP)Wtsi}/MbpMmucd (RRID:MMRRC_050292-UCD, on C57BL/6N background) were used. Seven C57BL/6J male mice (P49-63) were used for SDS-FRL experiments. Six C57BL/6J male mice (P32-39) and two young adult male Wistar rats (P30, 42) were used for immunofluorescent experiments. The animals were housed in the vivarium of the Institute of Experimental Medicine in a normal 12 h/12h light/dark cycle and had access to water and food ad libitum. All the experiments were carried out in accordance with the Hungarian Act of Animal Care and Experimentation 40/2013 (II.14) and with the ethical guidelines of the Institute of Experimental Medicine Protection of Research Subjects Committee.

3.2. Virus Injection

Mice were anesthetized with a mixture of ketamine, xylazine, pipolphene (0.625, 6.25, 1.25 mg/mL respectively, 10 μL/g body weight). We injected either pAAV-Ef1a-mCherry-IRES-Cre (a gift from Karl Deisseroth; 1.8 × 10¹³ vg/mL, Addgene viral prep # 55632-AAV8; RRID:Addgene_55632; Fenno et al., 2014) or pENN.AAV.CamKII 0.4.Cre.SV40 (a gift from James M. Wilson; Addgene viral prep # 105558-AAv92; RRID:Addgene_105558) at 1:10 dilution (2.8 × 10¹³ vg/mL, Penn Vector Core) into the dorsal hippocampus. Injections consisted of 200 nL at coordinates from the Bregma in mm: antero posterior/dorso ventral/lateral: 2.1/1.1/1.3 and/or 2.2/1.5/1.2). After two weeks, the mice were either perfused or in vitro acute slices were prepared from the dorsal hippocampus as below.

3.3. Slice Preparation

Mice were stably anesthetized with a ketamine, xylazine, pypolphene cocktail (0.625, 6.25, 1.25 mg/mL respectively, $10 \mu L/g$ body weight) then decapitated, the brain was quickly removed and placed into an ice-cold cutting solution containing the following (in mM): sucrose, 205.2; KCl, 2.5; NaHCO₃, 26; CaCl₂, 0.5; MgCl₂, 5; NaH₂PO₄, 1.25; and glucose, 10, saturated with 95% O₂ and 5% CO₂. Then, 250 or 300 μ m thick coronal slices were cut from the dorsal part of the hippocampus using a Vibratome (Leica VT1200S) and were incubated in a submerged-type holding chamber in artificial cerebrospinal fluid (ACSF) containing the following (in mM): NaCl, 126; KCl, 2.5; NaHCO₃, 26; CaCl₂, 2; MgCl₂, 2; NaH₂PO₄, 1.25; and glucose, 10, saturated with 95% O₂ and 5% CO₂, pH = 7.2 to 7.4, at 36 °C for 30 min, and were then kept at 22 to 24 °C.

3.4. Electrophysiological Recordings

All whole-cell patch-clamp paired recordings were conducted at 32-33 °C, up to 6 h after slicing. The ACSF was supplemented with 2 μ M AM251 to block presynaptic CB1 receptors and 0.35 mM γ DGG to prevent AMPA receptor saturation. Cells were visualized using infrared differential interference contrast (DIC) imaging on a Nikon Eclipse FN1 microscope equipped with a 40X water immersion objective (NA = 0.8). CA1 PCs were identified based on their position and morphology. O-LM INs in the str. oriens of the CA1 region were identified by tdTomato fluorescence in Chrna2-Cre-tdTomato animals, or by their somatic morphology and characteristic membrane voltage responses to de- or hyperpolarizing current injections (600 ms, from -250 to 800 pA with 100 pA steps). Following recordings, these cells were further characterized *post hoc* by their dendritic and axonal arborization and mGluR1 α immunoreactivity. FSINs were identified by their position, somatic morphology, and membrane voltage responses to de- or hyperpolarizing current injections (600 ms, from -250 to 800 pA with 100 pA steps).

Patch pipettes (4 to 6 M Ω resistance) were pulled from thick-walled borosilicate glass capillaries with an inner filament. The intracellular solution for INs contained (in mM): K-gluconate, 130; KCl, 5; MgCl₂, 2; EGTA, 0.05; creatine phosphate, 10; HEPES, 10; ATP, 2; GTP, 1; and biocytin, 7, pH = 7.3; 290 to 300 mOsm. For presynaptic PCs, the intracellular solution was either similar to the IN solution but supplemented with 10 mM glutamate or contained (in mM): K-gluconate, 97.4; KCl, 43.5; MgCl₂, 1.7; NaCl, 1.8;

EGTA, 0.05; creatine phosphate, 10; HEPES, 10; ATP, 2; GTP, 0.4; biocytin, 7 and 10 mM glutamate, pH = 7.25; 290 to 305 mOsm.

Paired whole-cell recordings were performed with PCs held in current-clamp mode at -65 mV (with a maximum of ± 100 pA DC current). Postsynaptic INs were held at -65 mV in voltage-clamp mode (with a maximum of ± 200 pA DC current) with access resistance maintained below 20 MΩ using a dual-channel amplifier (MultiClamp 700B; Axon Instruments). Action potentials were evoked in PCs with 1.5 ms long depolarizing current pulses (2.3 nA). Three to five APs at 40 Hz were evoked with 9 seconds inter-trace intervals and evoked EPSCs were recorded for PC – FSINs and PC – O-LM INs pairs. For modeling, PC – FSIN connections were recorded using six different stimulation protocols: 1) 15 APs at 5 Hz; 2) 15 APs at 100 Hz followed by a 6-AP recovery test train after 110 ms at 100 Hz; 3) 6 APs at 100 Hz followed by a 6-AP recovery test train at 100 Hz after 110 ms; 4) 6 APs at 100 Hz followed by a 6-AP recovery test train at 100 Hz after a 1.5 s recovery test period; 5) a 6-AP preconditioning train at 20 Hz followed by a 15-AP train at 100 Hz then a 6-AP recovery test train at 100 Hz after 110 ms; and 6) a 6-AP preconditioning train at 20 Hz followed by a 15-AP train at 100 Hz then a 6-AP recovery test train at 100 Hz after a 1.5 s recovery test period. For PC – O-LM IN pairs, only protocols 5 and 6 were recorded. Ten minutes were recorded for each protocol and 60 second inter-trace intervals were maintained, except for protocols 3 and 4 where a 30 second inter-trace interval was utilized. INs with an increase in access resistance exceeding 25% during the recording period were excluded from analysis.

Data were filtered at 3-4 kHz (Bessel filter), digitized online at 50 kHz, and then recorded and analyzed using Clampfit 10.7 (Molecular Devices). Peak amplitudes, 10-90% rise times, and areas under the curves were calculated in Clampfit.

3.5. Pharmacological Manipulation

To determine the effects of pharmacological agents on postsynaptic EPSC amplitudes, eEPSCs were recorded from PC – FSIN and PC – O-LM IN pairs. Each experiment involved a 10-minute baseline recording, a 10-minute drug wash-in period, followed by subsequent 10-minute recordings to assess the drug effect.

The stability of postsynaptic responses was evaluated during 30-minute whole-cell recordings in control ACSF. For FSIN postsynaptic cells, eEPSC amplitude remained stable, with the relative amplitude in the final 10 minutes of recordings being 0.99 ± 0.39 compared to the initial 10 minutes. In contrast, when the postsynaptic IN was an O-LM cell, the same protocol unexpectedly resulted in a 48% eEPSC rundown (normalized amplitude: 0.52 ± 0.51 , n = 28 pairs; Supplementary Figure S2C in Aldahabi et al., 2022). To counteract this rundown, a limited number of paired recordings were performed using the perforated patch configuration for the presynaptic PC (see below). In these specific experiments, the relative EPSC amplitude at the end of the recordings was 0.94 ± 0.25 (n = 6), which did not significantly differ from the initial 10 minutes (Supplementary Figure S2C & S2D in Aldahabi et al., 2022). However, given the exceptionally low yield of finding connected PC – O-LM IN pairs and maintaining their stability without membrane rupture, most of pharmacological experiments were conducted in dual whole-cell mode. Drug effects were subsequently corrected *post hoc* based on the average rundown observed during comparable time periods in ACSF control recordings.

3.6. Perforated Patch-Clamp Recordings

Perforated patch-clamp recordings were carried out from the presynaptic PCs to avoid rundown. The intracellular solution was supplemented with 100 μ g/mL Gramicidin (freshly dissolved in DMSO on the recording day and used only for 2 h when dissolved in the intracellular solution) and 12 μ M Alexa Fluor 594. Pipette resistance was 18–25 M Ω and the pipette tip was back-filled with Gramicidin-free intracellular solution then with Gramicidin-containing intracellular solution. The spontaneous membrane rupture was regularly checked and if fluorescence was detected in the soma of the PC, the recording was discarded (e.g. Supplementary Figure S2C in Aldahabi et al., 2022). An average of 10-20 min was needed to achieve an access resistance of <150 M Ω and to start the paired recording protocols.

3.7. Two-Photon Laser Scanning Microscopy

These experiments have been performed by Dr Noemi Holderith in our laboratory. For detailed methods of Ca^{2+} -imaging see (186, 210). Briefly, Rrecordings were performed in ACSF supplemented with 2 μ M AM251 to block presynaptic CB1 receptors at 29–30°C up to 6 h after slicing. Cells were filled for 90 min with intracellular solution with

a Ca²⁺-insensitive (25 μ M Alexa Fluor 594) and a Ca²⁺-sensitive fluorophore (200 μ M Fluo5F). Boutons were selected at 50-300 μ m distances from the soma, imaged in line scan mode at 1 kHz, with a laser intensity of 2-6 mW at the back aperture of the objective lens. Each bouton (on average 16 ± 8 per cell) was scanned once for baseline measurement, and once after washing in the control or drug solution for 10 min. Fluorescence changes upon 5 APs at 40 Hz were recorded. Only the peak amplitude of the $[Ca^{2+}]$ transient obtained for the first AP was quantified during the recording as $G/R_{(t)}=(F_{\text{green}(t)}-F_{\text{rest, green}})/(F_{\text{red}}-I_{\text{dark, red}})$ where $F_{\text{green}(t)}$ represents the green fluorescence signal as a function of time, $F_{\text{rest, green}}$ is the green fluorescence before stimulation, and $I_{\text{dark, red}}$ is the dark current in the red channel. To normalize data across batches of dyes, G_{max}/R values were measured by imaging a sealed (tip melted and closed by heating) pipette filled with intracellular solution containing 10 mM CaCl₂ for each cell at the same position where the boutons were imaged. G/R measurements from boutons were divided by G_{max}/R , yielding the reported values of G/G_{max} .

3.8. Tissue Processing After Paired Whole-Cell Patch-Clamp Recordings

After recordings, the slices were fixed in a solution containing 4% formaldehyde, 0.2% picric acid in 0.1 M phosphate buffer, pH = 7.4, at 4 °C for 12 h. Slices were embedded in agarose (2%) and re-sectioned at 120–150 μm thickness. Biocytin was visualized with Cy3-conjugated streptavidin (1:1000) diluted in TBS containing 0.2% Triton X-100. Sections were mounted in Vectashield. Image stacks were acquired with an Olympus FV1000 confocal microscope with a 20X or a 60X (oil-immersion) objectives. Recorded INs were classified based on the dendritic and axonal arbors.

3.9. Multiplexed Postembedding Immunolabeling

These experiments have been performed by Dr Noemi Holderith in our laboratory. For detailed methods see (211, 212)

3.10. EM Tomography

These experiments have been performed by Dr Noemi Holderith. For detailed methods see (210).

3.11. SDS-Digested Freeze-Fracture Replica Labelling

These experiments have been performed by Dr Andrea Lorincz. For detailed method see (210).

3.12. Modelling Short-Term Plasticity.

The sequential two-step priming model (151) was implemented in Berkeley Madonna [version 10.4]. Michaelis–Menten-like saturation for kl 0 in response to [Ca²⁺] was implemented, but the Ca^{2+} dependence of P_{fusion} , as described in (151), was omitted. In addition to the LS and TS states, a "Labile Tight State" (TSL) was incorporated, as it contributes to release at high frequencies, consistent with Lin et al. 2022. Euler's integration method was used as the numerical procedure for solving the differential equations. The model parameters were optimized to fit the experimental data using the software's built-in algorithm. Unless otherwise stated, the resting [Ca²⁺] was constrained to 50 nM, and the increment of effective [Ca²⁺] following each AP was constrained to 110 nM according to Lin et al. 2022, and these parameters were kept constant during fitting. Parameter values are presented in SI Appendix, Table S1, Aldahabi et al., 2024. To quantify the "goodness of fit," the root-mean-square deviation (RMSD) was calculated for each fit. EPSC amplitudes were converted to quantal content, the number of released SVs, by dividing the peak amplitudes by the estimated quantal size. For the PC – FSIN synapse (mean peak amplitude 160 pA), the estimated quantal size is 32 pA (213), resulting in an initial release of 5 quanta. The quantal content of the PC - O-LM IN connection was estimated to be one tenth of the PC – FSIN connection, therefore, traces were scaled for an initial release of 0.5 quanta.

3.13. Parameter Optimization for the PC – O-LM IN Connections

First, we searched for a single parameter that would change the model from STD to STF. Results showed that only three parameters were capable of converting the model from STD to STF: b2, the backward rate constant of the second priming step, $k2_0$, the resting value of its forward rate constant, and P_{fusion} (see SI Appendix, Table S1, Aldahabi et al., 2024). While the model regimes exhibit STF, none of them describe adequately the data. Hence, we continued our search for model parameters that converted STD to STF, but this time changing two parameters simultaneously. Results showed that, while the two-parameter optimization was better than the one-parameter optimization, there were still

great mismatches between the model and data. For example, the solution involving $k2_0$ and the steepness of its Ca^{2+} dependence, s2, had a reasonably good fit of the first release and the preconditioning EPSC amplitude train, but vastly underestimated the EPSC recovery; the $P_{fusion}+b2$ solution produced an acceptable EPSC recovery but started with an initial SV release of zero. Allowing the simultaneous optimization of three parameters revealed parameter constellation that qualitatively described the dynamics of SV release at the PC – O-LM IN synapse. As shown in $Figure\ 22A$, when $k2_0$, s2, and P_{fusion} were simultaneously optimized, the model qualitatively described the initial small facilitation and depression, followed by the large facilitation and depression during the high-frequency EPSC train. Furthermore, the recovery was also reasonably well described, reflected in a robust reduction of the RMSD value. Finally, we allowed all parameters to be optimized (with the exception of resting $[Ca^{2+}]$ and AP-induced $[Ca^{2+}]$ increments), which resulted in a further improvement of the goodness of fit (RMSD = 0.00027; $Figure\ 22B$). Notably, the largest improvement involved the first EPSC response of the recovery train. All data are given as mean \pm SD.

4. RESULTS

4.1. Differential Synaptic Strength and STP Patterns from CA1 PC – FSIN vs PC – O-LM IN

Whole-cell patch-clamp pair recordings were performed between PCs and either FSINs or O-LM INs in CA1 hippocampus. Transgenic mice expressing tdTomato in O-LM INs (Chrna2-Cre-tdTomato) were used to readily identify O-LM INs. Morphological identification of 45 patched tdTomato INs located in the str. oriens was performed. Forty-three INs were identified as O-LM IN, while two were bistratified INs, demonstrating that this Chrna2 animal line exhibits over 95% specificity in labeling O-LM INs. FSINs, conversely, were identified based on their location in the str. pyramidale or str. oriens, their somata size, and their firing pattern.

For the 1st AP, PCs frequently failed to evoke EPSCs in O-LM INs, with a high failure rate of 82 \pm 12% resulting in a small mean eEPSCs peak amplitude of 9.4 \pm 9.6 pA, (*Figure 7A & D*, n = 96 pairs). A continuous increase in eEPSCs amplitude was observed in response to the second and third APs at 40 Hz, showing STF with paired-pulse ratio (2nd eEPSC/1st eEPSC; PPR) of 2.26 \pm 1.07 (n = 79; *Figure 7A & D-G*). In contrast, the PC – FSIN connection exhibited a first eEPSCs amplitude of 142.9 \pm 145.9 pA (n = 70; *Figure 7B, D & F*) and showed STD with a PPR of 0.92 \pm 0.31 (n = 70, *Figure 7B & D-G*), resulting in a ~15-fold difference in the 1st eEPSCs amplitude between PC – FSIN and PC – O-LM IN (*Figure 7C, D & F*). A previous study from our laboratory (213) demonstrated that the *Pv* of PC – FSIN synapses in 2 mM [Ca²⁺]_e is 0.42, while it is 0.04 \pm 0.04 in PC – O-LM cell synapses (M. Aldahabi, N. Holderith and Z. Nusser, unpublished data), indicating that the primary reason for the ~15-fold difference in the eEPSC amplitude is a robust, ~10-fold difference in the initial *Pv* of the synapses.

This postsynaptic target cell type-dependent specificity in synaptic Pv must be regulated by differential types or regulatory mechanisms of molecules. We investigated whether the low Pv observed at CA1 PC to mGluR1 α + O-LM IN synapses could be attributed to the presence of Munc13-2 as a priming factor. Therefore, we examined the localization of Munc13-2 at the low-Pv PC – O-LM IN synapses.

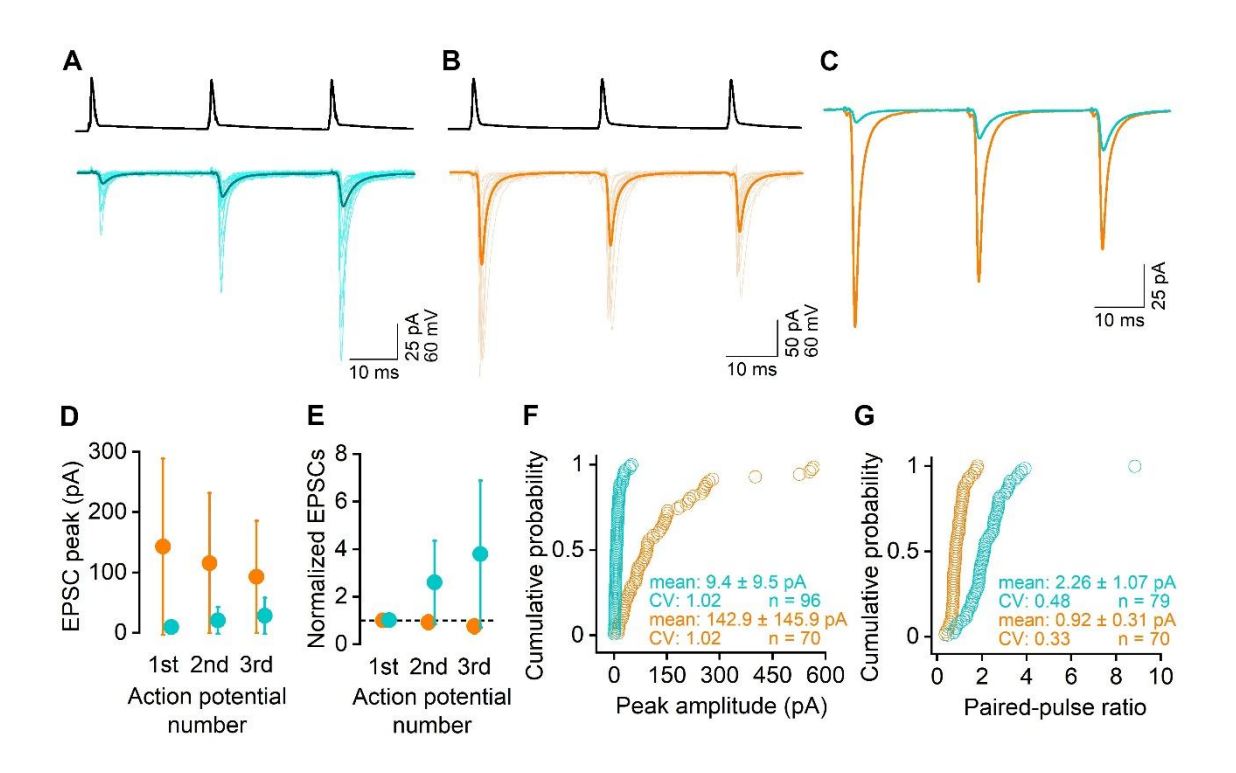


Figure 7: Distinct EPSC amplitudes and short-term plasticity of CA1 PC – FSINs vs. PC – O-LM cell synapses

(A and B) Averaged postsynaptic responses evoked by three action potentials (at 40 Hz) in presynaptic PCs are shown in O-LM cells (A, thin traces: 17 individual pairs; thick trace: the average of 96 pairs) and FSINs (B, thin traces: 16 individual pairs, thick trace: the average of 70 pairs). The amplitude of the first eEPSCs and the short-term plasticity of the responses show large variability within groups but are considerably different between O-LM cells and FSINs.

- **(C)** Superimposed PC O-LM IN (cyan, average of 96 pairs) and PC FSIN (orange, average of 70 pairs) eEPSCs demonstrate the dramatic difference in the amplitude (the first EPSC is ~15 times larger in FSINs) and short-term plasticity.
- **(D)** The amplitudes (mean \pm SD) of the eEPSCs in O-LM IN (n = 96 pairs) and FSINs (n = 70 pairs) are shown for the three consecutive APs.
- (E) Same as in (D), but normalized amplitude values are shown for demonstration of the difference in the short-term plasticity of the responses.
- (F and G) Cumulative probability plots of the peak amplitude of the first eEPSC (F) and the paired-pulse ratio (G) in O-LM cells (cyan) and FSINs (orange). Mean \pm SD, coefficient of variations (CV), and number of pairs are shown in the figure. For 17 PC O-LM IN pairs, first eEPSC was 0 pA, precluding the calculation of PPR (G). This figure was adopted from Aldahabi et al. (2022)

4.2. Munc13-2 Selectively Localizes to Synapses Targeting mGluR1α+Dendrites

Immunostaining of Munc13-2 in the dorsal hippocampus of mice (n = 3) and rats (n = 2) revealed punctate labeling of neuronal processes in the str. oriens and the alveus of the

CA1 hippocampus. Double immunolabeling of Munc13-2 and mGluR1 α showed that most of the Munc13-2 puncta decorate mGluR1 α dendrites, and the majority of mGluR1 α + dendrites are decorated by Munc13-2 puncta (*Figure 8A & B*). Given that mGluR7 is present in glutamatergic synapses targeting mGluR1 α -positive dendrites (187), similar to Munc13-2, we performed colocalization of these two molecules. Most of Munc13-2 puncta were positive for mGluR7 and vice versa (See Supplementary Figure 1C & 1D in Holderith et al. 2022). This suggests that Munc13-2 is present in glutamatergic synapses.

Postembedding multiplexed immunolabeling of several synaptic proteins was performed to further investigate the composition of these Munc13-2 immunopositive synapses. Qualitative assessment of the confocal images revealed that these Munc13-2 puncta were immunopositive for several synaptic markers such as PSD95, AMPA receptors, Bassoon, Cav2.1 VGCC subunit and Rim 1/2 (Figure 8D). The fluorescent intensities for each of these proteins were quantified in circular ROIs around the Munc13-2 positive puncta. We found that all Munc13-2 puncta contained PSD95 immunosignal, indicating that these are glutamatergic synapses (Figure 8E). Munc13-2 density values displayed large variability among individual synapses and did not correlate with the Munc13-1 density values (Figure 8F), suggesting that their amounts in the synaptic AZ are individually regulated. Interestingly, the PSD95 normalized densities of Munc13-1, AMPA receptors, Bassoon, Ca_V2.1, and Rim1/2 were significantly higher in synapses on mGluR1α+ dendrites compared to randomly selected surrounding synapses. Specifically, the normalized densities were: Munc13-1: 1.27 ± 0.58 ; AMPAR: 1.46 ± 0.50 ; Bassoon: 1.47 ± 0.85 ; Cav2.1: 1.38 ± 0.57 ; and Rim1/2: 1.22 ± 0.6 (Figure 8G; n = 194 mGluR1 α targeting and n = 160 random synapses from 2 mice). To assess the selectivity of Munc-13-2 expression in synapses targeting mGluR1α-+ dendrites, the immunosignal of Munc13-2 was compared between these synapses and random synapses in the surrounding neuropil in two mice (n = 101 and n = 60 mGluR1 α + dendrite-targeting synapses, and n = 1,000 and n = 500 random synapses). This revealed that only 4% of the Munc13-2 immunoreactivity is present in the surrounding randomly sampled synapse (Figure 8H).

Munc13-2 did not colocalize with vesicular inhibitory amino acid transporter (VIAAT; Figure 8I & J; n = 152 Munc13-2, and n = 222 VIAAT positive puncta in 2 mice) or with vesicular glutamate transporter-2 (vGluT2; Figure 8K & L; n = 43 Munc13-2 and n = 33

vGluT2 positive puncta in 1 mouse). This indicates that most of the Munc13-2 labeled puncta are present on the axon terminals of local (CA1 and/or CA3) PCs.

(The immunolabeling results were contributed by Noemi Holderith).

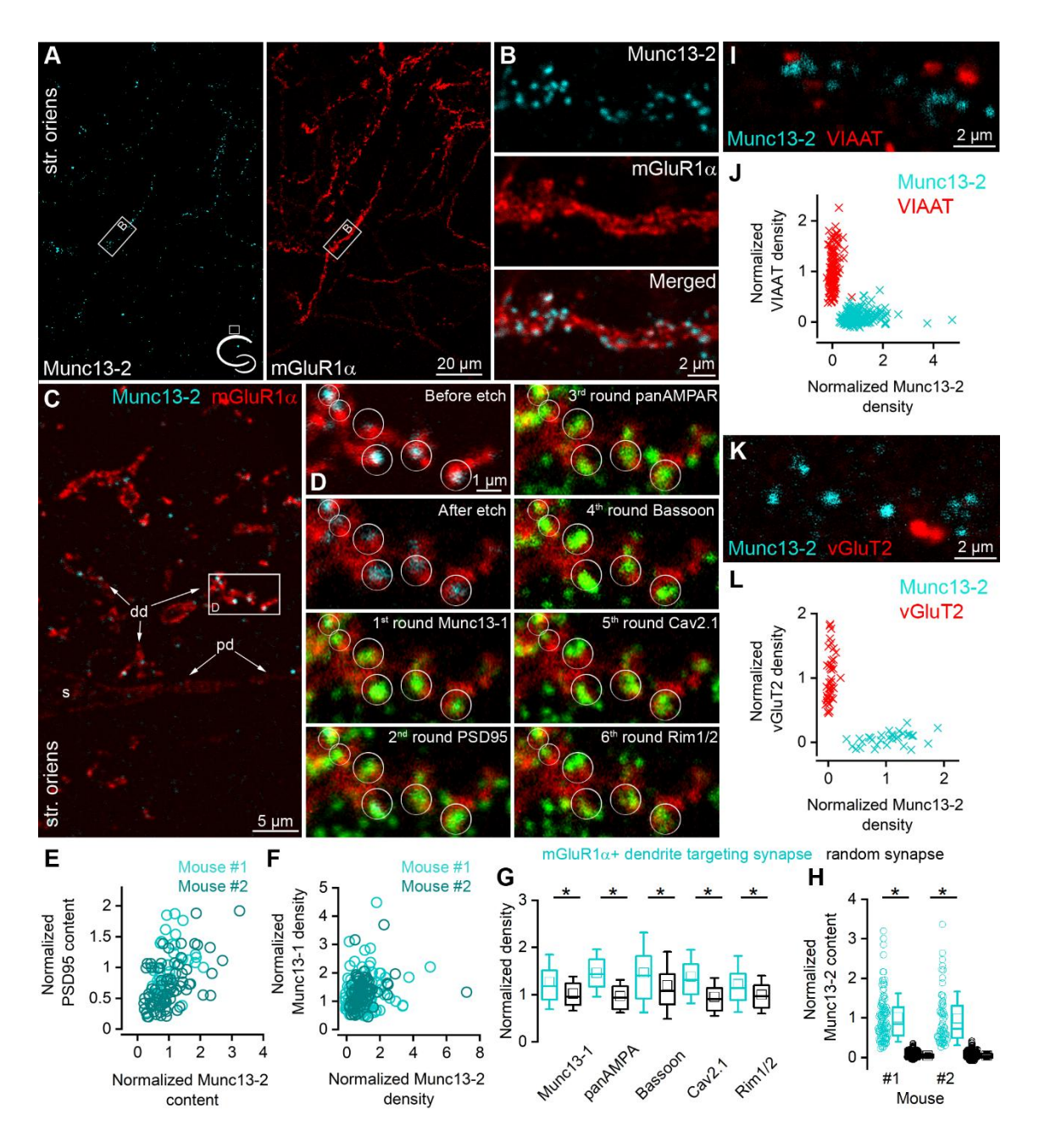


Figure 8: Munc13-2 immunolabeling is enriched on mGluR1 α immunopositive dendrites.

(A) Double immunolabeling for Munc13-2 (left, cyan) and mGluR1 α (right, red) in the dorsal hippocampal CA1 region of the mouse (cartoon indicates the location of the region) shows similar distribution in the stratum oriens. Maximum intensity projection of six confocal images separated by 1 μ m.

(B) A dendritic segment of an mGluR1α immunopositive IN (white boxes on A) is shown at a higher magnification, which is decorated by Munc13-2 immunopositive puncta. Maximum intensity projection

of three confocal images separated by 1 μm.

- (C) 500 nm thick epoxy resin embedded section with preembedding immunolabeling for Munc13-2 (cyan) and mGluR1 α (red) shows that Munc13-2 immunopositive puncta preferentially located on the small diameter of mGluR1 α + (distal) dendrites (dd), and mainly avoid the soma (s) and a proximal dendrite (pd) in the hippocampus of the mouse. Boxed area is enlarged on panel (D).
- (D) Multiplexed postembedding immunolabeling carried out on the section shown in panel (G). Munc13-2 immunopositive puncta marked by circles (representing ROIs for quantification) along the mGluR1 α immunolabeled dendrite are immunopositive for Munc13-1, PSD95, AMPA receptors, Bassoon, Cav2.1, and Rim1/2 (all pseudo colored to green). Note that the intensity of Munc13-2 immunolabeling varies substantially. Alignment of sections after each round was based on mGluR1 α immunolabeling (red). Numbers represent the labeling rounds during the multiplexed labeling.
- (E) All of the Munc13-2 immunopositive puncta contain PSD95 immunosignal. Their amount shows positive correlations (Spearman correlation r = 0.48 [n = 40] and 0.55 [n = 80] in mouse #1 and mouse #2, respectively).
- (F) Correlations between the density of the Munc13-2 and Munc13-1 in individual AZs (each data point represents an AZ, n = 114 in mouse #1 and n = 80 in mouse #2; Spearman correlation r = 0.16 and 0.34).
- (G) mGluR1 α IN targeting synapses have significantly larger (*) Munc13-1, AMPA receptors, Bassoon, Cav2.1 and Rim1/2 densities than those found in randomly selected glutamatergic synapses in the str. oriens (p = 1.5×10^{-5} , 5.5×10^{-24} , 1.5×10^{-4} , 6.6×10^{-16} , 1.3×10^{-5} , respectively, Mann-Whitney U-test [MWU test]). Box plots represent median and 25/75 percentiles, squares represent the mean value, whiskers represent SD. All immunolabelings were normalized to PSD95 intensity on panels (F, G).
- (H) The Munc13-2 content of randomly selected synapses is only $4 \pm 7\%$ and $4 \pm 10\%$ (in two mice; p = 0 for both MWU test) of that of synapses on mGluR1 α + dendrites.
- (I–L) Munc13-2 immunolabeling (cyan) does not colocalize either with vesicular inhibitory amino acid transporter (VIAAT, red) (I, J, n = 152 Munc13-2 and 222 VIAAT positive profiles in 2 mice) or with vesicular glutamate transporter-2 (vGluT2, red) (K, L), n = 43 Munc13-2 and 33 vGluT2 positive profiles in 1 mouse). Single confocal images (I, K). str. oriens, stratum oriens. This figure was adopted from Holderith et al. (2022)

4.3. Munc13-2 Puncta Disappear in the Stratum Oriens of Elfn1 Knock out Mice

It has been shown that Elfn1 is selectively expressed in the SST/mGluR1 α + hippocampal INs (56) and recruits mGluR7 in the presynaptic AZ (189, 190). Knocking down Elfn1 is known to decrease STF (56). Here, we tested the effect of Elfn1 knockout on the selective expression of Munc13-2 in the presynaptic AZs targeting mGluR1 α + INs. After Elfn1 knockout, Elfn1/2 immunolabeling was clearly absent in the CA1 str. oriens and alveus (*Figure 9A & E*; 97.7% \pm 0.53% decrease in KO compared to the control littermate). Consistent with previous literature, Elfn1 KO resulted in reduced mGluR7 immunolabeling compared to heterozygous littermate controls (*Figure 9C & G*).

We found that Elfn1 knocking out results in the absence of Munc13-2 immunolabeling $(3.7\% \pm 1.7\% \text{ of control littermates}; n = 5 \text{ KO mice and n} = 4 \text{ control mice})$ compared to controls, where punctate Munc13-2 decorates mGluR1 α + dendrites (*Figure 9D & H*). The lack of both mGluR7 and Munc13-2 after Elfn1 knockout raises the question of whether the decrease in the facilitation and the increase in Pv in Elfn1 KO mice (56) is due to the absence of mGluR7 or Munc13-2 or both.

(The immunolabeling results were contributed by Noemi Holderith).

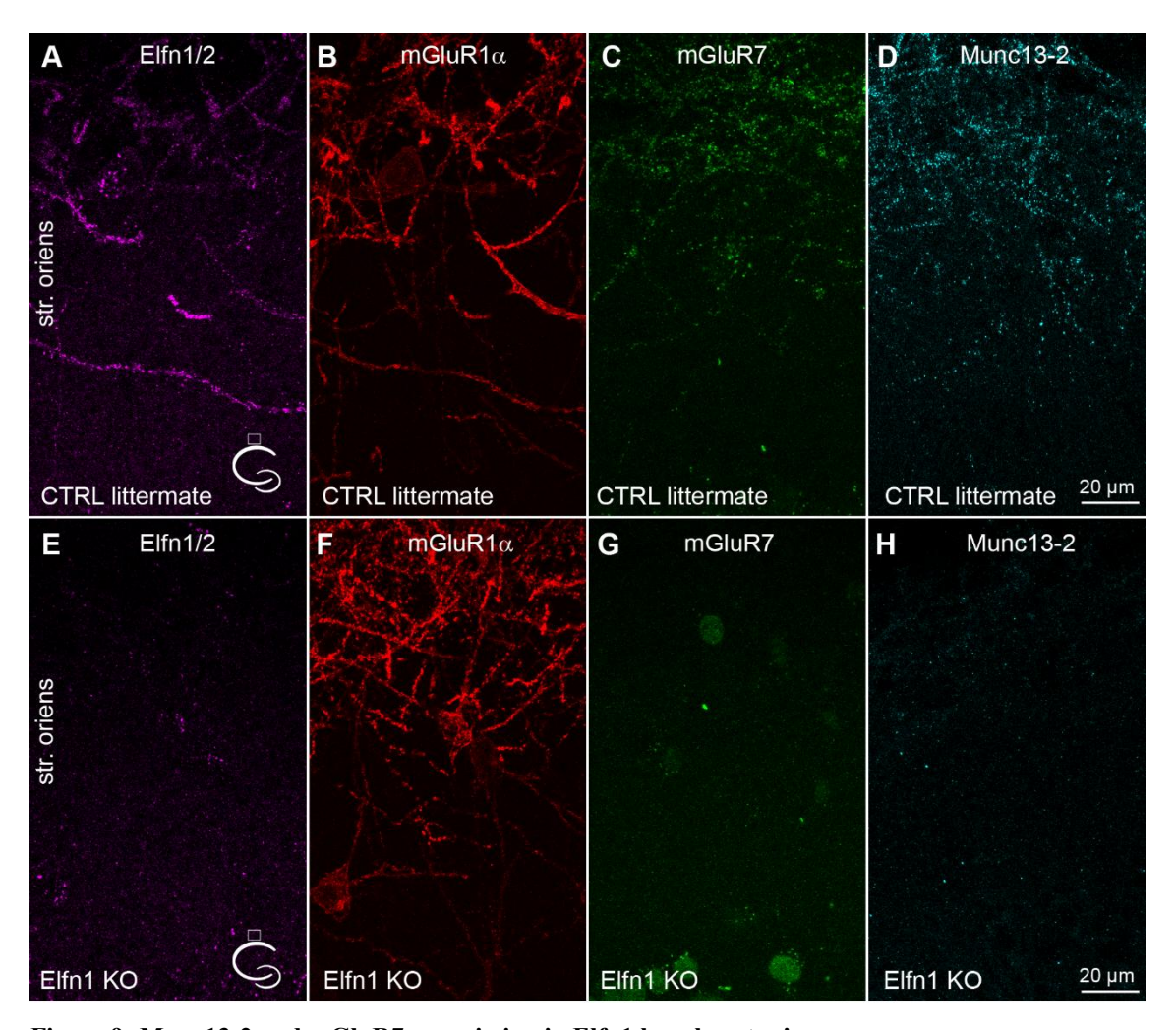


Figure 9: Munc13-2 and mGluR7 are missing in Elfn1 knock-out mice.

(A–D) Immunolabeling for Elfn1/2 (A), mGluR1α (B), mGluR7 (C) and Munc13-2 (D) in the dorsal CA1 region of a littermate control mouse shows intense labeling of IN dendrites in the str. oriens. (E–H) same as (A–D) in an Elfn1 KO mouse. No specific immunolabeling is detected for Elfn1/2 (E), mGluR7 (G) and Munc13-2 (H). Cartoons indicate the location of the region. Maximum intensity projection of 20 confocal images separated by 1 μm. str. oriens, stratum oriens. This figure was adopted from Holderith et al. (2022).

4.4. Conditional Knock out of Munc13-2 Does not Affect mGluR7 Expression

To investigate the role of Munc13-2 in synapses innervating mGluR1 α + dendrites, Munc13-2 was conditionally knocked out in hippocampal CA1 PCs. First, the immunolabeling of mGluR1 α and mGluR7 was assessed after Munc13-2 knockout. Later, the effect on evoked EPSCs at these synapses was also investigated. Cre-recombinase-expressing AAV was injected into the dorsal hippocampus. Two weeks later, Cre expression was visualized by Cre immunolabeling (*Figure 10*). In the central part of the injected area, most PCs were Cre positive, and the mGluR1 α + dendrite-associated specific immunosignal for Munc13-2 decreased by 92% \pm 10% in the str. oriens/alveus (n = 3 mice; *Figure 10F*). Despite the lack of Munc13-2, the expression pattern of mGluR1 α , Elfn1, mGluR7 and Munc13-1 did not change compared to non-injected contralateral control hemisphere (101 \pm 18%, 104 \pm 5%, 104 \pm 4%, 99 \pm 1% of controls, respectively; *Figure 10G-J* and Supplementary Figure 2G in Holderith et al. 2022).

(The immunolabeling results were contributed by Noemi Holderith)

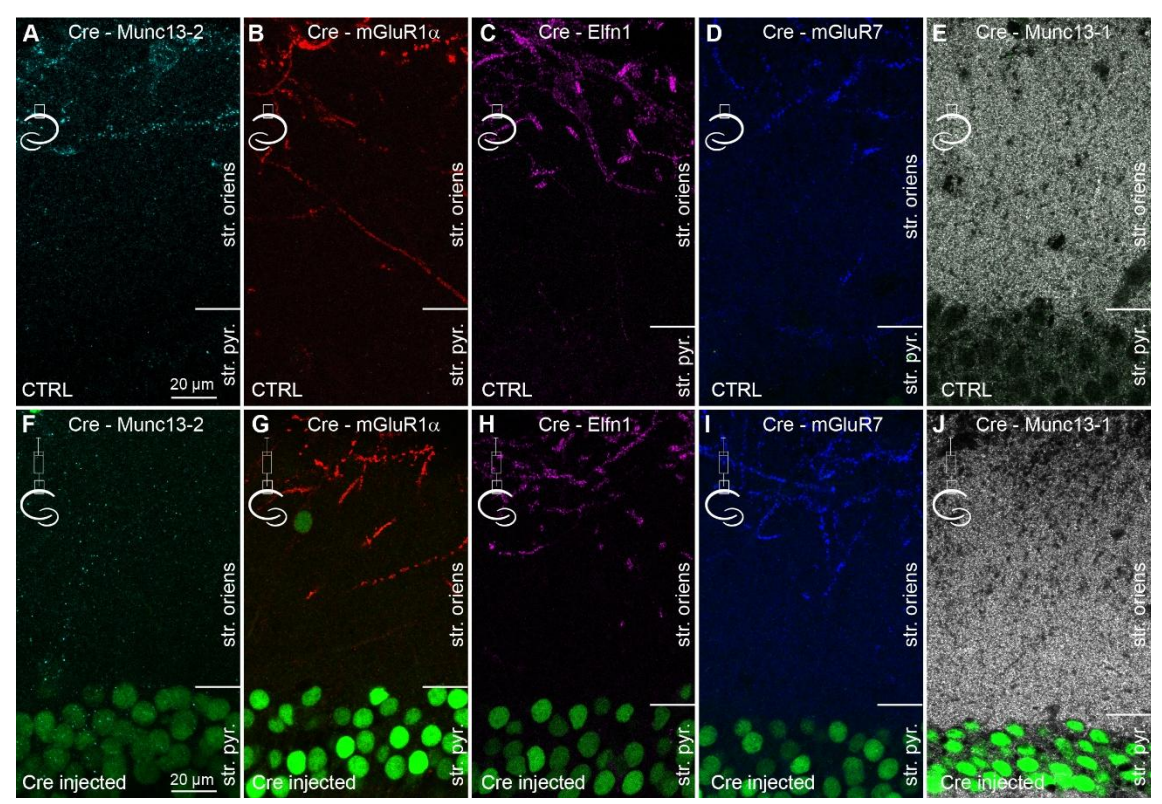


Figure 10: Conditional knock-out of Munc13-2 does not change the expression and distribution of Elfn1 and mGluR7.

(A–E) Double immunolabeling for Cre and either Munc13-2 (A) or mGluR1 α (B), or Elfn1 (C) or mGluR7 (D) or Munc13-1 (E) in the dorsal CA1 area of the non-injected hemisphere.

(F-J) Same as in (A-E), but the images are from the hemisphere that has been injected with AAV

expressing Cre-recombinase. Immunolabeled Cre (green) is visible in most CA1 PC nuclei (green). Note the lack of immunolabeling for Munc13-2 in the outer part of the stratum oriens, demonstrating the efficient removal of the protein, while there is no detectable change in the immunolabeling for mGluR1 α , Elfn1, mGluR7, and Munc13-1. Maximum intensity projection of 4 confocal images separated by 1 μ m. str. pyr, stratum pyramidale; str. oriens, stratum oriens. This figure was adopted from Holderith et al. (2022).

4.5. Knocking out Elfn-1 Increases eEPSCs at PC – O-LM IN Connections, while Munc13-2 Has no Obvious Role in Regulating Pv at These Synapses

To study the effect of Elfn1 knockout on PC – O-LM IN connections, paired whole-cell patch-clamp recordings were performed. Putative O-LM INs were selected based on somata location, size and their firing pattern in response to DC current injections. *Post-hoc* anatomical analysis of the filled INs revealed that 10 out of 14 INs had O-LM IN morphology (*Figure 11A*), while the remaining four had truncated axons but were mGluR1 α immunopositive (*Figure 11G*), all 14 INs were included in the study. The amplitude of the first eEPSC in Elfn1-KO mice was significantly larger (29 ± 28.9 pA, n = 14; *Figure 11C & D*) than in wild-type controls (9.6 ± 9.4 pA, n = 80; *Figure 11C & D* and Figure 7A, D & F). This 3-fold increase in the first eEPSC amplitude was accompanied by a decreased PPR (1.46 ± 0.41, n = 14; *Figure 11E*) compared to wild-type controls (2.19 ± 0.78, n = 66; in 14 pairs, the first eEPSC peak amplitude was 0 pA, precluding PPR calculation; *Figure 11E* and *Figure 7A & D-G*).

As discussed previously, the increase in eEPSCs after Elfn-1 knockout could result from the loss of mGluR7 and/or Munc13-2. To determine if Munc13-2 plays a role, we performed paired recordings from PC – O-LM/mGluR1 α + IN connections where Munc13-2 gene was conditionally knocked out using Cre- and mCherry-expressing AAVs. The morphology of the INs and their immunopositivity for mGluR1 α , as well as the Cre immunopositivity of the presynaptic PCs, were verified *post hoc* (*Figure 11F & G*). The first eEPSCs were small (6.7 ± 7.9 pA, n = 20 pairs), which was not significantly different from that in control (*Figure 11C & D*). These connections exhibited STF with a PPR of 2.3 ± 1.64 (n = 13; for 7 cell pairs, the amplitude of the first eEPSC peak was 0 pA, precluding PPR calculation; *Figure 11E*), which was not significantly larger than the PPR recorded for controls. This demonstrates that knocking out Munc13-2 has no obvious effect on eEPSCs at PC – O-LM IN synapses.

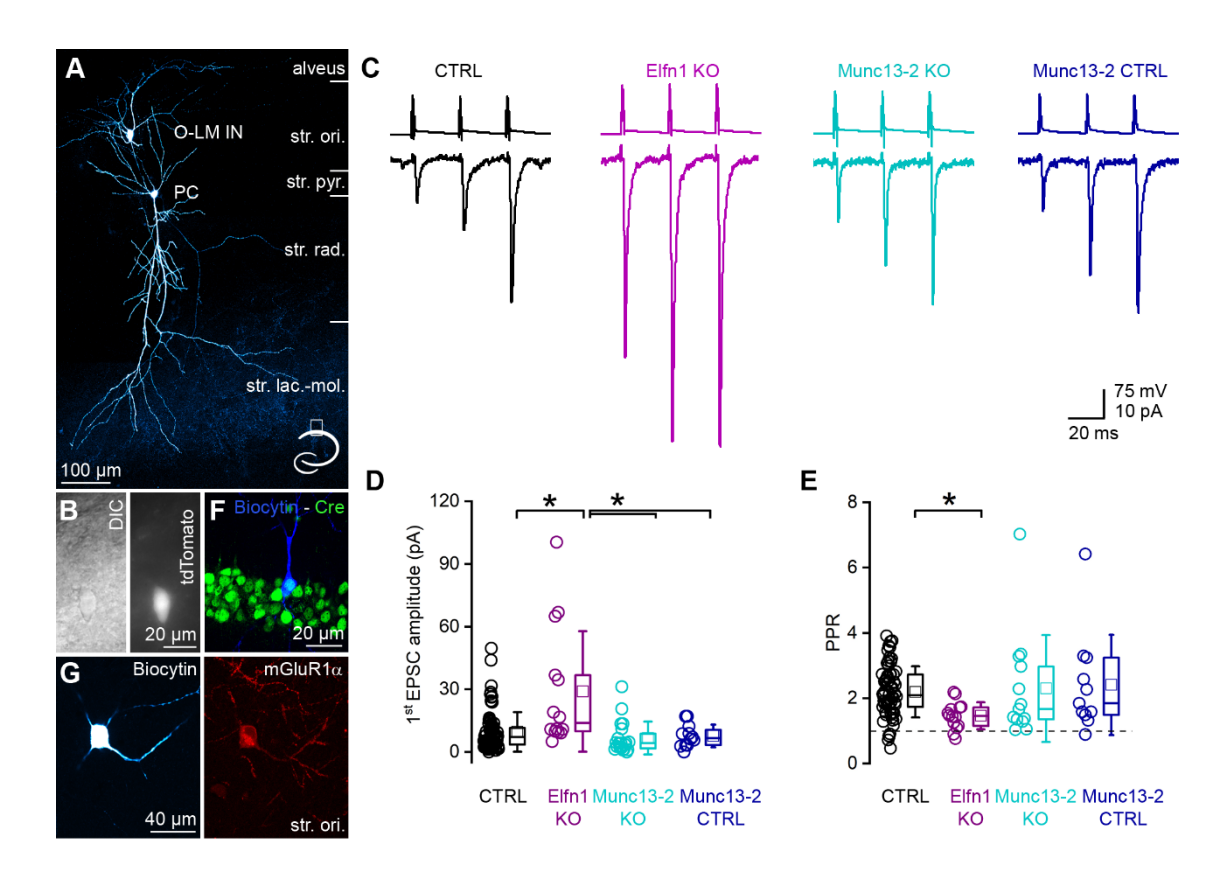


Figure 11: Removal of Munc13-2 does not change the peak amplitude and short-term plasticity of unitary EPSCs between CA1 PCs and mGluR1α expressing INs.

- (A) In vitro whole-cell patch-clamp recorded and biocytin filled CA1 PC and O-LM IN. The axonal arbor of the IN is visible in the stratum lacunosum-moleculare. Cartoon depicts the location of the cells within the hippocampus.
- **(B)** DIC image of the O-LM IN shown in panel (A) (left) and fluorescent tdTomato signal of the same cell (right).
- **(C)** Unitary EPSCs (lower traces) evoked by a train of 3 APs at 40 Hz in a presynaptic CA1 PC (upper traces) recorded in postsynaptic O-LM INs in the dorsal CA1 region of the hippocampus. Black traces are from a control, magenta traces from an Elfn1 knock-out, cyan traces from a Munc13-2 conditional knock-out, dark blue traces from a Munc13-2 conditional knock-out littermate control.
- **(D)** The first EPSC is significantly larger (*) in the Elfn1 knock-out mouse than in any of the controls or in the Munc13-2 conditional knock-out mice ($p = 5.44 \times 10^{-4}$, Kruskal-Wallis ANOVA, post hoc Dunn's test: p = 0.003, 0.00024, 0.041, ctrl vs. Elfn KO, Elfn KO vs. Munc13-2 KO, Elfn KO vs. Munc13-2 ctrl, respectively) while there is no change in the peak amplitude in the Munc13-2 conditional knock-out mouse compared to any of the controls (Kruskal–Wallis ANOVA, post hoc Dunn's test p = 0.49 and 1, ctrl vs. Munc13-2 KO, control vs. Munc13-2 control).
- (E) The short-term facilitation is significantly less pronounced in the Elfn1 knock-out mouse (p = 0.0065, Kruskal-Wallis ANOVA, post hoc Dunn's test: p = 0.0034, ctrl vs. Elfn knock-out) while there is no change in the short-term plasticity in the Munc13-2 conditional knock-out mouse compared to any of the controls (Kruskal-Wallis ANOVA, post hoc Dunn's test, p = 1, ctrl vs. Munc13-2 KO, Munc13-2 KO vs. Munc13-2 control).
- **(F)** In vitro recorded and biocytin filled PC (blue) expressing Cre-recombinase (green) that is localized to the PC nucleus. Single confocal image.
- (G) A biocytin filled IN with truncated axon (left) expresses mGluR1α (right red). Maximum intensity

projection of four confocal images separated by 1 μ m. Box plots represent median and 25/75 percentiles, square represent the mean value, whiskers represent SD. str. ori., stratum oriens, str. pyr., stratum pyramidale, str. rad., stratum radiatum, str. lac.-mol., stratum lacunosum-moleculare. This figure was adopted from Holderith et al. (2022).

These findings suggest that although Munc13-2 is preferentially localized to glutamatergic synapses innervating O-LM IN dendrites, it does not seem to be a key determinant of the lower Pv observed at these synapses compared to PC - FSIN synapses. Therefore, the investigation shifted to explore VGCC density and the resulting $[Ca^{2+}]$ influx involved in SV fusion at the PC AZs targeting O-LM INs and FSINs.

4.6. Larger Densities of VGCCs Surround Release Sites in FSIN versus O-LM IN-Targeting AZs

To investigate whether differences in VGCC densities around RSs contribute to the distinct Pvs observed at FSIN versus O-LM IN synapses, we performed freeze-fracture replica immunolabeling for the Cav2.1 subunit (P/Q-type VGCC) and Munc13-1, as a marker for RSs in the AZs (214, 215). While Ca_V2.2 (N-type) is another prominent VGCC subunit in CA1 PC synapses, unfortunately, it cannot be efficiently localized using EM SDS-FRL. Therefore, the role of Cav2.2 was probed by recording from PC – FSIN and PC – O-LM IN pairs after blocking Cay2.2 with 1 μM ω-Conotoxin GVIA. In PC – FSIN connections, the first eEPSC peak amplitude was reduced by 20% by ω-Conotoxin (BSA control: $126.7 \pm 101.4 \text{ pA}$, n = 17; ω -conotoxin: $103.7 \pm 120.7 \text{ pA}$, n = 18; Figure 12 B-C), while the PPR remained similar (control: 0.92 ± 0.31 ; BSA control: 1.00 ± 0.34 ; ω conotoxin: 1.02 ± 0.37). The PC – O-LM IN eEPSC peak amplitude in ω -Conotoxin was 5.7 ± 0.4 pA (n = 5; Figure 12A & C), still showing more than an 18-fold larger EPSC in PC – FSIN connections. This indicates that the two synapse types still exhibit different Pvs even when Ca²⁺ influx is primarily mediated by the P/Q-type (Cav2.1) subunit. Furthermore, it suggests that the proximity between Cav2.2 subunits and SVs cannot explain the higher Pv observed at PC – FSIN synapses.

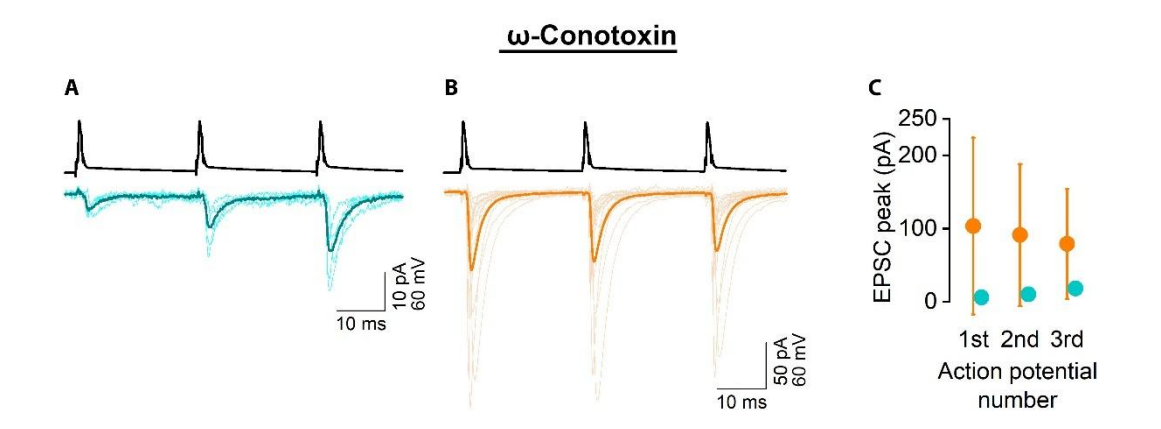


Figure 12: Distinct EPSC amplitudes and short-term plasticity of CA1 PC – FSINs vs. PC – O-LM cell synapses even in the presence of 1 μ M ω -conotoxin to block N-type Ca²⁺ channels.

(A and B) Averaged postsynaptic responses evoked by three action potentials (at 40 Hz) in presynaptic PCs are shown in O-LM cells (A, thin traces: 5 individual pairs; thick trace: the average of 5 pairs) and FSINs (B, thin traces: 16 individual pairs; thick trace: the average of 18 pairs). The amplitude of the first eEPSCs and the short-term plasticity of the responses show large variability within groups but are considerably different between O-LM cells and FSINs.

(C) The amplitudes (mean \pm SD) of the eEPSCs in O-LM IN (n = 5 pairs) and FSINs (n = 18 pairs) are shown for the three consecutive APs. This figure was adopted from Aldahabi et al. (2022).

The distribution of Munc13-1 and Ca_V2.1 was investigated in AZs targeting FSINs or O-LM INs using SDS-FRL. The mirror replica method was used in which extracellular and protoplasmic plasma membrane faces (EF & PF) of the same structure can be identified and labeled in replica pairs (*Figure 13*). In one replica, gold particles labeling voltage-gated potassium channels Kv3.1b was used to mark FSIN postsynaptic membranes or mGluR1 α for O-LM INs membranes. In the corresponding replica, Munc13-1 and Ca_V2.1 proteins were localized in AZs fractured from axon terminals targeting FSIN (*Figure 13A-D*) and O-LM IN somato-dendritic membranes (*Figure 13E-K*).

The enrichment of intramembrane proteins in the AZs of the PF plasma membrane enabled the demarcation of the AZs. The area of AZs targeting mGluR1 α somatodendritic regions (0.10 \pm 0.048 μ m², n = 118) was 43% larger than that of AZs targeting Kv3.1b-positive regions (0.07 \pm 0.035 μ m², n = 159; *Figure 14A*). Further analysis of Munc13-1 gold particles revealed similar Munc13-1 densities in both AZ populations (*Figure 14B*). Clustering of Munc13-1 molecules at individual AZs was observed (Ripley's analysis), with 66% and 81% of AZs contacting Kv3.1b- and mGluR1 α -positive dendrites, respectively, exhibiting gold particle distributions significantly different from random (*Figure 14C & 13K*).

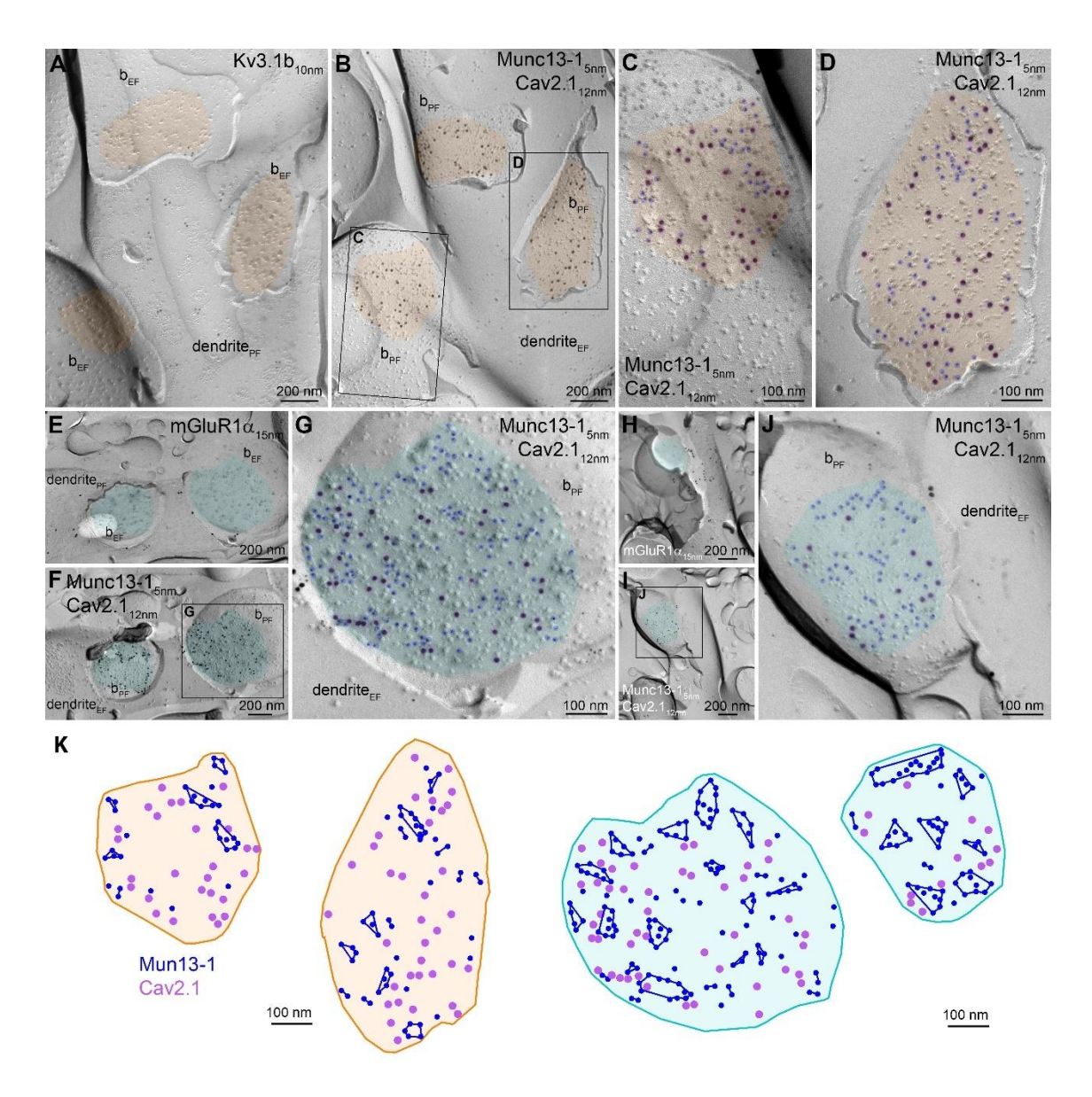


Figure 13: Freeze-fracture replica immunolabeling of Munc13-1 and Cav2.1 in excitatory synapses on Kv3.1b+ and mGluR1 α + INs

- (A) Low magnification image of the protoplasmic membrane face (PF) of a Kv3.1b+ dendrite (dendrite_{PF}) targeted by three excitatory boutons (b_{EF}) with fully exposed AZs (highlighted in orange).
- **(B)** The mirror replica of that shown in (A) immunolabeled for Munc13.1 and $Ca_V 2.1$. Gold particles are concentrated in the AZs (orange) on the PF membrane of the boutons (b_{PF}).
- (C and D) High magnification images of the boxed areas in (B) showing a small (C) and a large (D) AZ. Gold particles are highlighted in blue (Munc13-1) and purple ($Ca_V 2.1$).
- (E–J) Low (E, F, H, I) and high (G, J) magnification replica images immunolabeled for mGluR1 α , Munc13-1, and Ca_V2.1. (E) and (F), (H) and (I) are mirror replica images of the same dendrites. AZ areas are shown in cyan; gold particles are highlighted in blue (Munc13-1) and purple (Ca_V2.1).
- (K) Delineated AZs on Kv3.1b+ (orange) and mGluR1 α + (cyan) dendrites (original images shown in C, D, G and J) showing gold particles labeling Ca_V2.1 (purple) in relation to Munc13-1 clusters (blue). Clustering was performed with DBSCAN. This figure was adopted from Aldahabi et al. (2022).

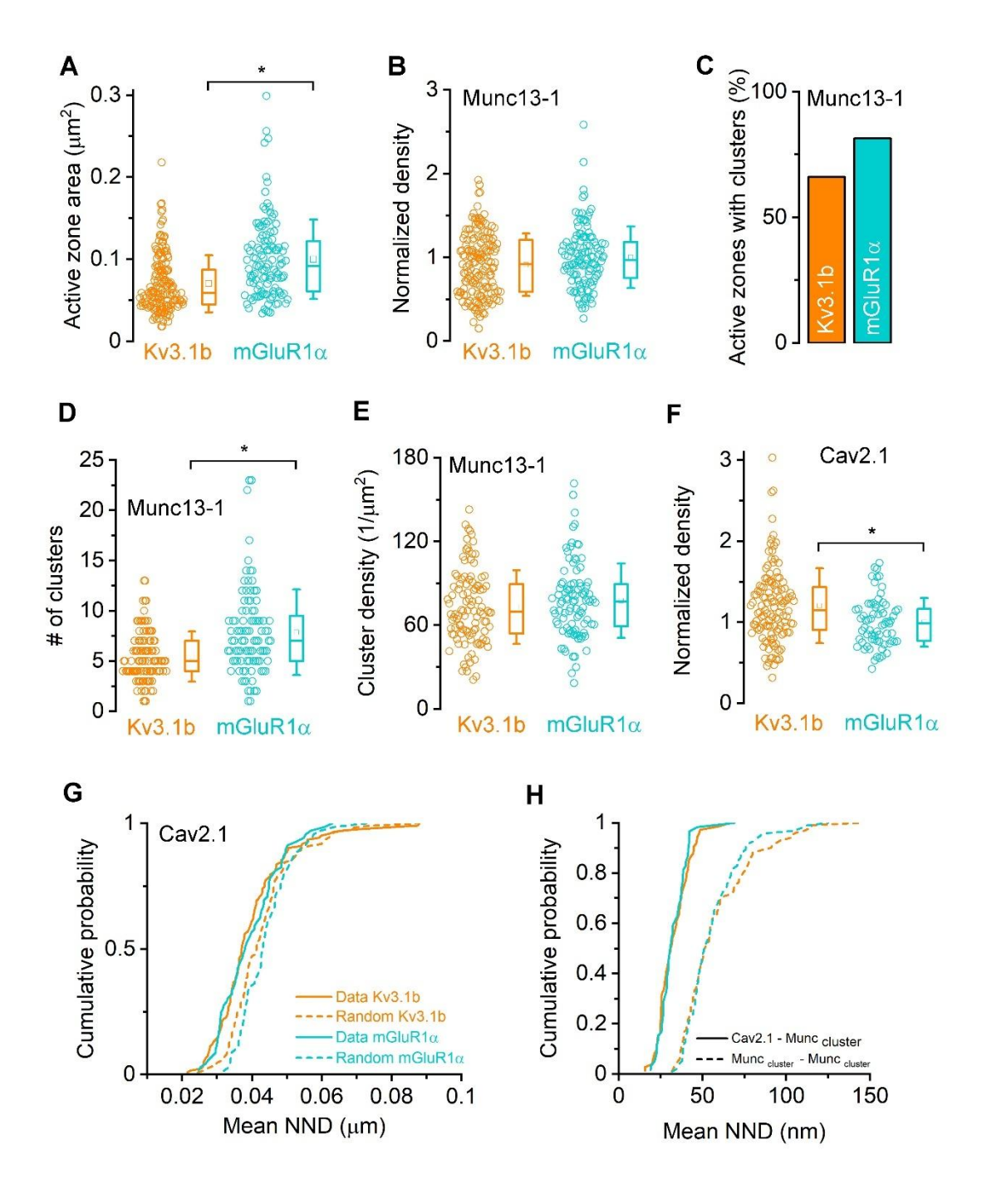


Figure 14: Quantitative analysis of Munc13-1 and Cav2.1 immunolabeling in AZs synapsing on Kv3.1b+ and mGluR1 α + INs

- (A) The AZs are significantly (p = 7E-9, MWU test) larger on mGluR1 α + INs (0.10 \pm 0.048 μ m², n = 118) than on Kv3.1b+ cells (0.07 \pm 0.035 μ m², n = 159).
- **(B)** The normalized density of Munc13-1 immunolabeling is similar (p = 0.081, MWU test) in both synapse populations.
- (C) Ripley analysis of individual synapses demonstrates that Munc13-1 gold particles are clustered (p < 0.05, maximum absolute deviation [MAD] test) in 66% and 81% of the AZs on Kv3.1b+ (n = 159) and mGluR1 α + (n = 118) dendrites, respectively.
- (D) The number of Munc13-1 clusters is significantly (p = 4E-6, MWU test) larger in mGluR1 α + (7.9 \pm

- 4.3, n = 96) than in Kv3.1b+ (5.4 ± 2.5, n = 105) dendrites contacting AZs.
- (E) The Munc13-1 cluster density does not differ in the two AZ populations (p = 0.24, MWU test).
- (F) The density of gold particles labeling $Ca_V 2.1$ is significantly (p = 1.6E-3, MWU test) larger in AZs contacting Kv 3.1b+ dendrites.
- (G) Cumulative probability plots of the mean NNDs of gold particles labeling $Ca_V 2.1$ (data, solid lines) and those of randomly placed particles (dashed lines). The mean NNDs of the data are significantly (p < 0.001, WSR test with HBC) different from randomly distributed gold particles within the same AZ population, but they are comparable between the two AZ populations (p = 0.695, MWU test with HBC). (H) The mean NNDs between $Ca_V 2.1$ gold particles and the edges of Munc13-1 clusters are significantly shorter (p < 0.0001 for both synapse populations, MWU test with HBC) than those between the Munc13-
- shorter (p < 0.0001 for both synapse populations, MWU test with HBC) than those between the Munc13-1 clusters in both synapse populations (orange: Kv3.1b+, cyan: mGluR1 α +). This figure was adopted from Aldahabi et al. (2022).

Cluster counts showed an average of 5.4 ± 2.5 (n = 105 AZs) and 7.9 ± 4.3 (n = 96 AZs) clusters per AZ on Kv3.1b- and mGluR1 α -positive structures, respectively (*Figure 14D*). This difference in cluster numbers is fully explained by the difference in AZ area, as the Munc13-1 cluster densities in these AZ populations are comparable (*Figure 14E*). Nevertheless, the distribution of Cav2.1 VGCCs surrounding these presumed RSs remains to be investigated.

Analysis of Cav2.1 subunit density revealed a slight, but statistically significant, increase in Cav2.1 density at AZs targeting Kv3.1b-positive INs (normalized density: 1.2 ± 0.46 , n = 123) compared to mGluR1 α -targeting AZs (normalized density: 1.0 ± 0.3 , n = 69; Figure 14F), consistent with prior observations in the CA3 region of juvenile rats (186). This difference in Cav2.1 density may contribute to a higher $[Ca^{2+}]$ influx and, consequently, a higher Pv at these synapses. To further investigate Cav2.1 distribution and its proximity to RSs, we measured the mean nearest neighbor distances (NNDs) between Cav2.1 gold particles and either Cav2.1 or Munc13-1 clusters in both AZ types. The NND cumulative distribution plots (Figure 14G, orange & cyan solid lines) demonstrated that the overall distribution of Cav2.1 subunits was similar between the two AZ populations. Similarly, the distances of Cav2.1 relative to Munc13-1 clusters also showed similar distributions (Figure 14H, orange & cyan solid lines) in both AZ populations. This indicates a consistent distribution of Cav2.1 subunits around RSs in both AZs, with a slightly higher overall density of Cav2.1 subunits in AZs targeting FSIN dendrites.

(The EM SDS-FRL results were contributed by Andrea Lorincz).

4.7. Differential [Ca²⁺] Influx is not the Primary Driver of Synaptic Strength Differences

To assess the impact of the higher Cav2.1 channel density observed at FSIN-targeting synapses compared to OLM-targeting synapses, two-photon [Ca²⁺] imaging was conducted in local axon collaterals of CA1 PCs within acute in vitro slices. The goal was to determine whether a reduced [Ca²⁺] influx at boutons targeting O-LM INs contributes to the lower Pv measured at PC - O-LM IN synapses. Fluo5F was introduced intracellularly, and AP-evoked [Ca²⁺] transients were recorded (Figure 15 A-C). Subsequent identification of the postsynaptic target of the imaged boutons enabled classification as PV+- or mGluR1α+- targeting boutons (Figure 15 I-K). Comparison of the [Ca²⁺] transients between the two synapse types revealed a 38% larger [Ca²⁺] transient in boutons targeting PV+ dendrites compared to those targeting mGluR1 α + dendrites (PV: $0.22 \pm 0.08 \text{ G/G}_{max}$, n = 16 boutons; mGluR1 α : $0.16 \pm 0.06 \text{ G/G}_{max}$, n = 25 boutons; Figure 15 L & M). To investigate this further, we modulated the lower $[Ca^{2+}]$ transient observed at PC – O-LM IN boutons using 4-aminopyridine (4-AP), a voltage-gated K⁺ channel blocker known to strongly increase AP-evoked [Ca²⁺] (216). Application of 5 µM 4-AP increased the $[Ca^{2+}]$ transient at mGluR1 α -targeting boutons from 0.16 ± 0.06 G/G_{max} to 0.24 ± 0.06 G/G_{max} (n = 12), effectively matching the [Ca²⁺] transient observed at PV-targeting boutons (Figure 15 L & M).

(The two-photon [Ca²⁺] imaging results were contributed by Noemi Holderith).

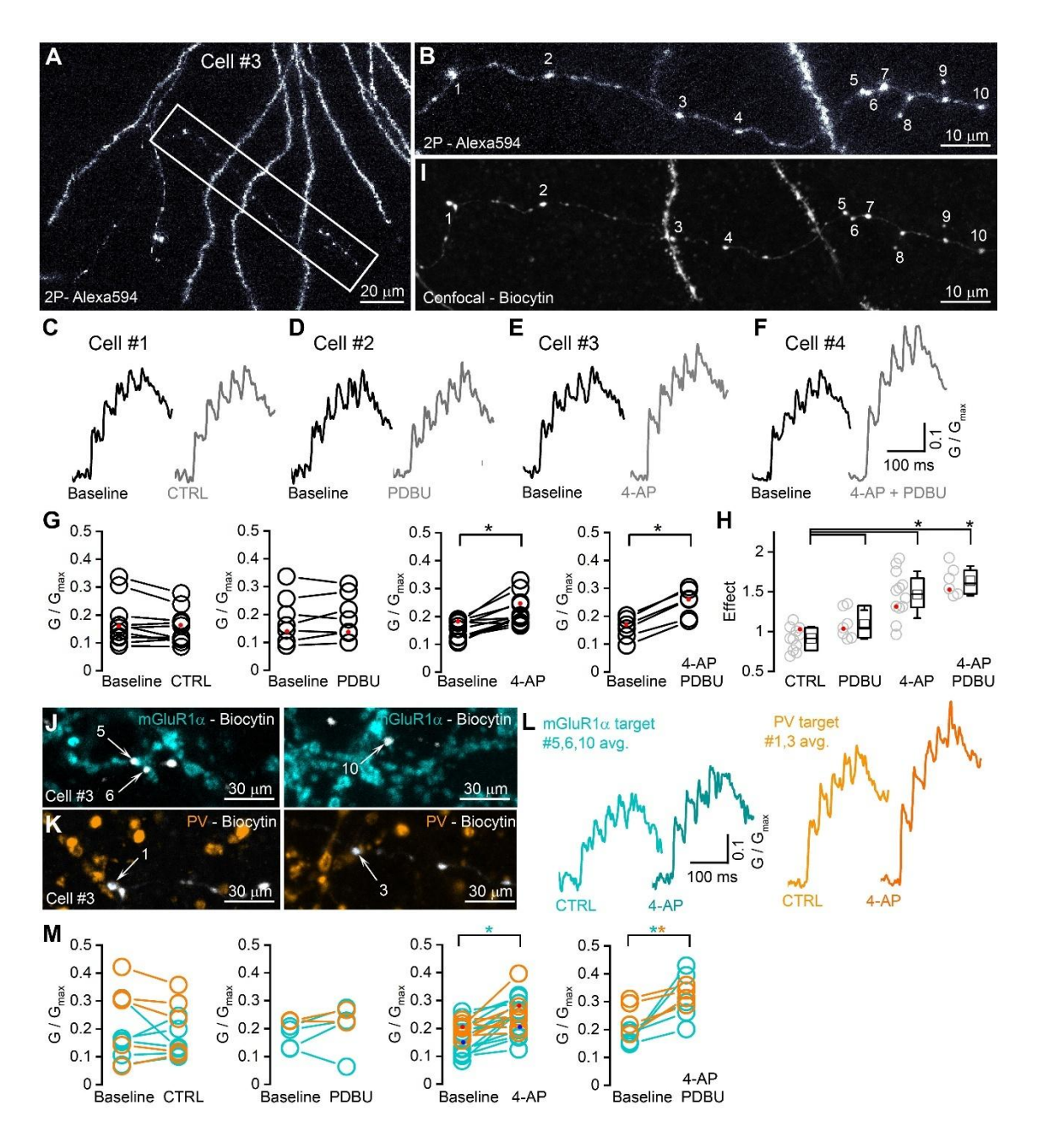


Figure 15: Effects of PDBU and 4-AP on the amplitudes of $[Ca^{2+}]$ transients recorded from CA1 PC boutons targeting PV+ or mGluR1 α + INs

- (A) Two-photon (2P) image stack of a CA1 PC (Cell #3) basal dendritic tree and axonal arbor filled with 20 μ M Alexa Fluor 594 (white), 200 μ M Fluo5F, and biocytin. Boxed area indicates the part of the imaged axonal arbor and is shown at higher magnification in (B).
- **(B)** High magnification 2P image of the scanned axon collateral. Numbers indicate scanned boutons.
- (C) Averaged [Ca²⁺] transients evoked by 5 action potentials at 40 Hz in local axon collaterals of a CA1 PC (Cell #1, trace is average of 17 boutons, black). Each bouton was scanned at the beginning of the imaging period (Baseline, black) and 30 min later (CTRL, gray) without perfusing any drug.
- (D–F) Same as (C) for Cells #2–4 but, after a control imaging period (Baseline), 1 μ M PDBU (D), 5 μ M 4-AP (E), or both (F) were applied (average trace from 9, 12, and 21 boutons, respectively).
- (G) Peak amplitudes of [Ca²⁺] transients for the first action potential do not change in CTRL and in

PDBU but increase significantly following the application of 4-AP and 4-AP + PDBU (WSR test, p = 0.10, 0.35, 0.003, 0.036, respectively). Data points represent individual cells (CTRL: n = 11; PDBU: n = 7; 4-AP: n = 12; 4-AP + PDBU: n = 6). Red dots indicate the cells shown in (C-F).

- **(H)** KW test with post hoc Dunn's test demonstrates that 4-AP (p = 0.0009) and 4-AP + PDBU (p = 0.0003) have significant effects on the peak amplitudes of $[Ca^{2+}]$ transients compared to control, while PDBU does not change the transients significantly (p = 1). Data points represent individual cells (CTRL: n = 11; PDBU: n = 7; 4-AP: n = 12; 4-AP + PDBU: n = 6). Red dots indicate the cells shown in (C-F).
- (I) Maximum intensity projection of a confocal image z stack showing the imaged boutons after fixation and the visualization of biocytin. Each imaged bouton can be unequivocally identified.
- (J and K) Some of the imaged boutons are in direct contact with mGluR1 α + (J, #5, 6, 10) or PV+ (K, #1, 3) dendrites.
- (L) Averaged $[Ca^{2+}]$ transients evoked by 5 action potentials at 40 Hz in boutons #5, 6, and 10 targeting mGluR1 α + (cyan CTRL, dark cyan 4-AP) and in boutons #1 and 3 targeting PV+ dendrites (CTRL, light orange, 4-AP, dark orange). $[Ca^{2+}]$ transients are smaller in boutons targeting mGluR1 α + dendrites. (M) Peak amplitudes of averaged $[Ca^{2+}]$ transients in response to the first action potential in boutons with identified postsynaptic partners (cyan mGluR1 α +, orange PV+) in CTRL and in the presence of drugs (CTRL: p = 0.87 and 0.50, n = 6 and 5 cells; PDBU: p = 0.42, n = 4 cells only for mGluR1 α +; 4-AP: p = 0.0012 and 0.06, n = 12 and 11 cells; 4-AP + PDBU: p = 0.031 and 0.032, n = 5 and 4 cells for mGluR1 α + and PV+ INs, respectively, paired t test). Red and blue dots indicate data from Cell #3. Horizontal lines in the boxplots: 25th, 50th, and 75th percentiles, rectangle: mean, whiskers: SD. This

figure was adopted from Aldahabi et al. (2022).

To assess the effect of increased [Ca²⁺] influx on SV release, evoked EPSCs were measured using whole-cell paired recordings of both connection types following 4-AP wash-in (*Figures 16 & 17*). Five μ M 4-AP increased eEPSCs by only 50% at PC – FSIN synapses (from 139.2 ± 150.7 pA to 175.1 ± 141.7 pA, n = 12 pairs; *Figure 16C*). In contrast, eEPSCs at PC – O-LM INs increased 2.7-fold (from 11.0 ± 13.0 pA, median 5.2 pA to 21.6 ± 16.6 pA, median 16.8 pA, both rundown corrected (see Methods), n = 11 pairs; *Figures 17 B & E*), but the eEPSC amplitude remained more than 5-fold smaller than PC – FSIN connections (142.9 ± 145.9 pA). This indicates that the difference in [Ca²⁺] transients does not fully explain the difference in *Pv* between these two synapses. This result argues against the hypothesis that P_{fusion} is the primary cause of the difference in *Pv*. The differential impact of 4-AP on PC – O-LM IN versus PC – FSIN connections suggests a greater capacity for increased [Ca²⁺] influx to enhance P_{fusion} at O-LM synapses, indicating a comparatively lower baseline P_{fusion} at O-LM than at FSIN synapses.

(The electrophysiology data in Figure 16 were contributed by Flora Balint).

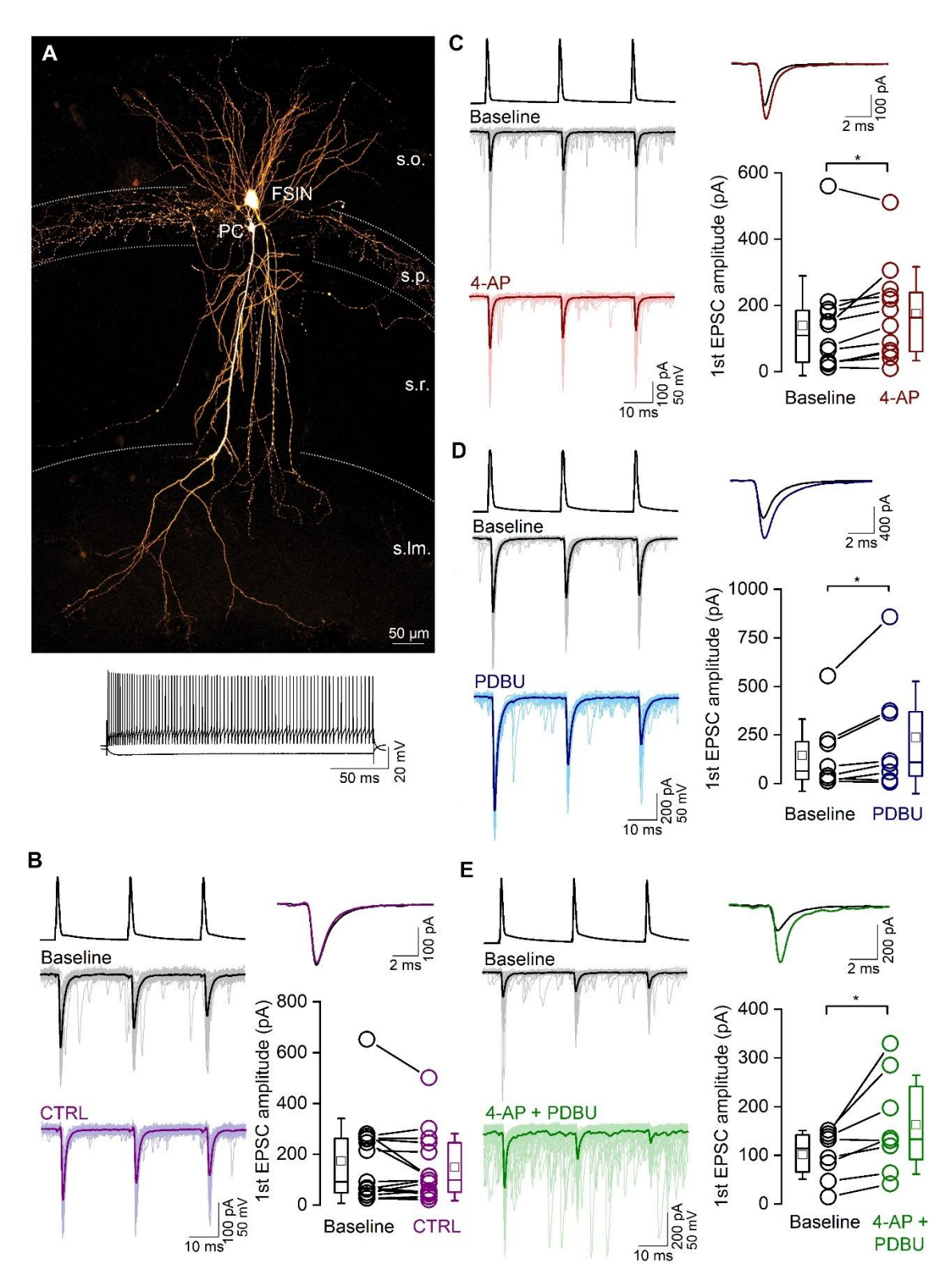


Figure 16: Synaptic responses between CA1 PCs and FSINs have moderate sensitivity to PDBU and 4-AP

(A) Confocal maximum intensity projection image of a biocytin-filled, synaptically connected PC – FSIN pair in the hippocampal CA1 region (top). Membrane potential responses of the IN to depolarizing and

hyperpolarizing current pulses are shown demonstrating the FS firing characteristic of the cell (bottom). s.o., stratum oriens; s.p., stratum pyramidale; s.r., stratum radiatum; s.lm., stratum lacunosum-moleculare. (B) Individual (thin traces) and their averaged (thick trace) unitary EPSCs evoked by three action potentials at 40 Hz are shown from the beginning (gray) and end (purple) of the recording period from the same pair (left). Superimposed averaged traces of the first eEPSCs at the beginning (black) and end (purple) of the recording (top, right). The amplitude of the first eEPSCs is unchanged at the beginning and end of a 30-min-long recording period without any drug application (bottom right; baseline: mean of 60 traces, 0–10 min; control (CTRL): mean of 60 traces, 20–30 min; p = 0.51, WSR test, n = 15 pairs in 15 mice). (C–E) Same as (B), but either 5 μ M 4-AP (red, C), the phorbol ester analog PDBU (1 μ M, blue, D), or both (green, E) were applied to the slice after a 10-min baseline (black) recording period. All treatments significantly increased the amplitude of the first eEPSC (50% \pm 59%, 77% \pm 115% and 70% \pm 61%, n = 12, 8, and 8 pairs; in 11, 8, and 8 mice, p = 0.025, 0.04, and 0.02 WSR test, respectively). Horizontal lines in the boxplots: 25th, 50th, and 75th percentiles, rectangle: mean, whiskers: SD. This figure was adopted from Aldahabi et al. (2022).

4.8. Differential Synaptic Vesicle Priming States Impact Release Probability More Prominently

4.8.1. Similar Docked Vesicles Densities in AZs Innervating FSIN and O-LM IN

Given that the fusion probability of SVs is not the primary factor responsible for the low Pv at PC – O-LM IN synapses, the other potential contributing factor to the difference in Pv is the low occupancy of RSs by SVs. This possibility was investigated using EM tomography to identify whether an SV is in direct contact with the intracellular membrane leaflet of the plasma membrane. These INs were filled with biocytin and subsequently processed for EM imaging. Tilt image series were acquired for tomography, and the AZs innervating FSIN or O-LM INs were identified (*Figure 18 A & B*). Similar docked SV densities were found in AZs innervating FSIN ($136 \pm 35 \text{ SV/}\mu\text{m}^2$, n = 68 AZs in 3 mice) and O-LM cells ($145 \pm 41 \text{ SV/}\mu\text{m}^2$, n = 63 AZs in 3 mice; *Figure 18C*). The distribution of vesicles within 100 nm from the AZs was also compared, revealing similar distribution profiles in both synapse populations. No difference was detected in spatial densities either (*Figures 17 D & E*). Our EM data clearly demonstrates that RSs are similarly occupied by SVs at PC – FSIN and PC – O-LM cell synapses.

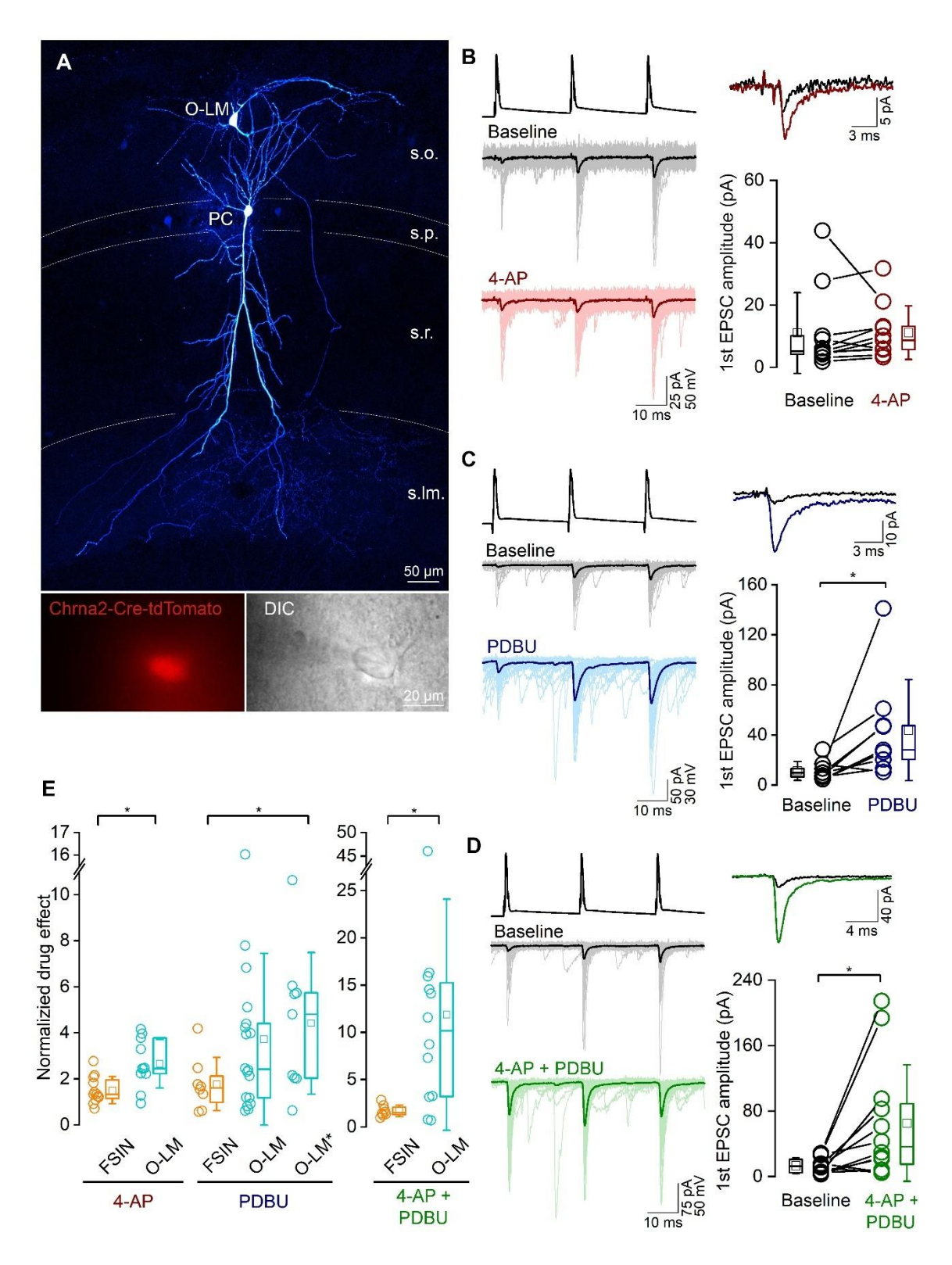


Figure 17: Robust PDBU sensitivity of unitary EPSCs in O-LM INs.

(A) Confocal maximum intensity projection image of a biocytin-filled, synaptically connected PC-O-LM IN pair in the hippocampal CA1 region (top). Note the extensive axonal arbor of the O-LM IN in the stratum lacunosum moleculare (s.lm.). Bottom left: epifluorescent image of a tdTomato-positive IN, acquired prior to patching. Bottom right: DIC image of the same IN, with the patch pipette.

- (B) Individual (thin traces) and the averaged (thick traces) unitary EPSCs evoked by three action potentials at 40 Hz are shown for the baseline (gray) and after 4-AP wash-in (red) of the recording period from the same pair (left). Superimposed averaged traces of the first eEPSCs at the beginning (black) and end (dark red) of the recording are on the top, right. The amplitude of the first eEPSCs is not significantly different at the beginning of the recording and after the application of 5 μ M 4-AP (bottom right; baseline: mean of 60 traces, 0–10 min; 4-AP: mean of 60 traces, 20–30 min; p = 0.17, WSR test, n = 11 pairs in 9 mice). Presynaptic PCs were recorded in whole-cell configuration.
- (C) Same as (B) but showing the effect of 1 μ M PDBU on eEPSCs in O-LM cells. PDBU significantly increased the amplitude of first eEPSCs of the train (n = 9 pairs in 9 mice; p = 0.013 WSR test). Presynaptic PCs were recorded in perforated patch configuration.
- **(D)** Same as (B) but demonstrating the effect of simultaneous application of PDBU and 4-AP (n = 12 pairs, in 11 mice, p = 0.009, WSR test). Presynaptic PCs were recorded in whole-cell configuration.
- (E) Summary of the effects of different drugs on the amplitude of first eEPSCs recorded from O-LM cells and FSINs. Plots show normalized drug effects, corrected to the rundowns measured in control recordings for O-LM, but not for FSIN or for O-LM* (see Figure 16B and Supplementary Figure 2A & 2D in Aldahabi et al. (2022)). All data, apart from O-LM*, were obtained with presynaptic PCs recorded in the whole-cell configuration. Data indicated with O-LM* were obtained with PCs recorded in the perforated patch configuration. Statistical comparison between FS and O-LM was assessed with MWU test (p = 0.007 in 4-AP, p = 0.16 in PDBU [FS vs. O-LM], p = 0.024 in PDBU [FS vs. O-LM*], p = 0.015 in 4-AP + PDBU). Horizontal lines in the boxplots: 25th, 50th, and 75th percentiles, rectangle: mean, whiskers: SD. This figure was adopted from Aldahabi et al. (2022).

4.8.2. Differential Effect of PDBU Indicates Distinct Priming in PC – FSIN vs PC – O-LM IN Synapses

Given that EM data clearly demonstrate similar SV occupancy at RSs in PC – FSIN and PC – O-LM cell synapses, we aimed to selectively manipulate SV priming at both synapse types. We applied the phorbol ester analog PDBU (1 μ M), which increases the activity of the SV priming molecule Munc13 (137). Consistent with the high Pv at PC – FSIN synapses, PDBU increased eEPSCs by only 77% \pm 115% (*Figure 16D*) and reduced the PPR from 0.97 \pm 0.40 to 0.72 \pm 0.37 (n = 8). Conversely, PDBU increased eEPSCs at PC – O-LM IN synapses by 4.4 \pm 3.1-fold (from 11.4 \pm 7.5 pA to 43.9 \pm 40.2 pA, n = 9; *Figure 17 C & E*, data from perforated patch-clamp recordings). This 4.4-fold increase induced by PDBU, in conjunction with the previously reported 2.5-fold increase by 4-AP, predicts an ~11-fold increase in eEPSCs amplitude when both drugs are applied concurrently. Experimental validation of this prediction revealed an 11.9 \pm 12.2-fold increase (n = 12; *Figure 17D & E*; whole-cell recording and rundown corrected). This additive effect of 4-AP and PDBU suggests distinct mechanisms of action for each drug, with selective effects on P_{fusion} and P_{occ} , respectively. These findings indicate that SVs

exist in different priming states at PC – FSIN compared to PC – O-LM IN synapses, as evidenced by our pharmacological experiments.

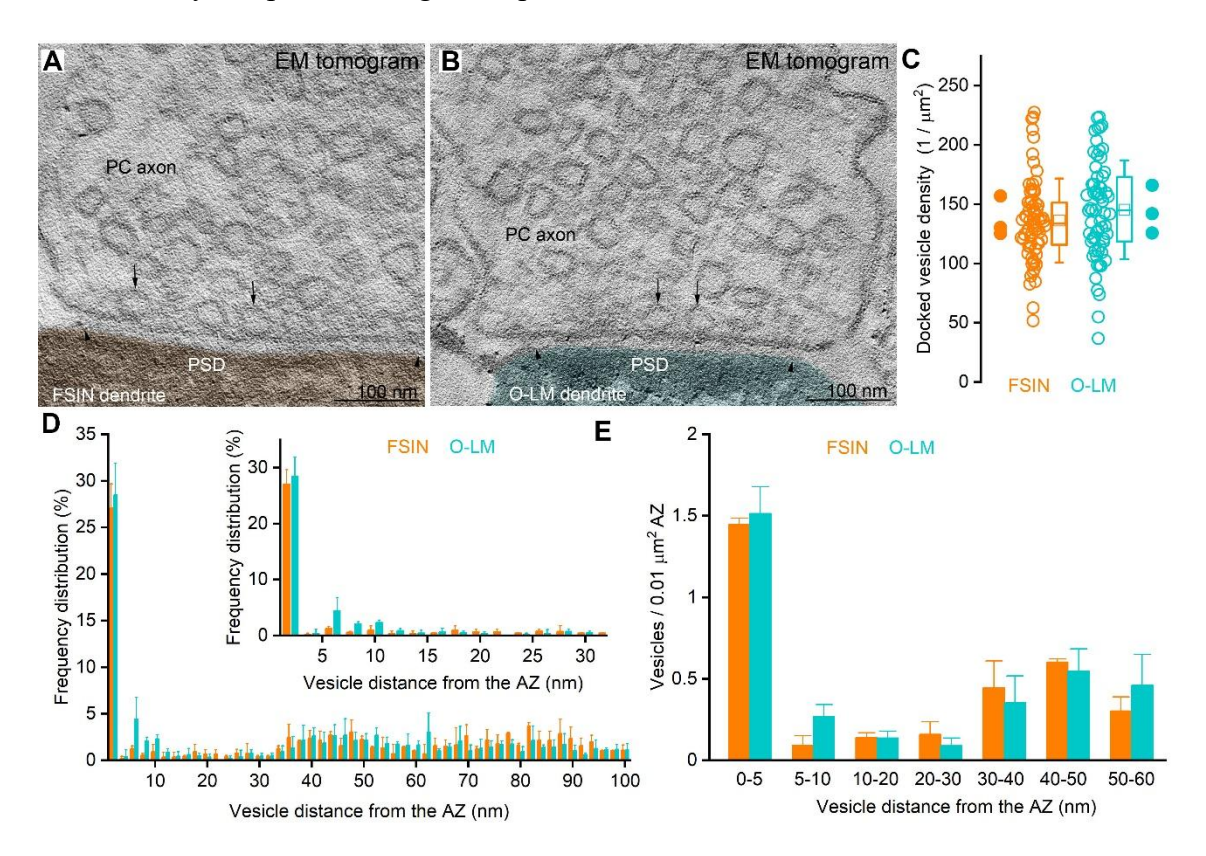


Figure 18: EM tomography reveals similar densities of docked vesicles in AZs innervating O-LM and FSINs.

(A and B) Electron tomographic subvolumes (0.6 nm thick) of representative excitatory synapses on an FSIN (A, orange) and O-LM IN (B, cyan) dendrite. Arrowheads demarcate the edges of the synapses; arrows point to docked vesicles.

- (C) Docked vesicles have similar densities in AZs innervating FSIN and O-LM cell dendrites (p = 0.16, MWU test, n = 68 FSIN and 63 O-LM cell targeting synapses in 4 mice). Densities were calculated from 200-nm-thick sections. Filled circles represent means within individual cells. Horizontal lines in the boxplots: 25th, 50th, and 75th percentiles, rectangle: mean, whiskers: SD.
- (D) Spatial distribution of vesicles within 100 nm of the AZ membrane. Inset shows the spatial distribution within the first 30 nm (n = 20 FSIN and 30 O-LM cell targeting synapses in 3 mice). Data are shown as mean \pm SD.
- (E) Number (mean \pm SD) of vesicles within bins of 5 and 10 nm distance from the AZ normalized to AZ area (n = 20 FSIN and 30 O-LM cell targeting synapses in 3 mice). This figure was adopted from Aldahabi et al. (2022).

4.9. Modeling Both Synapses by a Two-Step Priming Model Highlights Their Differences

The sole evidence for differential priming states of SVs at PC – FSIN versus PC – O-LM IN synapses comes from the differential effects of PDBU on these two connection types.

Therefore, based on the recently published sequential two-step priming model, which proposes two sequential docking/priming states prior to exocytosis, we hypothesized that a difference in the proportion of SVs in TS could underlies the observed differences in Pv between these two connections (Section 2.1.4.). To test this hypothesis, we performed paired whole-cell recordings and applied a series of simple and complex presynaptic stimulation protocols, followed by mathematical modeling of the resulting EPSCs using the sequential two-step priming model.

4.9.1. Short-Term Plasticity Characterization at PC – FSIN Connections

To investigate the dynamic release properties at PC – FSIN connections, we used various stimulation protocols to assess STP, recovery from facilitation/depression, and the effect of low-frequency conditioning on subsequent high-frequency trains. For frequencydependent release, trains of presynaptic stimulation were delivered at 5, 20, and 100 Hz, and the resulting postsynaptic responses were recorded (Figure 19 A-C). Interestingly, PPR_{2/1} was frequency-independent (PPR_{2/1} at 5 Hz: 0.70 ± 0.18 , at 20 Hz: 0.74 ± 0.3 , and at 100 Hz: 0.74 ± 0.35). However, the amplitudes of eEPSCs at steady state toward the end of the stimulus trains exhibited frequency-dependent depression (Figure 19D; normalized eEPSC amplitude from grand total averaged trace (GTA) at 5 Hz: 0.48, at 20 Hz: 0.37, and at 100 Hz: 0.14). Recovery at 110 ms after long high-frequency stimulation (15 APs at 100 Hz) was also examined, revealing that the first eEPSC amplitude of the recovery train was $56 \pm 23\%$ of the first EPSC of the initial train (Figure 19E). Following a shorter stimulation train (6 APs at 100 Hz), the recovery was very similar (0.58 \pm 0.23 of the first EPSC of the initial train; n = 13; Figure 19F). Increasing the recovery time to 1.5 seconds after the short train (6 APs at 100 Hz) showed recovery of the first EPSC to 0.73 ± 0.21 of its original value (n = 13; Figure 19F). Finally, a complex stimulation protocol was applied, consisting of a 6 APs at 20 Hz preconditioning train, followed by a 15 APs at 100 Hz train, and then a recovery train (6 APs at 100 Hz) after 110 ms and 1.5-

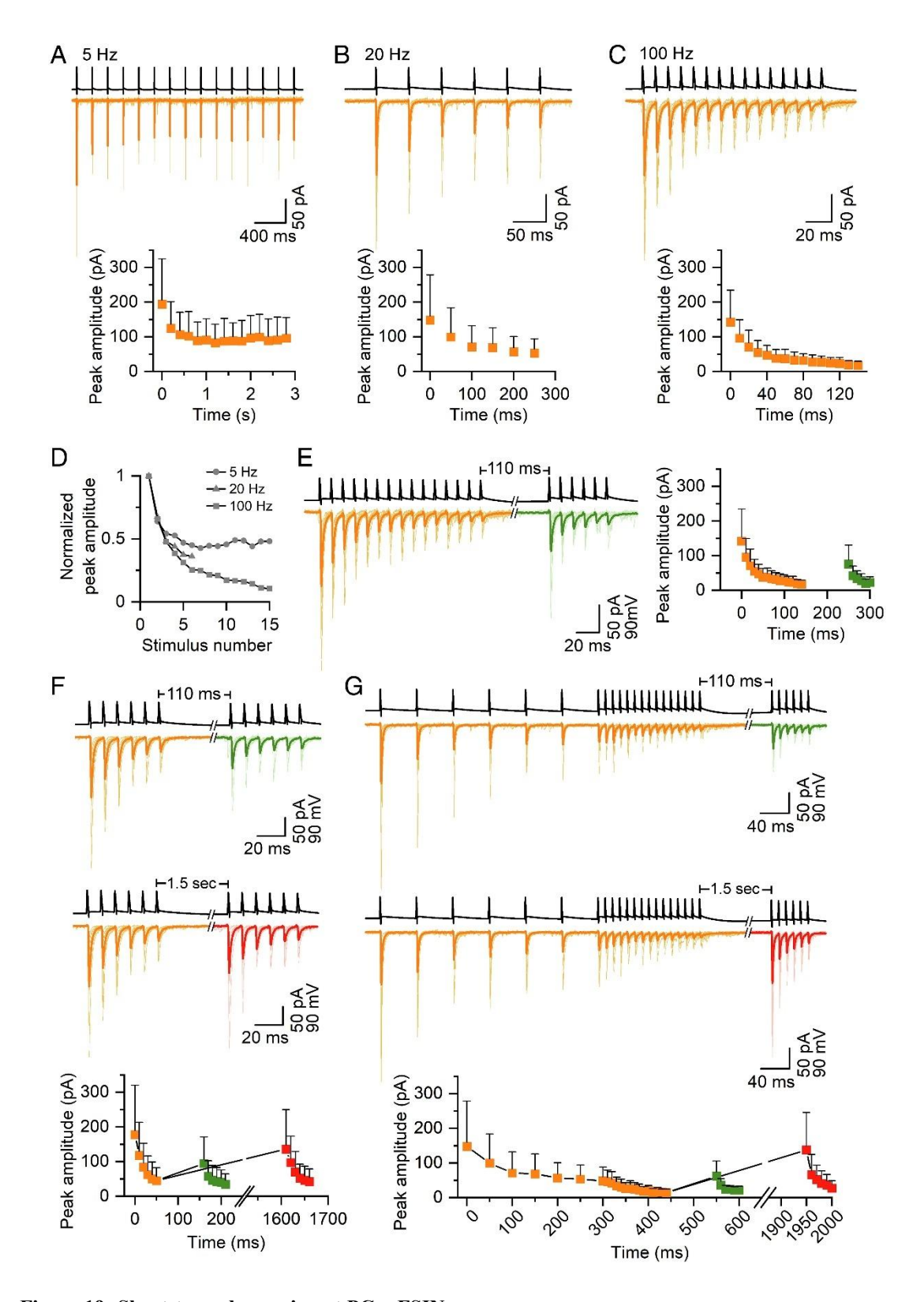


Figure 19: Short-term depression at PC – FSIN synapses.

(A) Top panel. A train of 15 action potentials (APs) at 5 Hz in hippocampal CA1 PCs (black trace) evokes EPSCs (orange traces) in FSINs. Averaged EPSC traces are shown from individual pairs (light orange) and superimposed is the grand total average trace (GTA) of 12 recorded pairs (dark orange). Bottom

panel. Evoked EPSC mean peak amplitudes are plotted as a function of time.

- **(B)** Same as (A) but 6 APs at 20 Hz (n = 20 for generating the GTA).
- (C) Same as (A) but 15 APs at 100 Hz (n = 21 for generating the GTA).
- **(D)** Normalized eEPSCs peak amplitudes from the GTA traces at 5, 20, and 100 Hz showing frequency dependence of steady-state depression.
- (E) 15 APs at 100 Hz followed by a short recovery train (6 AP at 100 Hz) after 110 ms. Examples of averaged eEPSC traces are shown from individual pairs (light orange, light green) as well as the GTA trace (dark orange and dark green, n = 21 pairs). eEPSC mean peak amplitudes are plotted vs. time (Right).
- **(F)** Top panel. Same as (E, Left) but in this protocol a short train (6 AP at 100 Hz) is followed by a short recovery train (6 AP, at 100 Hz) after 110 ms (n = 13, Top, green) or 1.5 s (the same 13 pairs, Middle, red). Bottom panel. EPSCs mean peak amplitudes are plotted vs. time (n = 13 pairs). In each pair, protocols with the two different recovery times were applied. The first 6 EPSC amplitude values are calculated from 20 traces in each pair, whereas the recovery 6 EPSC amplitudes from 10 and 10 traces. **(G)** Complex protocols composed of a preconditioning train (6 APs at 20 Hz) followed by a high-frequency long train (15 APs at 100 Hz) then a recovery short train after either 110 ms (6 APs at 100 Hz, n = 10, Top, green) or 1.5 s (n = 10, Middle, red). eEPSC mean peak amplitudes are plotted vs. time (Bottom). In the plot, the preconditioning and the 15 APs data were pooled together from the two protocols with different recovery times (n = 20 pairs). This figure was adopted from Aldahabi et al. (2024).

second recovery periods. The 20 Hz and 100 Hz trains induced moderate and robust depression, respectively. Recovery was dependent on the time, with recovery of 0.51 ± 0.20 of the first EPSC amplitude observed after 110 ms, which fully recovered after 1.5 seconds $(1.16 \pm 0.51; Figure 19G)$.

4.9.2. Modeling PC – FSIN Synapses with a Sequential Two-Step Priming Model

To understand the status of SVs at their release sites and their fusion at PC – FSIN synapses, we modeled our data using the sequential two-step priming model (151) (*Figure 20A*). Several model parameters were adopted from Lin et al. (2022), including a resting [Ca²⁺] of 50 nM and an increment of effective [Ca²⁺] of 110 nM following each AP. All other parameters were fitted (see Methods and Table S1 from Aldahabi et al. 2024).

The model parameters were initially fit using data from five protocols: three simple trains at 100, 20, and 5 Hz, a long train followed by a short train (15 APs + 6 APs at 100 Hz), and two short trains in sequence (6 APs + 6 APs at 100 Hz; *Figure 20B*), note the goodness of the model fit. Using the same model parameters, data from the two remaining complex protocols were predicted (*Figure 20C*). Subsequently, the reverse approach was

employed: model parameter fitting was performed using the complex protocols and the 5 Hz train (*Figure 20D*), and the results of the remaining four protocols were predicted (*Figure 20E*). Because both approaches yielded qualitatively and quantitatively comparable good fits (see the RMSD values in *Figure 20B - E*), the parameter values from each method were averaged and used for the final data simulation of all seven protocols (*Figure 20 F-G*). Our model fitting/parameter optimization at PC – FSIN synapses resulted in a P_{fusion} value of 0.6 and a TS fraction (=TS/(TS+LS)) of 0.44, resulting in a Pv of 0.26. All model parameters, along with an explanation of terms, are provided in Aldahabi et al. (2024), SI Appendix, Table S1.

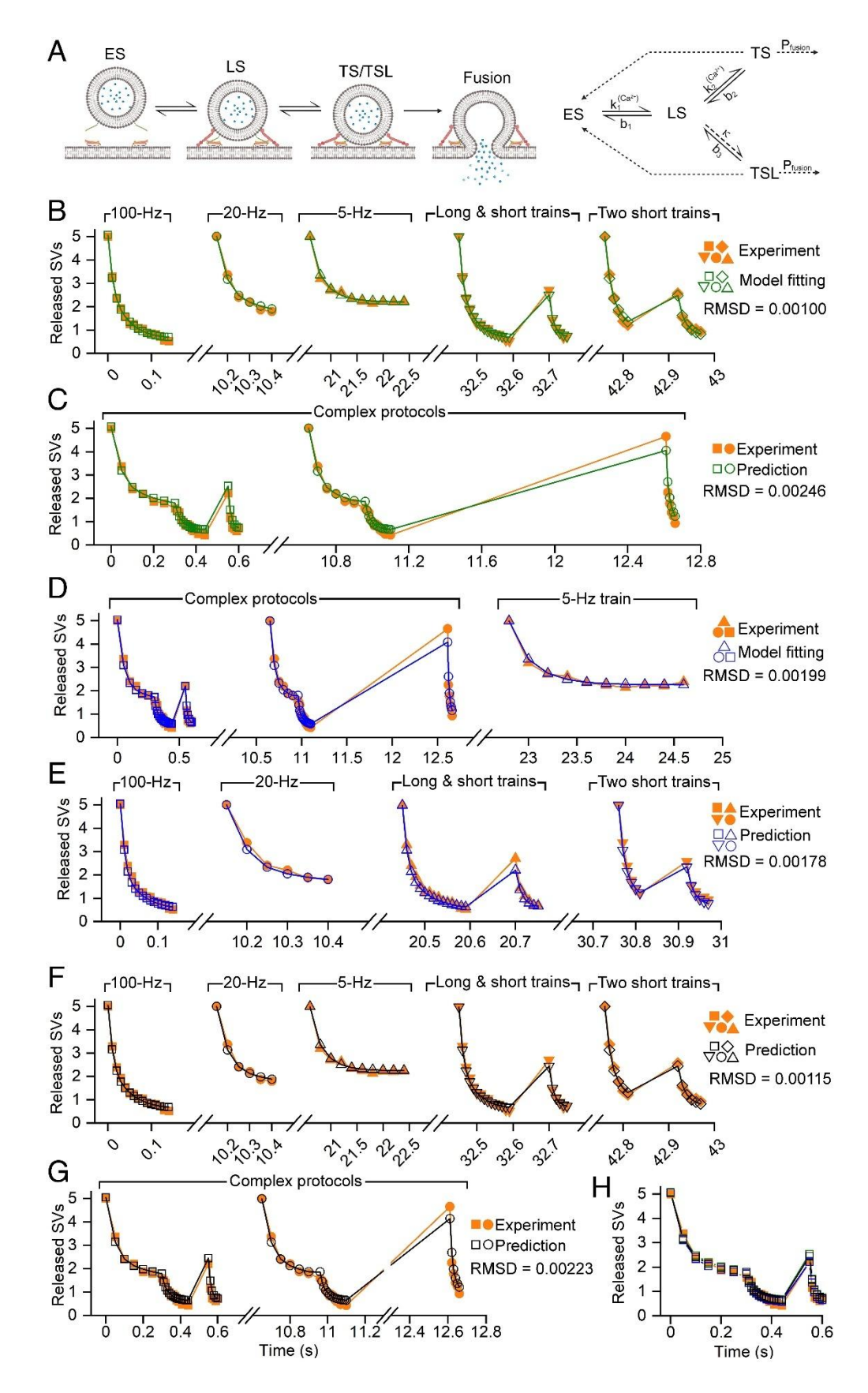
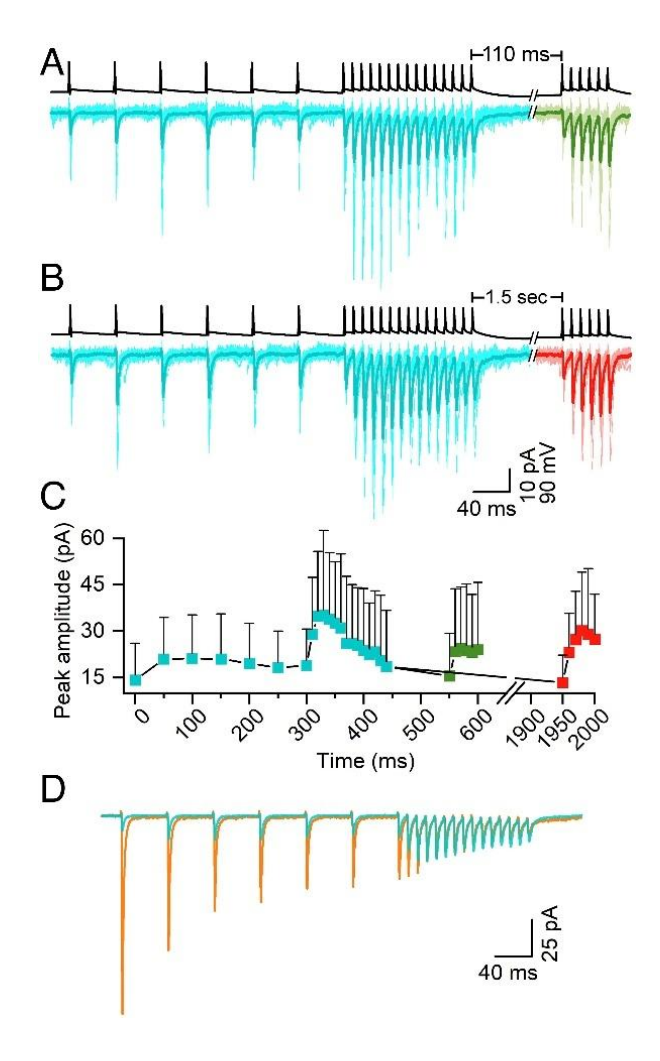


Figure 20: A sequential two-step priming model reproduces short-term depression patterns at PC – FSIN synapses.

- (A) Left: Schematic illustration of the sequential two-step priming model. Synaptic vesicles (SVs) can dock in empty docking sites (ES) and go through two sequential priming steps. In the first step, SVs are in a loosely docked state (LS) and are fusion incompetent from which they enter tightly docked states (TS or TSL) and become fusion competent. SVs from the TS and TSL states can fuse with the active zone membrane. Right: Kinetic scheme of state transitions between four states. A labile tightly docked state (TSL) needed to be introduced to describe robust facilitation at PC O-LM IN synapses. b1, k1, b2, and $k2_0$ are rate constants, whereas κ denotes the fraction of SVs that are transferred from the LS state to TSL after each action potential. The b3 is the decay time constant with which TSL returns to LS. b3 is approximately 50 times smaller than 1/b2. The model is adopted from ref. (151).
- **(B)** The sequential two-step priming and fusion model was fitted to PC FSINs data obtained from five different protocols (shown in Fig. 19 A-F). RMSD, Root-mean-square deviation.
- (C) Experimental data of two complex protocols (Fig. 19G) and model prediction using the model parameters obtained in (B).
- (D) Same as (B) but the model fitting was performed on the two complex protocols and the 5 Hz train.
- (E) Experimental data and model predictions using the model parameters obtained in (D).
- (F) Experimental data and model predictions for the five simple protocols using the mean of the model parameters obtained in (B) and (D).
- **(G)** Same as (F) but for the two complex protocols.
- (H) Experimental data of one complex protocol superimposed onto model predictions from (C), (D), and
- (G). All experimental data shown are from the GTA traces. The X-axis indicates the time in seconds. This figure was adopted from Aldahabi et al. (2024).

4.9.3. Short-Term Plasticity at PC – O-LM IN Synapses

To compare the PC – FSIN model parameters derived above with those of PC – O-LM IN synapses, we performed paired whole-cell patch-clamp recordings from PCs and O-LM INs using only the complex stimulation protocols. These protocols proved sufficient for model fitting and parameter optimization, as demonstrated previously (*Figure 20*). Consistent with prior results, the amplitude of the first eEPSC in the train was small (14.2 \pm 11.9 pA, n = 50 pairs; *Figure 21A-C*). Evoked EPSCs slightly facilitated during the 20 Hz preconditioning train, with further facilitation observed during the subsequent 100 Hz train stimulation (*Figure 21A-C*). The normalized eEPSC amplitude of the recovery train after 110 ms was 1.50 ± 1.66 (normalized to the first EPSC of the preconditioning train, n = 26), and there was a full recovery after 1.5 seconds (0.95 \pm 1.66, n = 18; *Figure 21C*). To compare the eEPSCs at FSIN and O-LM IN, the GTA traces were shown superimposed (*Figure 21D*). Notably, the >10-fold difference in the first eEPSC amplitude diminishes, and roughly the same eEPSC amplitude is evoked after the 9th AP in both synapse types.



←Figure 21: Short-term facilitation of PC – O-LM synapses.

- (A) Action potentials (APs) from hippocampal CA1 PCs (black trace) and evoked EPSCs (cyan and green) recorded in O-LM cells. Complex stimulation protocol composed of a preconditioning train (6 APs at 20 Hz), followed by a high-frequency long train (15 APs at 100 Hz), then a recovery short train after 110 ms (6 AP at 100 Hz, green). Averaged EPSCs are shown in individual pairs (light cyan or light green) with the grand total average (GTA, dark cyan and dark green, n = 30 pairs).
- **(B)** Same as (A) but with a recovery interval of 1.5 s (n = 20 pairs). The traces in the recovery period are shown in red.
- (C) eEPSC mean peak amplitudes are plotted vs. time; colors correspond to those of traces in (B) and (C). Data for the preconditioning and for the 15 AP-traces were pooled together from the two protocols (110 ms and 1.5 s recovery test durations, cyan points, n = 50 pairs).
- **(D)** Superimposed GTA traces from FSIN (orange) and O-LM (cyan) cells illustrate the dramatic difference in the short-term plasticity patterns. This figure was adopted from Aldahabi et al. (2024).

4.9.4. Modeling Synaptic Transmission at PC – O-LM IN Connections Suggests Very Low Occupancy of Release Sites by Well-Primed SVs

The subsequent goal was to identify the key model parameters responsible for the functional differences between PC – FSIN and PC – O-LM IN connections. We began with the PC – FSIN model and systematically varied the parameters individually to determine if we could reproduce the PC – O-LM IN data. We allowed for changes in one, then two, and then three parameters simultaneously. Varying only one or two parameters was insufficient to reproduce the PC – O-LM IN data; changing at least three parameters was necessary. When $k2_0$, s2, and P_{fusion} were simultaneously optimized, the model qualitatively captured the small initial facilitation during the low-frequency (20 Hz) train and the large facilitation and depression during the high-frequency (100 Hz) EPSC train (*Figure 22A*). The parameters $k2_0$ and s2 determine the feedforward rate constant from

LS to TS at rest and its Ca²⁺ sensitivity, respectively (*Figure 20A*). Finally, we allowed all model parameters to be fit to achieve the best possible fit to the PC – O-LM IN data, which resulted in a slight improvement in the overall fit (*Figure 22B* & check SI Appendix, Table S1 from Aldahabi et al., 2024).

We then examined the effects of changing these three model parameters. The greater than 10-fold reduction in $k2_0$ and s2 ($k2_0$: from 0.24 to 0.022 sec⁻¹ and s2: from 0.25 to 0.012; see SI Appendix, Table S1, Aldahabi et al. 2024), resulted in a substantial 6.5-fold decrease in the proportion of well-primed SVs (TS fraction = 0.07 vs. 0.44 for FSIN), while the reduction in P_{fusion} was only 40% (from 0.6 to 0.36; see SI Appendix, Table S1, Aldahabi et al. 2024). These results demonstrate that the sequential two-step priming model can accurately reproduces the experimental data from both PC – FSIN and PC – O-LM IN synapses. Moreover, these findings show that modifying only three parameters in the depressing PC – FSIN model is sufficient to convert it into a facilitating synapse (*Figure 22C*).

Our results indicate that the main difference underlying the distinct Pv of these synaptic connections lies in a robust difference in the fraction of well-primed SVs (TS fraction) rather than the fusion probability of such SVs (P_{fusion}).

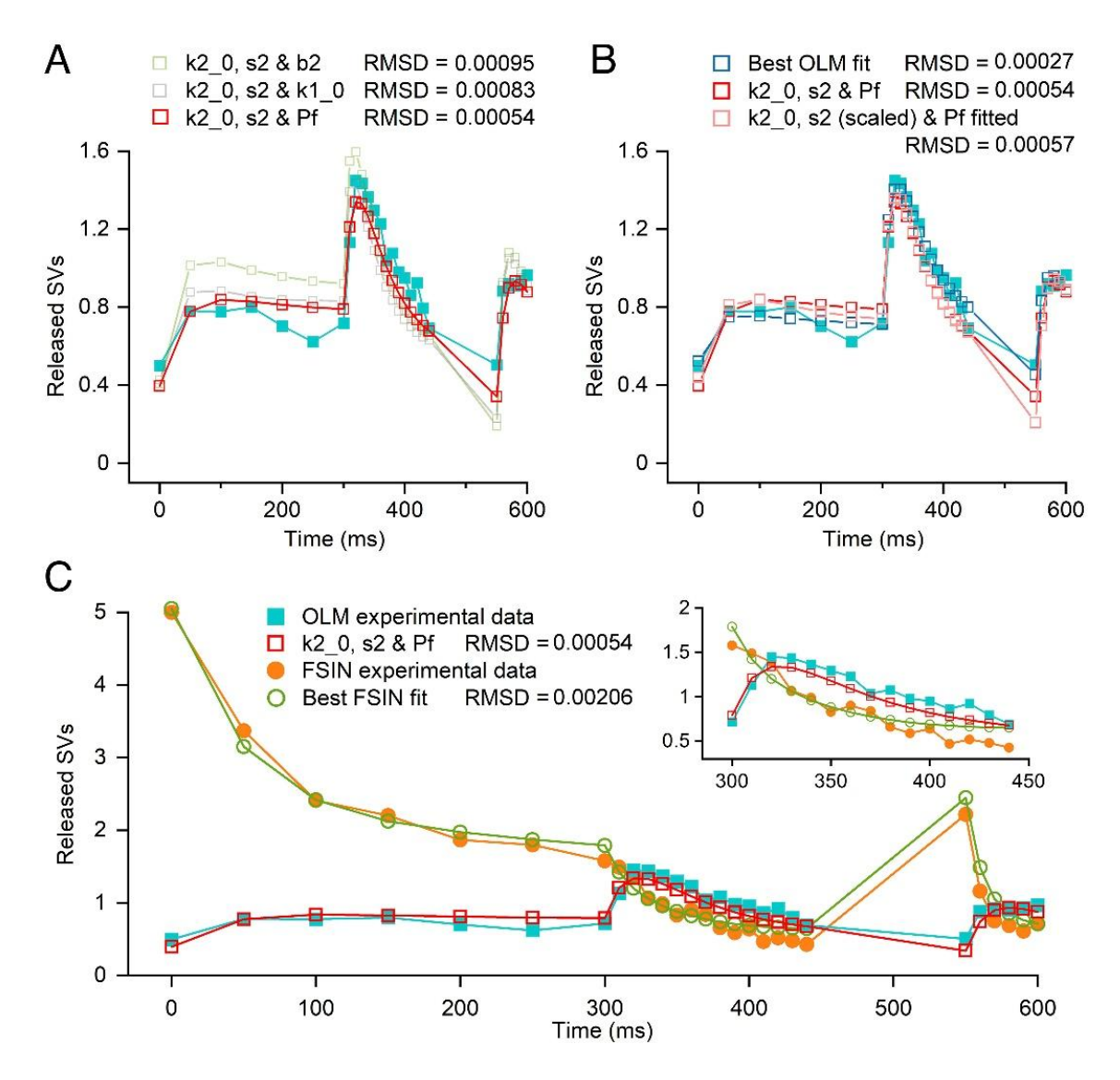


Figure 22: Changing model parameters related to the second SV priming step plus P_{fusion} are sufficient to change PC – FSIN-like release to PC – O-LM-like release dynamics.

- (A) All parameters of the two-step SV priming model were obtained from the best fit to the PC FSIN data (Figure 20 F & G), and three parameters were fitted to the PC O-LM IN experimental data. Qualitatively, all three illustrated simulations describe the STP pattern, but fitting $k2_0$, s2, and P_{fusion} (Pf) reproduces the data with the smallest error (red).
- **(B)** The best O-LM IN fit (blue), $k2_0$, s2, and P_{fusion} fit [as shown in panel (A); red] and fit in which $k2_0$ and s2 were constrained to scale together with one scaling factor (light red) are shown.
- (C) Experimental data and best model fit for PC FSIN (Figure 20G) and the $k2_0$, s2 and P_{fusion} fit for PC O-LM IN (A) are superimposed for direct comparison using the same complex protocol. The Inset shows the episode of 100 Hz stimulation at better resolution. This figure was adopted from Aldahabi et al. (2024).

5. DISCUSSION

My study demonstrates that the differential presynaptic expression of Munc13-2 at CA1 PC – mGluR1 α +/O-LM IN synapses does not significantly impact Pv at PC – O-LM connections. Synapses lacking Munc13-2 exhibited functional properties comparable to control synapses containing Munc13-2. Therefore, Munc13-2 does not appear to be a primary factor contributing to the lower Pv observed at these synapses compared to PC-FSIN synapses.

Next, using high-resolution immunolocalization of Munc13-1 and Cav2.1 revealed similar distances between VGCCs and RSs at PC – FSIN and PC – O-LM IN synapses, suggesting that the large difference in Pv is unlikely to be due to a large difference in P_{fusion} . This is supported by the less than 2-fold difference in the effect of the K^+ channel blocker 4-AP on eEPSCs recorded from these two IN types. However, application of the phorbol ester analog PDBU resulted in an ~80% increase in eEPSC amplitude at PC – FSIN connections, contrasted by an ~4.5-fold increase in postsynaptic responses at PC – O-LM IN connections, suggesting incomplete SV docking/priming at AZs innervating O-LM cells. High-resolution EM analysis demonstrated similar docked SV densities at these two synapse populations, suggesting that SV priming might differ despite similar morphological docking.

To investigate the impact of different priming states and fusion on these two synapses, a combined experimental and modeling approach was used. A recent sequential two-step priming model (151) was employed to simulate experimental data from paired recordings between CA1 PC and FSINs or O-LM cells using several presynaptic activity protocols. This model accurately described all data obtained from both IN types. Our results indicate that the main difference underlying the distinct Pv of these synaptic connections lies in a robust difference in the fraction of well-primed SVs (TS fraction) rather than the fusion probability of such SVs (P_{fusion}).

5.1. Distinct Localization of Presynaptic Munc13-2 and mGluR7 in an Elfn1 Postsynaptic-Dependent Manner

The subcellular distribution of presynaptic proteins crucial for SV docking/priming was examined to determine if any exhibited postsynaptic cell type-dependent distribution in

PC axons. Munc13-2 displayed punctate labeling in the str. oriens of the dorsal hippocampal CA1 area, and colocalization experiments revealed selective enrichment in the AZs of local CA1 PC boutons innervating mGluR1α+ INs. This represents the third instance, following mGluR7 (187) and mGluR8 (217), where such specific presynaptic molecules localized in postsynaptic target cell type-specific manner in the cortical networks, suggesting this phenomenon may be more prevalent than previously thought.

Munc13s are essential SV priming factors, indispensable for SV fusion (107, 111, 218). They form a tripartite complex with RIMs and RIM-binding proteins, collaborating to recruit VGCCs and SVs to the AZ (126, 219–224). Of the three isoforms expressed in the CNS (Munc13-1 to Munc13-3), Munc13-1 has the broadest distribution, while Munc13-2 and 3 exhibit more restricted and largely non-overlapping expression patterns (225). Several studies have investigated Munc13 function in heterologous expression systems or neuronal cultures (124, 140, 226). For instance, Rosenmund et al. (2002) showed that, in cultured hippocampal neurons, Munc13-1 likely contributes to tight vesicle docking and confers high Pv, whereas SVs in Munc13-2-containing AZs are loosely docked and exhibit low Pv. However, surprisingly, conditional removal of Munc13-2 from CA1 PCs (within an intact neuronal network) had no apparent effect on the Pv of CA1 PC to mGluR1α+ IN synapses. Similar results were observed at mouse photoreceptor ribbon synapses, where Munc13-2 is the sole Munc13 isoform present (193), although these synapses differ from conventional synapses in many respects. A similar lack of effect was also found at Schaffer collateral inputs onto CA1 PCs (127) and in the calyx of Held (227) in Munc13-2 KO animals. It should be noted, however, that the amount of bMunc13-2 is low in Schaffer collateral to CA1 PC synapses in control animals; therefore, the lack of effect in the KO is not entirely surprising. Furthermore, in the same Munc13-2 KO animals, an apparent reduction of Pv was found at hippocampal mossy fiber synapses onto CA3 PCs (127). Munc13-2 knockdown with shRNA from glutamatergic input onto amygdala PCs increases Pv (228), indicating a complex role of Munc13-2 in SV priming, likely dependent on its interacting partners within the AZ protein complex.

While shRNA-mediated Elfn1 knockdown did not induce STD of EPSCs on SST+ INs, it did reduce paired-pulse facilitation, suggesting an alteration in synaptic Pv (56), which was subsequently linked to the absence of presynaptic mGluR7 (189, 190). Our results demonstrate that Munc13-2 enrichment at CA1 PC to mGluR1 α + IN synapses is Elfn1-

dependent. Elfn1 removal results in the loss of both mGluR7 and Munc13-2, a threefold increase in peak eEPSC amplitude at PC to mGluR1α+/O-LM IN synapses, and decreased STF. To differentiate whether this functional effect is caused by the absence of constitutive mGluR7 activity or the absence of Munc13-2, we conditionally removed Munc13-2 (both bMunc13-2 and ubMunc13-2 isoforms) from these synapses. This was accomplished by injecting Cre-recombinase-expressing AAVs into the dorsal hippocampal CA1 of transgenic mice with Munc13-2 exons 15-17 flanked by loxP sites. Because Munc13-2 removal did not affect eEPSC amplitudes or PPRs, we conclude that the functional effects of Elfn1 removal from SST/mGluR1a+ INs are solely a consequence of mGluR7 loss. This is consistent with results from pharmacological blockade of group III mGluRs, which produces a similar effect on EPSC amplitudes (188). In summary, despite the high concentration of Munc13-2 at hippocampal CA1 PC to mGluR1α+/O-LM IN synapses, it does not appear to play a role in establishing the unusually low Pv observed at these connections. This suggests that Munc13-1 may be capable of "differential priming" of SVs, or that other, as-yet-unidentified molecules may prevent the release of tightly docked vesicles.

5.2. [Ca²⁺] Influx Is Not the Primary Determinant of Pv

Our data indicate that most RSs are occupied by docked SVs, suggesting a high P_{occ} , consistent with Sakamoto et al. (2018), who reported nearly identical numbers of RSs and readily releasable SVs in cultured hippocampal neurons (215). Our findings also align with observations from crayfish neuromuscular junctions, where low-Pv tonic synapses exhibit even higher docked vesicle density than high-output phasic synapses, demonstrating that Pv cannot be predicted solely from the number of docked vesicles (229). Furthermore, our results are consistent with Millar et al. (2005), who showed that artificially imposing similar intra-bouton [Ca²⁺] levels at tonic and phasic neuromuscular junctions does not normalize release; the output of low-Pv tonic synapses remains lower despite a greater number of docked vesicles (230), suggesting that most SVs at tonic synapses are molecularly incompetent for release.

Since the discovery of the Ca²⁺-dependence of neurotransmitter release (79), one of the most obvious explanations of different presynaptic strengths is the distinct amount of Ca²⁺ entry into the presynaptic terminals upon an AP. EM immunolocalization studies have

established that presynaptic VGCCs are exclusively located in AZs at central synapses (195, 231–234), where their numbers vary considerably, suggesting that VGCC number could be a key determinant of Pv. This idea was supported by $Ca_V2.1$ VGCC subunit overexpression in the Calyx of Held, which increased Pv (235), and by the results showing a correlation between VGCC number, Ca^{2+} influx, and Pv at individual RSs at the Drosophila NMJ (236–238). However, a recent study challenged this simple view. Cerebellar parallel fiber to Purkinje cell synapses have high VGCC density and large APevoked $[Ca^{2+}]$ transients, yet exhibit low Pv, while cerebellar MLIN synapses have higher Pv despite 5-fold fewer VGCCs and smaller AP-evoked Ca^{2+} transients (196).

The similar coupling distances between RSs and VGCCs at PC – FSIN and PC – O-LM IN synapses, the moderate difference in AP-evoked peak [Ca²⁺] transients, and the effect of 4-AP all suggest a small difference in P_{fusion} at these synapses, which is clearly insufficient to explain the 10-fold difference in Pv.

5.3. The Priming State of SVs Has a Greater Impact on Pv

It is reasonable to hypothesize that the energy barrier for vesicle fusion for a given [Ca²⁺] increase differs between these synapses, implying distinct molecular mechanisms of vesicle tethering, docking, or priming. Because our high-resolution EM experiments revealed similar docked vesicle densities at both synapse types, we can exclude dramatically different tethering and docking as a major contributing factor, leaving molecular priming as the most probable explanation (205, 239). It is now widely accepted that Munc13 molecules are the master regulators of SV priming at central synapses [reviewed in (240). Our results, which show a dramatic difference in the effect of PDBU on eEPSCs at PC – FSIN vs. PC – O-LM IN synapses, suggest that Munc13 molecules are the key determinants of the functional differences between these synapses. This could be achieved through a differential regulation of Munc13-1.

5.4. Munc13-1 as a Prominent Molecule Regulating Pv

Having excluded distinct Munc13 isoforms as the primary cause of the observed functional differences, we must consider postsynaptic target cell-type-dependent differential regulation of Munc13-1. RIM is a candidate for differential Munc13-1 regulation, as Munc13-1 homodimerization via its C2A domain is inhibited by RIM

binding (131, 133). However, RIM1/2 density at PC synapses targeting mGluR1 α + INs was even higher than in surrounding synapses (*Figure 8G*), indicating that low *Pv* cannot be attributed to unrelieved Munc13 autoinhibition by RIM at PC – O-LM IN low Pv synapses.

Munc13-1 activity is modulated by various second messengers, including Ca²⁺, DAG, PIP, or calmodulin. For instance, DAG or its analog PDBU binding to the C₁ domain enhances Munc13-1 activity (137, 138). Indeed, a single point mutation in this domain, rendering Munc13-1 constitutively active and phorbol ester-insensitive, results in increased SV release (140). Similarly, Ca²⁺ binding to the C₂B domain increases Munc13-1's affinity for PIP and PIP2, thereby increasing its priming activity (141). Although Ca²⁺ binding enhances Munc13-1 binding to PIP- and PIP2-enriched membranes, the concentration of these molecules in the presynaptic plasma membrane is also crucial; a 2-fold decrease in PIP or PIP2 concentration abolishes Ca²⁺-induced phospholipid binding of the C₂B domain (141). These findings collectively suggest that differential concentrations of DAG and PIP/PIP2 in presynaptic plasma membranes, or variations in resting [Ca²⁺] levels (241), might underlie the postsynaptic target cell-type-dependent differences in Munc13-1 priming efficacy.

5.5. Three Model Parameters Sufficient to Transform PC – FSIN into PC – O-LM IN Model

To transform the sequential two-step priming model from PC – FSIN transmission to PC – O-LM -type synapses, only three parameters required modification: P_{fusion} , $k2_0$, and s2. While P_{fusion} only needed a moderate decrease (40%), the parameters associated with the second priming step (its resting rate constant, $k2_0$, and its Ca²⁺ dependence, s2) needed to be decreased by more than 10-fold, resulting in a greater than six-fold reduction in TS fraction. All other model parameters could retain identical values for both synapse types. Furthermore, when $k2_0$ and s2 were fit simultaneously with a joint scaling factor (*Figure 22B*), the RMSD value was only slightly larger than that obtained by fitting them separately (0.00057 vs. 0.00054). Thus, changing only two parameters (P_{fusion} and the scaling factor) was also sufficient to convert the model from PC – FSIN synapses into an adequate model for PC – O-LM IN synapses.

5.6. Modeling Captures Slightly Lower P_{fusion} at PC – O-LM IN Connections

 P_{fusion} is regulated by the number/density, conductance, and open probability of VGCCs in the AZ. Additionally, P_{fusion} depends on the Ca²⁺ sensitivity of Ca²⁺ sensors on SVs and the distance between VGCCs and these sensors (160, 196, 242). Our modeling predicted a less than twofold difference in P_{fusion} between PC – FSIN (0.6) and PC – O-LM IN (0.36) synapses. This difference in P_{fusion} may be explained by the 40% larger AP-evoked [Ca²⁺] transients measured at PC – FSIN boutons (*Figure 15L*). Indeed, 5 µM 4-AP, which increased Ca^{2+} influx by ~40% at PC - O-LM IN connections, resulted in a twofold increase in EPSC amplitude and P_{fusion} (Figure 17E, and see Figure 5 in Aldahabi et al. (2024)). What could account for the 40% larger presynaptic [Ca²⁺] influx at PC – FSIN connections? EM freeze-fracture replica immunolabeling revealed a 20% greater density of Ca_V2.1 in AZs innervating PV-positive dendrites (Figure 14F). The remaining ~20% difference may arise from a smaller conductance or lower open probability of VGCCs at PC – O-LM IN synapses, possibly through an mGluR-mediated mechanism (243). The coupling distance between VGCCs and Ca²⁺ sensors is not significantly different between these two connection types. The Ca²⁺ sensor for fusion is very likely synaptotagmin-1 at both synapses, suggesting similar Ca²⁺ sensitivity of fusion. Taken together, these data support the presence of a $\sim 20\%$ greater Ca_V2.1 VGCC density and a 40% larger [Ca²⁺] transient in PC boutons innervating FSINs, which could fully explain the less than twofold difference in P_{fusion} between these synapses.

5.7. Modeling Shows Larger Proportion of Well-Primed SVs at PC – FSIN Compared to PC – O-LM IN Connections

In contrast to the modest difference in P_{fusion} , our modeling reveals a substantial difference between PC – FSIN and PC – O-LM IN synapses in the fraction of SVs in a well-primed state at rest (0.07 vs. 0.44). The concept of a small fraction of docked, well-primed SVs explaining low Pv was proposed previously and supported by experimental evidence (200, 202, 244). Furthermore, it has been suggested that dynamic changes in the fraction of well-primed SVs during repetitive presynaptic activity could underlie STP (144, 151, 203–208). A recent study by Lin et al. (2022) demonstrated that differences in resting TS fraction underlie Pv heterogeneity among individual calyx of Held synapses (151). They also showed that P_{fusion} diversity is not required to explain STP heterogeneity at this

synapse. The fact that the proportion of well-primed SVs exhibits large synapse-to-synapse heterogeneity suggests that it may be a consequence of specific modulation at a given synapse by long-term plastic mechanisms. Indeed, it has been shown that presynaptic long-term potentiation (LTP) induction increases the fraction of well-primed SVs at neocortical L5 PC synapses (245). Similarly, at cerebellar parallel fiber to Purkinje cell synapses, LTP is associated with an increase in the readily releasable pool of SVs (246).

5.8. STF at PC – O-LM IN Synapses

Our modeling also provides an explanation for STF at PC – O-LM IN synapses. Our model predicts that the majority of SVs at this synapse are in the LS state at rest (0.93), resulting in a low TS fraction (0.07) and, consequently, low Pv (~0.025). During highfrequency repetitive stimulation, SVs transition from the LS to the TS state more rapidly due to the Ca^{2+} sensitivity (s2) of the forward rate constant k2, leading to STF at frequencies above 10 Hz. However, this mechanism alone is insufficient to explain the full extent of STF at high frequencies. Consistent with Lin et al. (2022), we propose that approximately 20% of SVs in the LS state transition to a labile TS state (TSL) following each AP, from which release can occur with a probability of P_{fusion} . Unlike the TS state, this TSL state is labile, returning to the LS state within ~40 ms (b3; Figure 20A), which is >25 times faster than the backward rate constant from the TS state (b2). Therefore, TSL does not contribute to STF at low stimulus frequencies (when the interstimulus interval is >40 ms) but plays a significant role in STF at high (e.g., at gamma frequency) stimulation. This proposed model explanation could be biologically mediated by synaptotagmin-7, which is known to transiently facilitate SV priming following repetitive stimulation, lasting for ~100 ms (247-249). Intriguingly, our model, without incorporating a Ca^{2+} -dependent increase in P_{fusion} , can fully explain one of the most robust known STF phenomena in cortical networks.

5.9. What Are the Structural Correlates of SVs in LS and TS?

We interpret the two states of our model in terms of tight and loose docking in view of recent cryo-EM studies. These studies suggest that SVs closer than 5 nm to the plasma membrane might constitute well-primed SVs, corresponding to the TS state in our model, while those 5 to 10 nm from the AZ membrane could form the LS pool (149). Compared

to cryo-EM, chemical fixation of brain tissue results in shorter SV-AZ membrane distances probably as a consequence of membrane perturbation from heavy metal staining and dehydration. Therefore, it is possible that, following chemical fixation, SVs in direct contact with the AZ membrane correspond to SVs in the TS state, and those with a short distance from the AZ (1 to 5 nm) correspond to SVs in the LS state (108, 144, 149, 184). These EM studies, along with our current modelling, suggest a large difference in the number of SVs in direct contact with the AZ plasma membrane between PC - FSIN and PC – O-LM IN synapses. However, we found with EM tomography similar docked SV densities at FSIN- and O-LM cell-targeting PC AZs (~135 SV/µm²; Figure 18). Therefore, it remains an open question whether the model's postulated functional states reflect these two morphologically defined states or represent other differences in the release machinery's state. Intriguingly, Munc13-1, a priming protein with Ca²⁺- and DAGdependent regulatory sites, has been proposed to exist in two conformations with different orientations relative to the plasma membrane (250). Our results might suggest that physical docking does not necessarily equate to molecular maturation/priming of SVs. Future experiments combining well-designed genetic modifications and EM techniques will be necessary to resolve these discrepancies.

6. CONCLUSIONS

This study aimed to determine the mechanisms underlying postsynaptic target cell typedependent Pv and STP at PC – FSIN versus PC – O-LM IN connections.

We determined that CA1 PC – FSIN connections exhibit STD and a Pv more than ten times greater than PC – mGluR1 α -expressing O-LM IN connections, which display STF. We investigated several potential mechanisms underlying this Pv difference and found:

- Presynaptic Munc13-2 localization at low-Pv PC O-LM IN synapses does not significantly influence Pv, as conditional knockout of Munc13-2 gene resulted in eEPSCs peak amplitudes and STP patterns comparable to wild-type controls.
- The distribution of Cav2.1 subunits around RSs was similar in both FSIN and O-LM-targeting AZs, with only a slightly higher (16% larger) overall density in AZs targeting FSIN dendrites.
- Presynaptic AP-evoked [Ca²⁺] influx was approximately 40% greater at PC –
 FSIN connections compared to PC O-LM IN connections.
- This difference in [Ca²⁺] influx does not primarily determine synaptic strength differences, as matching [Ca²⁺] influx with 4-AP only resulted in a 2.7-fold increase in eEPSCs at PC O-LM IN connections.
- PDBU application resulted in a ~4.5-fold augmentation at PC O-LM IN synapses, compared to only 1.7-fold at PC – FSIN synapses, indicating distinct priming states.
- Modelling synaptic transmission at both connections suggest that the primary difference in Pv is due to a very low occupancy of release sites by well-primed SVs at PC O-LM IN synapses, rather than a difference in the fusion probability (P_{fusion}) of these SVs.

7. SUMMARY

The variability in neurotransmitter release from a single presynaptic neuron, depending on its postsynaptic target, is a hallmark of cortical network complexity. We found that CA1 PC - FSIN connections exhibit 10 times larger Pv than the PC - mGluR1αexpressing O-LM IN connections. The differential distribution of proteins at presynaptic AZs is crucial for establishing these distinct Pv and STP patterns. O-LM INs express Elfn1, which trans-synaptically recruits mGluR7 to PC axon AZs. We further demonstrate that Elfn1 also selectively recruits Munc13-2, a protein involved in SV priming and docking, to PC AZs targeting mGluR1α+ INs. To determine the roles of Elfn1 and Munc13-2 at the low-Pv PC - O-LM IN connections, we performed knockout experiments. In Elfn1 KO, eEPSCs in O-LM INs showed a 3-fold increase in amplitude and reduced STF, potentially due to the loss of mGluR7, Munc13-2, or both. Conditional genetic deletion of Munc13-2 gene from CA1 PCs resulted in Munc13-2 loss from AZs, but did not affect mGluR7 levels, eEPSC amplitude, or the characteristic STF at PC – O-LM IN connections. These results indicate that Munc13-2 is not essential for the low Pv at PC – O-LM IN synapses and that Munc13-1 alone can mediate both low and high Pv at PC – O-LM and PC – FSIN synapses, respectively.

Freeze-fracture immunolabeling revealed that differences in Ca^{2+} channel and RS nanotopology or coupling distance do not explain the distinct Pv. Although $[Ca^{2+}]$ transients are 40% larger in FSIN-innervating boutons, matching $[Ca^{2+}]$ entry in both bouton populations still resulted in 7-fold smaller eEPSCs in O-LM cells, suggesting that P_{fusion} is not the primary factor limiting Pv. However, PDBU application resulted in a \sim 2.5-fold larger augmentation at PC - O-LM IN synapses compared to PC - FSIN synapses, indicating incomplete vesicle docking or priming. Similar docked vesicle densities ruled out distinct RS occupancies, demonstrating that incompletely primed, yet docked, vesicles limit PC - O-LM IN synapse output.

We used a modelling approach to determine whether the primary difference lies in AP-evoked fusion or upstream vesicle priming processes. We fit a sequential two-step SV priming model to eEPSC peak amplitudes recorded in response to complex presynaptic stimulation. At PC – FSIN connections, P_{fusion} was 0.6, and 44% of docked SVs were fusion-competent. At PC – O-LM IN synapses, P_{fusion} was only 40% lower (0.36), while

the fraction of well-primed SVs was 6.5-fold smaller. These results demonstrate that the low transmission fidelity at PC – O-LM IN synapses can be explained by a low occupancy of release sites by well-primed SVs.

8. REFERENCES

- 1. P. Andersen, R. Morris, D. Amaral, T. Bliss, J. O'Keefe, *The Hippocampus Book* (Oxford University Press, 2006; https://academic.oup.com/book/25965).
- 2. J. O'Keefe, Place units in the hippocampus of the freely moving rat. *Exp Neurol* (1976) **51**, 78–109.
- 3. R. Q. Quiroga, L. Reddy, G. Kreiman, C. Koch, I. Fried, Invariant visual representation by single neurons in the human brain. *Nature* (2005) **435**, 1102–1107.
- 4. E. Gunseli, M. Aly, Preparation for upcoming attentional states in the hippocampus and medial prefrontal cortex. *Elife* (2020) **9**.
- 5. N. L. M. Cappaert, N. M. Van Strien, M. P. Witter, "Chapter 20 Hippocampal Formation" in *The Rat Nervous System*, George Paxinos, Ed. (Elsevier, 2015; https://linkinghub.elsevier.com/retrieve/pii/B9780123742452000206), pp. 511–573.
- 6. R. L. Spencer, S. T. Bland, "Hippocampal Neurons" in *Encyclopedia of Stress*, George Fink, Ed. (Elsevier, Second., 2007; https://linkinghub.elsevier.com/retrieve/pii/B978012373947600194X)vol. 51, pp. 311–320.
- 7. T. F. Freund, G. Buzsáki, Interneurons of the hippocampus. *Hippocampus* (1996) **6**, 347–470.
- 8. T. Klausberger, P. Somogyi, Neuronal diversity and temporal dynamics: the unity of hippocampal circuit operations. *Science* (2008) **321**, 53–7.
- 9. R. A. Piskorowski, V. Chevaleyre, "Interneurons in Synaptic Plasticity and Information Storage" in *Learning and Memory: A Comprehensive Reference*, John H. Byrne, Ed. (Elsevier, Second Edition., 2017; https://linkinghub.elsevier.com/retrieve/pii/B978012809324521105X), pp. 179–198.
- 10. R. Lorente De Nó, Studies on the structure of the cerebral cortex. II. Continuation of the study of the ammonic system. *Journal für Psychologie und Neurologie* (1934) **46**, 113–177.
- 11. I. Soltesz, A. Losonczy, CA1 pyramidal cell diversity enabling parallel information processing in the hippocampus. *Nat Neurosci* (2018) **21**, 484–493.
- 12. K. G. Baimbridge, J. J. Miller, Immunohistochemical localization of calciumbinding protein in the cerebellum, hippocampal formation and olfactory bulb of the rat. *Brain Res* (1982) **245**, 223–229.

- 13. S. H. Lee, I. Marchionni, M. Bezaire, C. Varga, N. Danielson, M. Lovett-Barron, A. Losonczy, I. Soltesz, Parvalbumin-positive basket cells differentiate among hippocampal pyramidal cells. *Neuron* (2014) **82**, 1129–1144.
- M. S. Cembrowski, J. L. Bachman, L. Wang, K. Sugino, B. C. Shields, N. Spruston, Spatial Gene-Expression Gradients Underlie Prominent Heterogeneity of CA1 Pyramidal Neurons. *Neuron* (2016) 89, 351–368.
- 15. B. A. Strange, M. P. Witter, E. S. Lein, E. I. Moser, Functional organization of the hippocampal longitudinal axis. *Nat Rev Neurosci* (2014) **15**, 655–69.
- 16. K. M. Igarashi, H. T. Ito, E. I. Moser, M.-B. Moser, Functional diversity along the transverse axis of hippocampal area CA1. *FEBS Lett* (2014) **588**, 2470–6.
- 17. D. G. Amaral, C. Dolorfo, P. Alvarez-Royo, "Organization of CAl Projections to the Subiculum: A PHA-L Analysis in the Rat" (1991).
- 18. L. A. Cenquizca, L. W. Swanson, Analysis of direct hippocampal cortical field CA1 axonal projections to diencephalon in the rat. *Journal of Comparative Neurology* (2006) **497**, 101–114.
- 19. L. A. Cenquizca, L. W. Swanson, Spatial organization of direct hippocampal field CA1 axonal projections to the rest of the cerebral cortex. *Brain Res Rev* (2007) **56**, 1–26.
- 20. T. Ino, Y. Yasui, K. Itoh, S. Nomura, T. Akiguchi, M. Kameyama, N. Mizuno, Direct projections from Ammon's horn to the septum in the cat. *Exp Brain Res* (1987) **68**, 179–188.
- 21. M. Megías, Z. Emri, T. F. Freund, A. I. Gulyás, Total number and distribution of inhibitory and excitatory synapses on hippocampal CA1 pyramidal cells. *Neuroscience* (2001) **102**, 527–540.
- 22. Petilla terminology: nomenclature of features of GABAergic interneurons of the cerebral cortex. *Nat Rev Neurosci* (2008) **9**, 557–568.
- 23. D. W. Cope, G. Maccaferri, L. F. Márton, J. D. B. Roberts, P. M. Cobden, P. Somogyi, Cholecystokinin-immunopositive basket and Schaffer collateral-associated interneurones target different domains of pyramidal cells in the CA1 area of the rat hippocampus. *Neuroscience* (2002) **109**, 63–80.
- K. A. Pelkey, R. Chittajallu, M. T. Craig, L. Tricoire, J. C. Wester, C. J. McBain, Hippocampal GABAergic Inhibitory Interneurons. *Physiol Rev* (2017) 97, 1619– 1747.
- 25. M. J. Bezaire, I. Soltesz, Quantitative assessment of CA1 local circuits: Knowledge base for interneuron-pyramidal cell connectivity. *Hippocampus* (2013) **23**, 751–785.

- 26. A. Sik, M. Penttonen, A. Ylinen, G. Buzsáki, Hippocampal CA1 interneurons: an in vivo intracellular labeling study. *J Neurosci* (1995) **15**, 6651–65.
- 27. H. Pawelzik, D. I. Hughes, A. M. Thomson, Physiological and morphological diversity of immunocytochemically defined parvalbumin- and cholecystokinin-positive interneurones in CA1 of the adult rat hippocampus. *J Comp Neurol* (2002) **443**, 346–67.
- 28. C. Földy, S. H. Lee, R. J. Morgan, I. Soltesz, Regulation of fast-spiking basket cell synapses by the chloride channel ClC-2. *Nat Neurosci* (2010) **13**, 1047–1049.
- 29. S.-H. Lee, C. Földy, I. Soltesz, Distinct endocannabinoid control of GABA release at perisomatic and dendritic synapses in the hippocampus. *J Neurosci* (2010) **30**, 7993–8000.
- 30. T. Klausberger, L. F. Marton, J. O'Neill, J. H. J. Huck, Y. Dalezios, P. Fuentealba, W. Y. Suen, E. Papp, T. Kaneko, M. Watanabe, J. Csicsvari, P. Somogyi, Complementary roles of cholecystokinin- and parvalbumin-expressing GABAergic neurons in hippocampal network oscillations. *J Neurosci* (2005) **25**, 9782–93.
- 31. J. Somogyi, A. Baude, Y. Omori, H. Shimizu, S. El Mestikawy, M. Fukaya, R. Shigemoto, M. Watanabe, P. Somogyi, GABAergic basket cells expressing cholecystokinin contain vesicular glutamate transporter type 3 (VGLUT3) in their synaptic terminals in hippocampus and isocortex of the rat. *Eur J Neurosci* (2004) 19, 552–69.
- 32. L. Acsády, D. Arabadzisz, T. F. Freund, Correlated morphological and neurochemical features identify different subsets of vasoactive intestinal polypeptide-immunoreactive interneurons in rat hippocampus. *Neuroscience* (1996) **73**, 299–315.
- 33. T. Klausberger, L. F. Márton, A. Baude, J. D. B. Roberts, P. J. Magill, P. Somogyi, Spike timing of dendrite-targeting bistratified cells during hippocampal network oscillations in vivo. *Nat Neurosci* (2004) 7, 41–47.
- 34. A. Baude, C. Bleasdale, Y. Dalezios, P. Somogyi, T. Klausberger, Immunoreactivity for the GABAA receptor alpha1 subunit, somatostatin and Connexin36 distinguishes axoaxonic, basket, and bistratified interneurons of the rat hippocampus. *Cereb Cortex* (2007) 17, 2094–107.
- 35. L. Katona, D. Lapray, T. J. Viney, A. Oulhaj, Z. Borhegyi, B. R. Micklem, T. Klausberger, P. Somogyi, Sleep and Movement Differentiates Actions of Two Types of Somatostatin-Expressing GABAergic Interneuron in Rat Hippocampus. *Neuron* (2014) **82**, 872–886.

- 36. E. H. Buhl, K. Halasy, P. Somogyi, Diverse sources of hippocampal unitary inhibitory postsynaptic potentials and the number of synaptic release sites. *Nature* (1994) **368**, 823–828.
- 37. X. G. Li, P. Somogyi, J. M. Tepper, G. Buzsáki, Axonal and dendritic arborization of an intracellularly labeled chandelier cell in the CA1 region of rat hippocampus. *Exp Brain Res* (1992) **90**, 519–25.
- 38. P. Somogyi, M. G. Nunzi, A. Gorio, A. D. Smith, A new type of specific interneuron in the monkey hippocampus forming synapses exclusively with the axon initial segments of pyramidal cells. *Brain Res* (1983) **259**, 137–142.
- 39. T. J. Viney, B. Lasztoczi, L. Katona, M. G. Crump, J. J. Tukker, T. Klausberger, P. Somogyi, Network state-dependent inhibition of identified hippocampal CA3 axoaxonic cells in vivo. *Nat Neurosci* (2013) **16**, 1802–1811.
- 40. J. M. Veres, G. A. Nagy, V. K. Vereczki, T. Andrási, N. Hájos, Strategically positioned inhibitory synapses of axo-axonic cells potently control principal neuron spiking in the basolateral amygdala. *J Neurosci* (2014) **34**, 16194–206.
- 41. H. Katsumaru, T. Kosaka, C. W. Heizmann, K. Hama, Immunocytochemical study of GABAergic neurons containing the calcium-binding protein parvalbumin in the rat hippocampus. *Exp Brain Res* (1988) **72**.
- 42. T. G. Ekins, V. Mahadevan, Y. Zhang, J. A. D'Amour, G. Akguül, T. J. Petros, C. J. McBain, Emergence of non-canonical parvalbumin- containing interneurons in hippocampus of a murine model of type I lissencephaly. *Elife* (2020) **9**, 1–29.
- 43. H. Hu, J. Gan, P. Jonas, Interneurons. Fast-spiking, parvalbumin⁺ GABAergic interneurons: from cellular design to microcircuit function. *Science* (2014) **345**, 1255263.
- 44. B. Rudy, C. J. McBain, Kv3 channels: voltage-gated K+ channels designed for high-frequency repetitive firing. *Trends Neurosci* (2001) **24**, 517–526.
- 45. I. Vida, K. Halasy, C. Szinyei, P. Somogyi, E. H. Buhl, Unitary IPSPs evoked by interneurons at the stratum radiatum-stratum lacunosum-moleculare border in the CA1 area of the rat hippocampus *in vitro*. *J Physiol* (1998) **506**, 755–773.
- 46. L. Acsády, T. J. Görcs, T. F. Freund, Different populations of vasoactive intestinal polypeptide-immunoreactive interneurons are specialized to control pyramidal cells or interneurons in the hippocampus. *Neuroscience* (1996) **73**, 317–34.
- 47. S. Chamberland, C. Salesse, D. Topolnik, L. Topolnik, Synapse-specific inhibitory control of hippocampal feedback inhibitory circuit. *Front Cell Neurosci* (2010) **4**, 130.

- 48. J. C. Lacaille, A. L. Mueller, D. D. Kunkel, P. A. Schwartzkroin, Local circuit interactions between oriens/alveus interneurons and CA1 pyramidal cells in hippocampal slices: electrophysiology and morphology. *J Neurosci* (1987) 7, 1979–93.
- 49. G. Maccaferri, J. David, B. Roberts, P. Szucs, C. A. Cottingham, P. Somogyi, Cell surface domain specific postsynaptic currents evoked by identified GABAergic neurones in rat hippocampus *in vitro*. *J Physiol* (2000) **524**, 91–116.
- 50. F. Pouille, M. Scanziani, Routing of spike series by dynamic circuits in the hippocampus. *Nature* (2004) **429**, 717–723.
- 51. J. M. Blasco-Ibáñez, T. F. Freund, Synaptic input of horizontal interneurons in stratum oriens of the hippocampal CA1 subfield: structural basis of feed-back activation. *Eur J Neurosci* (1995) 7, 2170–80.
- 52. A. B. Ali, A. M. Thomson, Facilitating pyramid to horizontal oriens-alveus interneurone inputs: dual intracellular recordings in slices of rat hippocampus. *J Physiol* (1998) **507**, 185–199.
- 53. R. N. Leão, S. Mikulovic, K. E. Leão, H. Munguba, H. Gezelius, A. Enjin, K. Patra, A. Eriksson, L. M. Loew, A. B. L. Tort, K. Kullander, OLM interneurons differentially modulate CA3 and entorhinal inputs to hippocampal CA1 neurons. *Nat Neurosci* (2012) **15**, 1524–1530.
- 54. A. Baude, Z. Nusser, J. D. Roberts, E. Mulvihill, R. A. McIlhinney, P. Somogyi, The metabotropic glutamate receptor (mGluR1 alpha) is concentrated at perisynaptic membrane of neuronal subpopulations as detected by immunogold reaction. *Neuron* (1993) **11**, 771–87.
- 55. F. Ferraguti, P. Cobden, M. Pollard, D. Cope, R. Shigemoto, M. Watanabe, P. Somogyi, Immunolocalization of metabotropic glutamate receptor 1α (mGluR1α) in distinct classes of interneuron in the CA1 region of the rat hippocampus. *Hippocampus* (2004) **14**, 193–215.
- 56. E. L. Sylwestrak, A. Ghosh, Elfn1 regulates target-specific release probability at CA1-interneuron synapses. *Science* (1979) (2012) **338**, 536–540.
- 57. S. Mikulovic, C. E. Restrepo, M. M. Hilscher, K. Kullander, R. N. Leão, Novel markers for OLM interneurons in the hippocampus. *Front Cell Neurosci* (2015) **9**, 201.
- 58. D. G. Amaral, M. P. Witter, The three-dimensional organization of the hippocampal formation: A review of anatomical data. *Neuroscience* (1989) **31**, 571–591.
- 59. O. Steward, S. A. Scoville, Cells of origin of entorhinal cortical afferents to the hippocampus and fascia dentata of the rat. *J Comp Neurol* (1976) **169**, 347–70.

- 60. J. Deuchars, A. M. Thomson, CA1 pyramid-pyramid connections in rat hippocampus in vitro: Dual intracellular recordings with biocytin filling. *Neuroscience* (1996) **74**, 1009–1018.
- 61. V. T. Takács, T. Klausberger, P. Somogyi, T. F. Freund, A. I. Gulyás, Extrinsic and local glutamatergic inputs of the rat hippocampal CA1 area differentially innervate pyramidal cells and interneurons. *Hippocampus* (2012) **22**, 1379–91.
- 62. T. Deller, G. Adelmann, R. Nitsch, M. Frotscher, The alvear pathway of the rat hippocampus. *Cell Tissue Res* (1996) **286**, 293–303.
- 63. M. J. Dolleman-Van Der Weel, M. P. Witter, Projections from the nucleus reuniens thalami to the entorhinal cortex, hippocampal field CA1, and the subiculum in the rat arise from different populations of neurons. *J Comp Neurol* (1996) **364**, 637–50.
- 64. S. Kemppainen, E. Jolkkonen, A. Pitkänen, Projections from the posterior cortical nucleus of the amygdala to the hippocampal formation and parahippocampal region in rat. *Hippocampus* (2002) **12**, 735–55.
- 65. J. E. Krettek, J. L. Price, The cortical projections of the mediodorsal nucleus and adjacent thalamic nuclei in the rat. *J Comp Neurol* (1977) **171**, 157–91.
- 66. M. J. Dolleman-Van der Weel, F. H. Lopes da Silva, M. P. Witter, Nucleus reuniens thalami modulates activity in hippocampal field CA1 through excitatory and inhibitory mechanisms. *J Neurosci* (1997) **17**, 5640–50.
- 67. X. Xu, K. D. Roby, E. M. Callaway, Immunochemical characterization of inhibitory mouse cortical neurons: three chemically distinct classes of inhibitory cells. *J Comp Neurol* (2010) **518**, 389–404.
- 68. R. Tremblay, S. Lee, B. Rudy, GABAergic Interneurons in the Neocortex: From Cellular Properties to Circuits. *Neuron* (2016) **91**, 260–92.
- 69. J. Kiss, G. Buzsaki, J. S. Morrow, S. B. Glantz, C. Leranth, Entorhinal cortical innervation of parvalbumin-containing neurons (Basket and Chandelier cells) in the rat Ammon's horn. *Hippocampus* (1996) **6**, 239–46.
- 70. L. Wittner, D. A. Henze, L. Záborszky, G. Buzsáki, Hippocampal CA3 pyramidal cells selectively innervate aspiny interneurons. *Eur J Neurosci* (2006) **24**, 1286–98.
- 71. Y. Sun, A. Q. Nguyen, J. P. Nguyen, L. Le, D. Saur, J. Choi, E. M. Callaway, X. Xu, Cell-Type-Specific Circuit Connectivity of Hippocampal CA1 Revealed through Cre-Dependent Rabies Tracing. *Cell Rep* (2014) 7, 269–280.
- 72. F. Pouille, M. Scanziani, Enforcement of temporal fidelity in pyramidal cells by somatic feed-forward inhibition. *Science* (2001) **293**, 1159–63.

- 73. G. Buzsáki, Feed-forward inhibition in the hippocampal formation. *Prog Neurobiol* (1984) **22**, 131–53.
- 74. C. Adaikkan, J. Joseph, G. Foustoukos, J. Wang, D. Polygalov, R. Boehringer, S. J. Middleton, A. J. Y. Huang, L.-H. Tsai, T. J. McHugh, Silencing CA1 pyramidal cells output reveals the role of feedback inhibition in hippocampal oscillations. *Nat Commun* (2024) **15**, 2190.
- 75. A. Ylinen, I. Soltész, A. Bragin, M. Penttonen, A. Sik, G. Buzsáki, Intracellular correlates of hippocampal theta rhythm in identified pyramidal cells, granule cells, and basket cells. *Hippocampus* (1995) **5**, 78–90.
- 76. C. Varga, M. Oijala, J. Lish, G. G. Szabo, M. Bezaire, I. Marchionni, P. Golshani, I. Soltesz, Functional fission of parvalbumin interneuron classes during fast network events. *Elife* (2014) **3**, 1–23.
- 77. N. Hájos, J. Pálhalmi, E. O. Mann, B. Németh, O. Paulsen, T. F. Freund, Spike timing of distinct types of GABAergic interneuron during hippocampal gamma oscillations in vitro. *J Neurosci* (2004) **24**, 9127–37.
- 78. J. J. Tukker, P. Fuentealba, K. Hartwich, P. Somogyi, T. Klausberger, Cell type-specific tuning of hippocampal interneuron firing during gamma oscillations in vivo. *J Neurosci* (2007) **27**, 8184–9.
- 79. J. del Castillo, B. Katz, Quantal components of the end-plate potential. *J Physiol* (1954) **124**, 560–573.
- 80. G. J. Augustine, F. Santamaria, K. Tanaka, Local Calcium Signaling in Neurons. *Neuron* (2003) **40**, 331–346.
- 81. B. L. Sabatini, W. G. Regehr, Timing of neurotransmission at fast synapses in the mammalian brain. *Nature* (1996) **384**, 170–2.
- 82. J. C. López, Quantifying synaptic efficacy. *Nat Rev Neurosci* (2002) **3**, 332–332.
- 83. L. E. Dobrunz, C. F. Stevens, Heterogeneity of release probability, facilitation, and depletion at central synapses. *Neuron* (1997) **18**, 995–1008.
- 84. H. L. Atwood, S. Karunanithi, Diversification of synaptic strength: presynaptic elements. *Nat Rev Neurosci* (2002) **3**, 497–516.
- 85. N. A. Hessler, A. M. Shirke, R. Malinow, The probability of transmitter release at a mammalian central synapse. *Nature* (1993) **366**, 569–572.
- 86. W. G. Regehr, Short-term presynaptic plasticity. *Cold Spring Harb Perspect Biol* (2012) **4**, a005702.

- 87. P. S. Katz, M. D. Kirk, C. K. Govind, Facilitation and depression at different branches of the same motor axon: evidence for presynaptic differences in release. *J Neurosci* (1993) **13**, 3075–89.
- 88. A. B. Ali, J. Deuchars, H. Pawelzik, A. M. Thomson, CA1 pyramidal to basket and bistratified cell EPSPs: dual intracellular recordings in rat hippocampal slices. *J Physiol* (1998) **507**, 201–217.
- 89. A. Reyes, R. Lujan, A. Rozov, N. Burnashev, P. Somogyi, B. Sakmann, Target-cell-specific facilitation and depression in neocortical circuits. *Nat Neurosci* (1998) 1, 279–285.
- 90. H. Y. Sun, S. A. Lyons, L. E. Dobrunz, Mechanisms of target-cell specific short-term plasticity at Schaffer collateral synapses onto interneurones versus pyramidal cells in juvenile rats. *J Physiol* (2005) **568**, 815–40.
- 91. A. Rozov, N. Burnashev, B. Sakmann, E. Neher, Transmitter release modulation by intracellular Ca2+ buffers in facilitating and depressing nerve terminals of pyramidal cells in layer 2/3 of the rat neocortex indicates a target cell-specific difference in presynaptic calcium dynamics. *J Physiol* (2001) **531**, 807–26.
- 92. M. Scanziani, B. H. Gähwiler, S. Charpak, Target cell-specific modulation of transmitter release at terminals from a single axon. *Proc Natl Acad Sci USA* (1998) **95**, 12004–9.
- 93. J. Bao, K. Reim, T. Sakaba, Target-dependent feedforward inhibition mediated by short-term synaptic plasticity in the cerebellum. *J Neurosci* (2010) **30**, 8171–9.
- 94. A. Losonczy, L. Zhang, R. Shigemoto, P. Somogyi, Z. Nusser, Cell type dependence and variability in the short-term plasticity of EPSCs in identified mouse hippocampal interneurones. *J Physiol* (2002) **542**, 193–210.
- 95. H. Markram, Y. Wang, M. Tsodyks, Differential signaling via the same axon of neocortical pyramidal neurons. *Proc Natl Acad Sci U S A* (1998) **95**, 5323–8.
- 96. L. F. Abbott, W. G. Regehr, Synaptic computation. *Nature* (2004) **431**, 796–803.
- 97. H. Markram, D. Pikus, A. Gupta, M. Tsodyks, Potential for multiple mechanisms, phenomena and algorithms for synaptic plasticity at single synapses. *Neuropharmacology* (1998) **37**, 489–500.
- 98. T. C. Südhof, Neurotransmitter release: the last millisecond in the life of a synaptic vesicle. *Neuron* (2013) **80**, 675–90.
- 99. C. A. G. H. van Gelder, M. Altelaar, Neuroproteomics of the Synapse: Subcellular Quantification of Protein Networks and Signaling Dynamics. *Mol Cell Proteomics* (2021) **20**, 100087.

- 100. R. Jahn, D. Fasshauer, Molecular machines governing exocytosis of synaptic vesicles. *Nature* (2012) **490**, 201–207.
- 101. C.-W. Chang, E. Hui, J. Bai, D. Bruns, E. R. Chapman, M. B. Jackson, A structural role for the synaptobrevin 2 transmembrane domain in dense-core vesicle fusion pores. *J Neurosci* (2015) **35**, 5772–80.
- 102. Y. Lai, U. B. Choi, J. Leitz, H. J. Rhee, C. Lee, B. Altas, M. Zhao, R. A. Pfuetzner, A. L. Wang, N. Brose, J. Rhee, A. T. Brunger, Molecular Mechanisms of Synaptic Vesicle Priming by Munc13 and Munc18. *Neuron* (2017) **95**, 591-607.e10.
- 103. O. Kochubey, X. Lou, R. Schneggenburger, Regulation of transmitter release by Ca(2+) and synaptotagmin: insights from a large CNS synapse. *Trends Neurosci* (2011) **34**, 237–46.
- 104. E. R. Chapman, How does synaptotagmin trigger neurotransmitter release? *Annu Rev Biochem* (2008) 77, 615–41.
- 105. Y.-Z. Li, Y. Wang, Q. Jiao, J. Chi, Y. Liang, B. Fan, G.-Y. Li, Complexin regulation of synaptic vesicle release: mechanisms in the central nervous system and specialized retinal ribbon synapses. *Cell Commun Signal* (2024) **22**, 581.
- 106. F. J. López-Murcia, K. Reim, O. Jahn, H. Taschenberger, N. Brose, Acute Complexin Knockout Abates Spontaneous and Evoked Transmitter Release. *Cell Rep* (2019) 26, 2521-2530.e5.
- 107. F. Varoqueaux, A. Sigler, J.-S. Rhee, N. Brose, C. Enk, K. Reim, C. Rosenmund, Total arrest of spontaneous and evoked synaptic transmission but normal synaptogenesis in the absence of Munc13-mediated vesicle priming. *Proc Natl Acad Sci U S A* (2002) **99**, 9037–42.
- 108. C. Imig, S. W. Min, S. Krinner, M. Arancillo, C. Rosenmund, T. C. Südhof, J. S. Rhee, N. Brose, B. H. Cooper, The Morphological and Molecular Nature of Synaptic Vesicle Priming at Presynaptic Active Zones. *Neuron* (2014) 84, 416–431.
- 109. M. Verhage, A. S. Maia, J. J. Plomp, A. B. Brussaard, J. H. Heeroma, H. Vermeer, R. F. Toonen, R. E. Hammer, T. K. van den Berg, M. Missler, H. J. Geuze, T. C. Südhof, Synaptic assembly of the brain in the absence of neurotransmitter secretion. *Science* (2000) 287, 864–9.
- 110. L. Siksou, F. Varoqueaux, O. Pascual, A. Triller, N. Brose, S. Marty, A common molecular basis for membrane docking and functional priming of synaptic vesicles. *Eur J Neurosci* (2009) **30**, 49–56.
- 111. I. Augustin, C. Rosenmund, T. C. Südhof, N. Brose, Munc13-1 is essential for fusion competence of glutamatergic synaptic vesicles. *Nature* (1999) **400**, 457–61.

- 112. C. Ma, L. Su, A. B. Seven, Y. Xu, J. Rizo, Reconstitution of the vital functions of Munc18 and Munc13 in neurotransmitter release. *Science* (2013) **339**, 421–5.
- 113. J. Leitz, C. Wang, L. Esquivies, R. A. Pfuetzner, J. J. Peters, S. Couoh-Cardel, A. L. Wang, A. T. Brunger, Beyond the MUN domain, Munc13 controls priming and depriming of synaptic vesicles. *Cell Rep* (2024) 43, 114026.
- 114. S. Wang, U. B. Choi, J. Gong, X. Yang, Y. Li, A. L. Wang, X. Yang, A. T. Brunger, C. Ma, Conformational change of syntaxin linker region induced by Munc13s initiates SNARE complex formation in synaptic exocytosis. *EMBO J* (2017) 36, 816–829.
- 115. C. Ma, W. Li, Y. Xu, J. Rizo, Munc13 mediates the transition from the closed syntaxin-Munc18 complex to the SNARE complex. *Nat Struct Mol Biol* (2011) **18**, 542–549.
- 116. S. Wang, Y. Li, J. Gong, S. Ye, X. Yang, R. Zhang, C. Ma, Munc18 and Munc13 serve as a functional template to orchestrate neuronal SNARE complex assembly. *Nat Commun* (2019) **10**, 69.
- 117. R. V. Kalyana Sundaram, H. Jin, F. Li, T. Shu, J. Coleman, J. Yang, F. Pincet, Y. Zhang, J. E. Rothman, S. S. Krishnakumar, Munc13 binds and recruits SNAP25 to chaperone SNARE complex assembly. *FEBS Lett* (2021) **595**, 297–309.
- 118. Q. Zhou, P. Zhou, A. L. Wang, D. Wu, M. Zhao, T. C. Südhof, A. T. Brunger, The primed SNARE-complexin-synaptotagmin complex for neuronal exocytosis. *Nature* (2017) **548**, 420–425.
- 119. Q. Zhou, Y. Lai, T. Bacaj, M. Zhao, A. Y. Lyubimov, M. Uervirojnangkoorn, O. B. Zeldin, A. S. Brewster, N. K. Sauter, A. E. Cohen, S. M. Soltis, R. Alonso-Mori, M. Chollet, H. T. Lemke, R. A. Pfuetzner, U. B. Choi, W. I. Weis, J. Diao, T. C. Südhof, A. T. Brunger, Architecture of the synaptotagmin-SNARE machinery for neuronal exocytosis. *Nature* (2015) 525, 62–7.
- 120. E. He, K. Wierda, R. van Westen, J. H. Broeke, R. F. Toonen, L. N. Cornelisse, M. Verhage, Munc13-1 and Munc18-1 together prevent NSF-dependent de-priming of synaptic vesicles. *Nat Commun* (2017) **8**, 15915.
- 121. E. A. Prinslow, K. P. Stepien, Y.-Z. Pan, J. Xu, J. Rizo, Multiple factors maintain assembled trans-SNARE complexes in the presence of NSF and αSNAP. *Elife* (2019) 8.
- 122. Z. P. Pang, T. C. Südhof, Cell biology of Ca2+-triggered exocytosis. *Curr Opin Cell Biol* (2010) **22**, 496–505.

- 123. N. Brose, K. Hofmann, Y. Hata, T. C. Südhof, Mammalian homologues of Caenorhabditis elegans unc-13 gene define novel family of C2-domain proteins. *J Biol Chem* (1995) **270**, 25273–80.
- 124. C. Rosenmund, A. Sigler, I. Augustin, K. Reim, N. Brose, J.-S. Rhee, Differential Control of Vesicle Priming and Short-Term Plasticity by Munc13 Isoforms. *Neuron* (2002) **33**, 411–424.
- 125. H. Kawabe, M. Mitkovski, P. S. Kaeser, J. Hirrlinger, F. Opazo, D. Nestvogel, S. Kalla, A. Fejtova, S. E. Verrier, S. R. Bungers, B. H. Cooper, F. Varoqueaux, Y. Wang, R. B. Nehring, E. D. Gundelfinger, C. Rosenmund, S. O. Rizzoli, T. C. Südhof, J.-S. Rhee, N. Brose, ELKS1 localizes the synaptic vesicle priming protein bMunc13-2 to a specific subset of active zones. *J Cell Biol* (2017) 216, 1143–1161.
- 126. A. Betz, P. Thakur, H. J. Junge, U. Ashery, J.-S. Rhee, V. Scheuss, C. Rosenmund, J. Rettig, N. Brose, Functional Interaction of the Active Zone Proteins Munc13-1 and RIM1 in Synaptic Vesicle Priming. *Neuron* (2001) **30**, 183–196.
- 127. J. Breustedt, A. Gundlfinger, F. Varoqueaux, K. Reim, N. Brose, D. Schmitz, Munc13-2 differentially affects hippocampal synaptic transmission and plasticity. *Cereb Cortex* (2010) **20**, 1109–20.
- 128. D. R. Stevens, Z.-X. Wu, U. Matti, H. J. Junge, C. Schirra, U. Becherer, S. M. Wojcik, N. Brose, J. Rettig, Identification of the minimal protein domain required for priming activity of Munc13-1. *Curr Biol* (2005) **15**, 2243–8.
- 129. J. Basu, N. Shen, I. Dulubova, J. Lu, R. Guan, O. Guryev, N. V Grishin, C. Rosenmund, J. Rizo, A minimal domain responsible for Munc13 activity. *Nat Struct Mol Biol* (2005) **12**, 1017–1018.
- 130. W. Li, C. Ma, R. Guan, Y. Xu, D. R. Tomchick, J. Rizo, The crystal structure of a Munc13 C-terminal module exhibits a remarkable similarity to vesicle tethering factors. *Structure* (2011) **19**, 1443–55.
- 131. M. Camacho, J. Basu, T. Trimbuch, S. Chang, C. Pulido-Lozano, S.-S. Chang, I. Duluvova, M. Abo-Rady, J. Rizo, C. Rosenmund, Heterodimerization of Munc13 C2A domain with RIM regulates synaptic vesicle docking and priming. *Nat Commun* (2017) 8, 15293.
- 132. J. Lu, M. Machius, I. Dulubova, H. Dai, T. C. Südhof, D. R. Tomchick, J. Rizo, Structural basis for a Munc13-1 homodimer to Munc13-1/RIM heterodimer switch. *PLoS Biol* (2006) **4**, e192.
- 133. L. Deng, P. S. Kaeser, W. Xu, T. C. Südhof, RIM Proteins Activate Vesicle Priming by Reversing Autoinhibitory Homodimerization of Munc13. *Neuron* (2011) **69**, 317–331.

- 134. B. Quade, M. Camacho, X. Zhao, M. Orlando, T. Trimbuch, J. Xu, W. Li, D. Nicastro, C. Rosenmund, J. Rizo, Membrane bridging by munc13-1 is crucial for neurotransmitter release. *Elife* (2019) **8**, 1–30.
- 135. L. Li, H. Liu, Q. Hall, W. Wang, Y. Yu, J. M. Kaplan, Z. Hu, A Hyperactive Form of unc-13 Enhances Ca2+ Sensitivity and Synaptic Vesicle Release Probability in C. elegans. *Cell Rep* (2019) **28**, 2979-2995.e4.
- 136. F. Michelassi, H. Liu, Z. Hu, J. S. Dittman, A C1-C2 Module in Munc13 Inhibits Calcium-Dependent Neurotransmitter Release. *Neuron* (2017) **95**, 577-590.e5.
- 137. J. Basu, A. Betz, N. Brose, C. Rosenmund, Munc13-1 C1 domain activation lowers the energy barrier for synaptic vesicle fusion. *J Neurosci* (2007) **27**, 1200–10.
- 138. A. Betz, U. Ashery, M. Rickmann, I. Augustin, E. Neher, T. C. Südhof, J. Rettig, N. Brose, Munc13-1 Is a Presynaptic Phorbol Ester Receptor that Enhances Neurotransmitter Release. *Neuron* (1998) **21**, 123–136.
- 139. X. Lou, V. Scheuss, R. Schneggenburger, Allosteric modulation of the presynaptic Ca2+ sensor for vesicle fusion. *Nature* (2005) **435**, 497–501.
- 140. J. S. Rhee, A. Betz, S. Pyott, K. Reim, F. Varoqueaux, I. Augustin, D. Hesse, T. C. Südhof, M. Takahashi, C. Rosenmund, N. Brose, Beta phorbol ester- and diacylglycerol-induced augmentation of transmitter release is mediated by Munc13s and not by PKCs. *Cell* (2002) **108**, 121–33.
- 141. O.-H. Shin, J. Lu, J.-S. Rhee, D. R. Tomchick, Z. P. Pang, S. M. Wojcik, M. Camacho-Perez, N. Brose, M. Machius, J. Rizo, C. Rosenmund, T. C. Südhof, Munc13 C2B domain is an activity-dependent Ca2+ regulator of synaptic exocytosis. *Nat Struct Mol Biol* (2010) 17, 280–8.
- 142. V. N. Murthy, C. F. Stevens, Reversal of synaptic vesicle docking at central synapses. *Nat Neurosci* (1999) **2**, 503–507.
- 143. H. Bao, D. Das, N. A. Courtney, Y. Jiang, J. S. Briguglio, X. Lou, D. Roston, Q. Cui, B. Chanda, E. R. Chapman, Dynamics and number of trans-SNARE complexes determine nascent fusion pore properties. *Nature* (2018) 554, 260–263.
- 144. E. Neher, N. Brose, Dynamically Primed Synaptic Vesicle States: Key to Understand Synaptic Short-Term Plasticity. *Neuron* (2018) **100**, 1283–1291.
- 145. A. Witkowska, L. P. Heinz, H. Grubmüller, R. Jahn, Tight docking of membranes before fusion represents a metastable state with unique properties. *Nat Commun* (2021) **12**, 3606.
- 146. H. Yavuz, I. Kattan, J. M. Hernandez, O. Hofnagel, A. Witkowska, S. Raunser, P. J. Walla, R. Jahn, Arrest of trans-SNARE zippering uncovers loosely and tightly docked intermediates in membrane fusion. *J Biol Chem* (2018) 293, 8645–8655.

- 147. G. F. Kusick, M. Chin, S. Raychaudhuri, K. Lippmann, K. P. Adula, E. J. Hujber, T. Vu, M. W. Davis, E. M. Jorgensen, S. Watanabe, Synaptic vesicles transiently dock to refill release sites. *Nat Neurosci* (2020) **23**, 1329–1338.
- 148. S. Chang, T. Trimbuch, C. Rosenmund, Synaptotagmin-1 drives synchronous Ca 2+ -triggered fusion by C 2 B-domain-mediated synaptic-vesicle-membrane attachment. *Nat Neurosci* (2018) **21**, 33–42.
- 149. C. Papantoniou, U. Laugks, J. Betzin, C. Capitanio, J. J. Ferrero, J. Sánchez-Prieto, S. Schoch, N. Brose, W. Baumeister, B. H. Cooper, C. Imig, V. Lučić, Munc13-and SNAP25-dependent molecular bridges play a key role in synaptic vesicle priming. *Sci Adv* (2023) **9**, eadf6222.
- 150. L. Maus, C. Lee, B. Altas, S. M. Sertel, K. Weyand, S. O. Rizzoli, J. Rhee, N. Brose, C. Imig, B. H. Cooper, Ultrastructural Correlates of Presynaptic Functional Heterogeneity in Hippocampal Synapses. *Cell Rep* (2020) **30**, 3632-3643.e8.
- 151. K.-H. Lin, H. Taschenberger, E. Neher, A sequential two-step priming scheme reproduces diversity in synaptic strength and short-term plasticity. *Proc Natl Acad Sci USA* (2022) **119**, e2207987119.
- 152. N. Brose, A. G. Petrenko, T. C. Südhof, R. Jahn, Synaptotagmin: a calcium sensor on the synaptic vesicle surface. *Science* (1992) **256**, 1021–5.
- 153. R. Fernández-Chacón, A. Königstorfer, S. H. Gerber, J. García, M. F. Matos, C. F. Stevens, N. Brose, J. Rizo, C. Rosenmund, T. C. Südhof, Synaptotagmin I functions as a calcium regulator of release probability. *Nature* (2001) 410, 41–49.
- 154. A. Maximov, T. C. Südhof, Autonomous function of synaptotagmin 1 in triggering synchronous release independent of asynchronous release. *Neuron* (2005) **48**, 547–54.
- 155. H. T. McMahon, M. Missler, C. Li, T. C. Südhof, Complexins: Cytosolic proteins that regulate SNAP receptor function. *Cell* (1995) **83**, 111–119.
- 156. K. Reim, M. Mansour, F. Varoqueaux, H. T. McMahon, T. C. Südhof, N. Brose, C. Rosenmund, Complexins regulate a late step in Ca2+-dependent neurotransmitter release. *Cell* (2001) **104**, 71–81.
- 157. J. Rizo, T. C. Südhof, C2-domains, structure and function of a universal Ca2+binding domain. *J Biol Chem* (1998) **273**, 15879–82.
- 158. W. Kuo, D. Z. Herrick, J. F. Ellena, D. S. Cafiso, The calcium-dependent and calcium-independent membrane binding of synaptotagmin 1: two modes of C2B binding. *J Mol Biol* (2009) **387**, 284–94.

- 159. J. Bai, W. C. Tucker, E. R. Chapman, PIP2 increases the speed of response of synaptotagmin and steers its membrane-penetration activity toward the plasma membrane. *Nat Struct Mol Biol* (2004) **11**, 36–44.
- 160. M. Geppert, Y. Goda, R. E. Hammer, C. Li, T. W. Rosahl, C. F. Stevens, T. C. Südhof, Synaptotagmin I: A major Ca2+ sensor for transmitter release at a central synapse. *Cell* (1994) **79**, 717–727.
- 161. S. Wang, Y. Li, C. Ma, Synaptotagmin-1 C2B domain interacts simultaneously with SNAREs and membranes to promote membrane fusion. *Elife* (2016) **5**.
- 162. F. J. López-Murcia, K. Reim, H. Taschenberger, Complexins: Ubiquitously Expressed Presynaptic Regulators of SNARE-Mediated Synaptic Vesicle Fusion. *Adv Neurobiol* (2023) **33**, 255–285.
- 163. E. Toulmé, A. Salazar Lázaro, T. Trimbuch, J. Rizo, C. Rosenmund, Neurotransmitter release is triggered by a calcium-induced rearrangement in the Synaptotagmin-1/SNARE complex primary interface. *Proc Natl Acad Sci U S A* (2024) **121**, e2409636121.
- 164. S. Pabst, M. Margittai, D. Vainius, R. Langen, R. Jahn, D. Fasshauer, Rapid and selective binding to the synaptic SNARE complex suggests a modulatory role of complexins in neuroexocytosis. *J Biol Chem* (2002) **277**, 7838–48.
- X. Chen, D. R. Tomchick, E. Kovrigin, D. Araç, M. Machius, T. C. Südhof, J. Rizo, Three-Dimensional Structure of the Complexin/SNARE Complex. *Neuron* (2002) 33, 397–409.
- 166. M. Xue, A. Stradomska, H. Chen, N. Brose, W. Zhang, C. Rosenmund, K. Reim, Complexins facilitate neurotransmitter release at excitatory and inhibitory synapses in mammalian central nervous system. *Proc Natl Acad Sci U S A* (2008) 105, 7875–80.
- 167. M. Xue, T. K. Craig, J. Xu, H. T. Chao, J. Rizo, C. Rosenmund, Binding of the complexin N terminus to the SNARE complex potentiates synaptic-vesicle fusogenicity. *Nat Struct Mol Biol* (2010) **17**, 568–575.
- 168. S. Huntwork, J. T. Littleton, A complexin fusion clamp regulates spontaneous neurotransmitter release and synaptic growth. *Nat Neurosci* (2007) **10**, 1235–1237.
- 169. J. Tang, A. Maximov, O. H. Shin, H. Dai, J. Rizo, T. C. Südhof, A Complexin/Synaptotagmin 1 Switch Controls Fast Synaptic Vesicle Exocytosis. *Cell* (2006) **126**, 1175–1187.
- 170. J. R. Schaub, X. Lu, B. Doneske, Y. K. Shin, J. A. McNew, Hemifusion arrest by complexin is relieved by Ca2+-synaptotagmin I. *Nat Struct Mol Biol* (2006) **13**, 748–750.

- 171. C. G. Giraudo, W. S. Eng, T. J. Melia, J. E. Rothman, A clamping mechanism involved in SNARE-dependent exocytosis. *Science* (2006) **313**, 676–80.
- 172. Z.-W. Wang, S. Riaz, L. Niu, Roles and Sources of Calcium in Synaptic Exocytosis. *Adv Neurobiol* (2023) **33**, 139–170.
- 173. L. Lacinová, Voltage-dependent calcium channels. *Gen Physiol Biophys* (2005) **24 Suppl 1**, 1–78.
- 174. E. A. Ertel, K. P. Campbell, M. M. Harpold, F. Hofmann, Y. Mori, E. Perez-Reyes, A. Schwartz, T. P. Snutch, T. Tanabe, L. Birnbaumer, R. W. Tsien, W. A. Catterall, Nomenclature of Voltage-Gated Calcium Channels. *Neuron* (2000) **25**, 533–535.
- 175. D. B. Wheeler, A. Randall, R. W. Tsien, Roles of N-type and Q-type Ca2+ channels in supporting hippocampal synaptic transmission. *Science* (1994) **264**, 107–11.
- 176. T. Takahashi, A. Momiyama, Different types of calcium channels mediate central synaptic transmission. *Nature* (1993) **366**, 156–158.
- 177. L. G. Wu, P. Saggau, Pharmacological identification of two types of presynaptic voltage-dependent calcium channels at CA3-CA1 synapses of the hippocampus. *J Neurosci* (1994) **14**, 5613–22.
- 178. J. I. Luebke, K. Dunlap, T. J. Turner, Multiple calcium channel types control glutamatergic synaptic transmission in the hippocampus. *Neuron* (1993) **11**, 895–902.
- 179. S. Iwasaki, T. Takahashi, Developmental changes in calcium channel types mediating synaptic transmission in rat auditory brainstem. *J Physiol* (1998) **509**, 419–423.
- 180. R. Khanna, A. Zougman, E. F. Stanley, A Proteomic Screen for Presynaptic Terminal N-type Calcium Channel (CaV2.2) Binding Partners. *BMB Rep* (2007) **40**, 302–314.
- 181. T. Coppola, S. Magnin-Luthi, V. Perret-Menoud, S. Gattesco, G. Schiavo, R. Regazzi, Direct interaction of the Rab3 effector RIM with Ca2+ channels, SNAP-25, and synaptotagmin. *J Biol Chem* (2001) **276**, 32756–62.
- 182. H. Hibino, R. Pironkova, O. Onwumere, M. Vologodskaia, A. J. Hudspeth, F. Lesage, RIM Binding Proteins (RBPs) Couple Rab3-Interacting Molecules (RIMs) to Voltage-Gated Ca2+ Channels. *Neuron* (2002) **34**, 411–423.
- 183. M. Silva, V. Tran, A. Marty, Calcium-dependent docking of synaptic vesicles. *Trends Neurosci* (2021) **44**, 579–592.

- 184. R. Fernández-Busnadiego, B. Zuber, U. E. Maurer, M. Cyrklaff, W. Baumeister, V. Lucic, Quantitative analysis of the native presynaptic cytomatrix by cryoelectron tomography. *J Cell Biol* (2010) **188**, 145–56.
- 185. H. J. Koester, D. Johnston, Target cell-dependent normalization of transmitter release at neocortical synapses. *Science* (2005) **308**, 863–6.
- 186. T. Éltes, T. Kirizs, Z. Nusser, N. Holderith, Target Cell Type-Dependent Differences in Ca2+ Channel Function Underlie Distinct Release Probabilities at Hippocampal Glutamatergic Terminals. *J Neurosci* (2017) 37, 1910–1924.
- 187. R. Shigemoto, A. Kulik, J. D. B. Roberts, H. Ohishi, Z. Nusser, T. Kaneko, P. Somogyi, Target-cell-specific concentration of a metabotropic glutamate receptor in the presynaptic active zone. *Nature* (1996) **381**, 523–525.
- 188. A. Losonczy, P. Somogyi, Z. Nusser, Reduction of excitatory postsynaptic responses by persistently active metabotropic glutamate receptors in the hippocampus. *J Neurophysiol* (2003) **89**, 1910–1919.
- 189. N. H. Tomioka, H. Yasuda, H. Miyamoto, M. Hatayama, N. Morimura, Y. Matsumoto, T. Suzuki, M. Odagawa, Y. S. Odaka, Y. Iwayama, J. Won Um, J. Ko, Y. Inoue, S. Kaneko, S. Hirose, K. Yamada, T. Yoshikawa, K. Yamakawa, J. Aruga, Elfn1 recruits presynaptic mGluR7 in trans and its loss results in seizures. *Nat Commun* (2014) 5.
- 190. T. J. Stachniak, E. L. Sylwestrak, P. Scheiffele, B. J. Hall, A. Ghosh, Elfn1-Induced Constitutive Activation of mGluR7 Determines Frequency-Dependent Recruitment of Somatostatin Interneurons. *J Neurosci* (2019) **39**, 4461–4474.
- 191. T. C. Südhof, The presynaptic active zone. Neuron (2012) 75, 11–25.
- 192. K. N. M. Man, C. Imig, A. M. Walter, P. S. Pinheiro, D. R. Stevens, J. Rettig, J. B. Sørensen, B. H. Cooper, N. Brose, S. M. Wojcik, Identification of a Munc13-sensitive step in chromaffin cell large dense-core vesicle exocytosis. *Elife* (2015) 4.
- 193. B. Cooper, M. Hemmerlein, J. Ammermüller, C. Imig, K. Reim, N. Lipstein, S. Kalla, H. Kawabe, N. Brose, J. H. Brandstätter, F. Varoqueaux, Munc13-independent vesicle priming at mouse photoreceptor ribbon synapses. *J Neurosci* (2012) **32**, 8040–52.
- 194. F. A. Dodge, R. Rahamimoff, Co-operative action of calcium ions in transmitter release at the neuromuscular junction. *J Physiol* (1967) **193**, 419–432.
- 195. Y. Nakamura, H. Harada, N. Kamasawa, K. Matsui, J. S. Rothman, R. Shigemoto, R. A. Silver, D. A. DiGregorio, T. Takahashi, Nanoscale distribution of presynaptic

- Ca(2+) channels and its impact on vesicular release during development. *Neuron* (2015) **85**, 145–158.
- 196. N. Rebola, M. Reva, T. Kirizs, M. Szoboszlay, A. Lőrincz, G. Moneron, Z. Nusser, D. A. DiGregorio, Distinct Nanoscale Calcium Channel and Synaptic Vesicle Topographies Contribute to the Diversity of Synaptic Function. *Neuron* (2019) 104, 693-710.e9.
- 197. G. Malagon, T. Miki, V. Tran, L. Gomez, A. Marty, Incomplete vesicular docking limits synaptic strength under high release probability conditions. *Elife* (2020) **9**, 1–18.
- 198. E. Neher, Some Subtle Lessons from the Calyx of Held Synapse. *Biophys J* (2017) **112**, 215–223.
- 199. D. M. Quastel, The binomial model in fluctuation analysis of quantal neurotransmitter release. *Biophys J* (1997) **72**, 728–53.
- 200. B. Pan, R. S. Zucker, A General Model of Synaptic Transmission and Short-Term Plasticity. *Neuron* (2009) **62**, 539–554.
- 201. E. Hanse, B. Gustafsson, Vesicle release probability and pre-primed pool at glutamatergic synapses in area CA1 of the rat neonatal hippocampus. *J Physiol* (2001) **531**, 481–93.
- 202. T. Miki, G. Malagon, C. Pulido, I. Llano, E. Neher, A. Marty, Actin- and Myosin-Dependent Vesicle Loading of Presynaptic Docking Sites Prior to Exocytosis. *Neuron* (2016) **91**, 808–823.
- 203. F. Doussau, H. Schmidt, K. Dorgans, A. M. Valera, B. Poulain, P. Isope, Frequency-dependent mobilization of heterogeneous pools of synaptic vesicles shapes presynaptic plasticity. *Elife* (2017) **6**, 1–24.
- 204. T. Miki, Y. Nakamura, G. Malagon, E. Neher, A. Marty, Two-component latency distributions indicate two-step vesicular release at simple glutamatergic synapses. *Nat Commun* (2018) **9**.
- 205. H. Taschenberger, A. Woehler, E. Neher, Superpriming of synaptic vesicles as a common basis for intersynapse variability and modulation of synaptic strength. *Proc Natl Acad Sci U S A* (2016) **113**, E4548-57.
- 206. M. Müller, J. D. Goutman, O. Kochubey, R. Schneggenburger, Interaction between facilitation and depression at a large CNS synapse reveals mechanisms of short-term plasticity. *Journal of Neuroscience* (2010) **30**, 2007–2016.
- 207. C. Pulido, A. Marty, A two-step docking site model predicting different short-term synaptic plasticity patterns. *J Gen Physiol* (2018) **150**, 1107–1124.

- 208. E. Neher, Interpretation of presynaptic phenotypes of synaptic plasticity in terms of a two-step priming process. *J Gen Physiol* (2024) **156**.
- 209. L. E. Fenno, J. Mattis, C. Ramakrishnan, M. Hyun, S. Y. Lee, M. He, J. Tucciarone, A. Selimbeyoglu, A. Berndt, L. Grosenick, K. A. Zalocusky, H. Bernstein, H. Swanson, C. Perry, I. Diester, F. M. Boyce, C. E. Bass, R. Neve, Z. J. Huang, K. Deisseroth, Targeting cells with single vectors using multiple-feature Boolean logic. *Nat Methods* (2014) 11, 763–72.
- 210. M. Aldahabi, F. Balint, N. Holderith, A. Lorincz, M. Reva, Z. Nusser, Different priming states of synaptic vesicles underlie distinct release probabilities at hippocampal excitatory synapses. *Neuron* (2022) **110**, 4144-4161.e7.
- 211. N. Holderith, J. Heredi, V. Kis, Z. Nusser, A High-Resolution Method for Quantitative Molecular Analysis of Functionally Characterized Individual Synapses. *Cell Rep* (2020) **32**, 107968.
- 212. N. Holderith, M. Aldahabi, Z. Nusser, Selective Enrichment of Munc13-2 in Presynaptic Active Zones of Hippocampal Pyramidal Cells That Innervate mGluR1α Expressing Interneurons. *Front Synaptic Neurosci* (2022) **13**, 773209.
- 213. M. R. Karlocai, J. Heredi, T. Benedek, N. Holderith, A. Lorincz, Z. Nusser, Variability in the Munc13-1 content of excitatory release sites. *Elife* (2021) **10**.
- 214. S. Reddy-Alla, M. A. Böhme, E. Reynolds, C. Beis, A. T. Grasskamp, M. M. Mampell, M. Maglione, M. Jusyte, U. Rey, H. Babikir, A. W. McCarthy, C. Quentin, T. Matkovic, D. D. Bergeron, Z. Mushtaq, F. Göttfert, D. Owald, T. Mielke, S. W. Hell, S. J. Sigrist, A. M. Walter, Stable Positioning of Unc13 Restricts Synaptic Vesicle Fusion to Defined Release Sites to Promote Synchronous Neurotransmission. *Neuron* (2017) 95, 1350-1364.e12.
- 215. H. Sakamoto, T. Ariyoshi, N. Kimpara, K. Sugao, I. Taiko, K. Takikawa, D. Asanuma, S. Namiki, K. Hirose, Synaptic weight set by Munc13-1 supramolecular assemblies. *Nat Neurosci* (2018) **21**, 41–55.
- 216. Y. P. Tan, I. Llano, Modulation by K+ channels of action potential-evoked intracellular Ca2+ concentration rises in rat cerebellar basket cell axons. *J Physiol* (1999) **520 Pt 1**, 65–78.
- 217. F. Ferraguti, T. Klausberger, P. Cobden, A. Baude, J. D. B. Roberts, P. Szucs, A. Kinoshita, R. Shigemoto, P. Somogyi, Y. Dalezios, Metabotropic glutamate receptor 8-expressing nerve terminals target subsets of GABAergic neurons in the hippocampus. *Journal of Neuroscience* (2005) **25**, 10520–10536.
- 218. T. C. Südhof, J. Rizo, Synaptic vesicle exocytosis. *Cold Spring Harb Perspect Biol* (2011) **3**.

- 219. P. S. Kaeser, L. Deng, Y. Wang, I. Dulubova, X. Liu, J. Rizo, T. C. Südhof, RIM proteins tether Ca2+ channels to presynaptic active zones via a direct PDZ-domain interaction. *Cell* (2011) **144**, 282–295.
- 220. M. M. Brockmann, M. Maglione, C. G. Willmes, A. Stumpf, B. A. Bouazza, L. M. Velasquez, M. K. Grauel, P. Beed, M. Lehmann, N. Gimber, J. Schmoranzer, S. J. Sigrist, C. Rosenmund, D. Schmitz, RIM-BP2 primes synaptic vesicles via recruitment of Munc13-1 at hippocampal mossy fiber synapses. *Elife* (2019) 8.
- 221. Y. Wang, M. Okamoto, F. Schmitz, K. Hofmann, T. C. Südhof, Rim is a putative Rab3 effector in regulating synaptic-vesicle fusion. *Nature* (1997) **388**, 593–8.
- 222. M. M. Brockmann, F. Zarebidaki, M. Camacho, M. K. Grauel, T. Trimbuch, T. C. Südhof, C. Rosenmund, A Trio of Active Zone Proteins Comprised of RIM-BPs, RIMs, and Munc13s Governs Neurotransmitter Release. *Cell Rep* (2020) 32, 107960.
- 223. S. Schoch, P. E. Castillo, T. Jo, K. Mukherjee, M. Geppert, Y. Wang, F. Schmitz, R. C. Malenka, T. C. Südhof, RIM1α forms a protein scaffold for regulating neurotransmitter release at the active zone. *Nature* (2002) **415**, 321–326.
- 224. Y. S. Andrews-Zwilling, H. Kawabe, K. Reim, F. Varoqueaux, N. Brose, Binding to Rab3A-interacting molecule RIM regulates the presynaptic recruitment of Munc13-1 and ubMunc13-2. *J Biol Chem* (2006) **281**, 19720–31.
- 225. I. Augustin, A. Betz, C. Herrmann, T. Jo, N. Brose, Differential expression of two novel Munc13 proteins in rat brain. *Biochem J* (1999) **337** (**Pt 3**), 363–71.
- 226. R. van de Bospoort, M. Farina, S. K. Schmitz, A. de Jong, H. de Wit, M. Verhage, R. F. Toonen, Munc13 controls the location and efficiency of dense-core vesicle release in neurons. *Journal of Cell Biology* (2012) **199**, 883–891.
- 227. Z. Chen, B. Cooper, S. Kalla, F. Varoqueaux, S. M. Young, The Munc13 proteins differentially regulate readily releasable pool dynamics and calcium-dependent recovery at a central synapse. *J Neurosci* (2013) **33**, 8336–51.
- 228. D. A. Gioia, N. J. Alexander, B. A. McCool, Differential Expression of Munc13-2 Produces Unique Synaptic Phenotypes in the Basolateral Amygdala of C57BL/6J and DBA/2J Mice. *J Neurosci* (2016) **36**, 10964–10977.
- 229. A. G. Millar, H. Bradacs, M. P. Charlton, H. L. Atwood, Inverse relationship between release probability and readily releasable vesicles in depressing and facilitating synapses. *J Neurosci* (2002) **22**, 9661–7.
- 230. A. G. Millar, R. S. Zucker, G. C. R. Ellis-Davies, M. P. Charlton, H. L. Atwood, Calcium sensitivity of neurotransmitter release differs at phasic and tonic synapses. *J Neurosci* (2005) **25**, 3113–25.

- 231. N. Holderith, A. Lorincz, G. Katona, B. Rózsa, A. Kulik, M. Watanabe, Z. Nusser, Release probability of hippocampal glutamatergic terminals scales with the size of the active zone. *Nat Neurosci* (2012) **15**, 988–997.
- 232. A. Kulik, K. Nakadate, A. Hagiwara, Y. Fukazawa, R. Luján, H. Saito, N. Suzuki, A. Futatsugi, K. Mikoshiba, M. Frotscher, R. Shigemoto, Immunocytochemical localization of the alpha 1A subunit of the P/Q-type calcium channel in the rat cerebellum. *Eur J Neurosci* (2004) **19**, 2169–78.
- 233. D. W. Indriati, N. Kamasawa, K. Matsui, A. L. Meredith, M. Watanabe, R. Shigemoto, Quantitative localization of Cav2.1 (P/Q-type) voltage-dependent calcium channels in Purkinje cells: somatodendritic gradient and distinct somatic coclustering with calcium-activated potassium channels. *J Neurosci* (2013) 33, 3668–78.
- 234. I. Bucurenciu, A. Kulik, B. Schwaller, M. Frotscher, P. Jonas, Nanodomain coupling between Ca2+ channels and Ca2+ sensors promotes fast and efficient transmitter release at a cortical GABAergic synapse. *Neuron* (2008) **57**, 536–45.
- 235. M. Lübbert, R. O. Goral, C. Keine, C. Thomas, D. Guerrero-Given, T. Putzke, R. Satterfield, N. Kamasawa, S. M. Young, Ca V 2.1 α 1 Subunit Expression Regulates Presynaptic Ca V 2.1 Abundance and Synaptic Strength at a Central Synapse. *Neuron* (2019) **101**, 260-273.e6.
- 236. S. J. Gratz, P. Goel, J. J. Bruckner, R. X. Hernandez, K. Khateeb, G. T. Macleod, D. Dickman, K. M. O'Connor-Giles, Endogenous Tagging Reveals Differential Regulation of Ca2+ Channels at Single Active Zones during Presynaptic Homeostatic Potentiation and Depression. *J Neurosci* (2019) **39**, 2416–2429.
- 237. Z. L. Newman, D. Bakshinskaya, R. Schultz, S. J. Kenny, S. Moon, K. Aghi, C. Stanley, N. Marnani, R. Li, J. Bleier, K. Xu, E. Y. Isacoff, Determinants of synapse diversity revealed by super-resolution quantal transmission and active zone imaging. *Nat Commun* (2022) **13**, 229.
- 238. Y. Akbergenova, K. L. Cunningham, Y. V Zhang, S. Weiss, J. T. Littleton, Characterization of developmental and molecular factors underlying release heterogeneity at Drosophila synapses. *Elife* (2018) 7.
- 239. M. Wölfel, X. Lou, R. Schneggenburger, A mechanism intrinsic to the vesicle fusion machinery determines fast and slow transmitter release at a large CNS synapse. *J Neurosci* (2007) **27**, 3198–210.
- 240. J. Rizo, Mechanism of neurotransmitter release coming into focus. *Protein Sci* (2018) **27**, 1364–1391.

- 241. G. B. Awatramani, G. D. Price, L. O. Trussell, Modulation of transmitter release by presynaptic resting potential and background calcium levels. *Neuron* (2005) **48**, 109–121.
- 242. A. Fekete, Y. Nakamura, Y. M. Yang, S. Herlitze, M. D. Mark, D. A. DiGregorio, L. Y. Wang, Underpinning heterogeneity in synaptic transmission by presynaptic ensembles of distinct morphological modules. *Nat Commun* (2019) **10**.
- 243. T. Takahashi, I. D. Forsythe, T. Tsujimoto, M. Barnes-Davies, K. Onodera, Presynaptic calcium current modulation by a metabotropic glutamate receptor. *Science* (1996) **274**, 594–7.
- 244. E. Hanse, B. Gustafsson, Factors explaining heterogeneity in short-term synaptic dynamics of hippocampal glutamatergic synapses in the neonatal rat. *J Physiol* (2001) **537**, 141–9.
- 245. I. Weichard, H. Taschenberger, F. Gsell, G. Bornschein, A. Ritzau-Jost, H. Schmidt, R. J. Kittel, J. Eilers, E. Neher, S. Hallermann, J. Nerlich, Fully-primed slowly-recovering vesicles mediate presynaptic LTP at neocortical neurons. *Proc Natl Acad Sci U S A* (2023) 120, e2305460120.
- 246. R. Martín, N. García-Font, A. S. Suárez-Pinilla, D. Bartolomé-Martín, J. J. Ferrero, R. Luján, M. Torres, J. Sánchez-Prieto, β-Adrenergic Receptors/Epac Signaling Increases the Size of the Readily Releasable Pool of Synaptic Vesicles Required for Parallel Fiber LTP. *J Neurosci* (2020) 40, 8604–8617.
- 247. D. N. Chiu, B. C. Carter, Synaptotagmin 7 Sculpts Short-Term Plasticity at a High Probability Synapse. *J Neurosci* (2024) **44**, e1756232023.
- 248. J. Turecek, S. L. Jackman, W. G. Regehr, Synaptic Specializations Support Frequency-Independent Purkinje Cell Output from the Cerebellar Cortex. *Cell Rep* (2016) **17**, 3256–3268.
- 249. Z. Wu, G. F. Kusick, M. M. M. Berns, S. Raychaudhuri, K. Itoh, A. M. Walter, E. R. Chapman, S. Watanabe, Synaptotagmin 7 docks synaptic vesicles to support facilitation and Doc2α-triggered asynchronous release. *Elife* (2024) **12**.
- 250. M. Camacho, B. Quade, T. Trimbuch, J. Xu, L. Sari, J. Rizo, C. Rosenmund, Control of neurotransmitter release by two distinct membrane-binding faces of the munc13-1 c1c2b region. *Elife* (2021) **10**, 1–34.
- 251. M. E. Larkum, J. J. Zhu, B. Sakmann, A new cellular mechanism for coupling inputs arriving at different cortical layers. *Nature* (1999) **398**, 338–341.
- 252. M. Murayama, E. Pérez-Garci, T. Nevian, T. Bock, W. Senn, M. E. Larkum, Dendritic encoding of sensory stimuli controlled by deep cortical interneurons. *Nature* (2009) **457**, 1137–1141.

- 253. G. Silberberg, H. Markram, Disynaptic Inhibition between Neocortical Pyramidal Cells Mediated by Martinotti Cells. *Neuron* (2007) **53**, 735–746.
- 254. K. A. Buchanan, A. V. Blackman, A. W. Moreau, D. Elgar, R. P. Costa, T. Lalanne, A. A. Tudor Jones, J. Oyrer, P. J. Sjöström, Target-Specific Expression of Presynaptic NMDA Receptors in Neocortical Microcircuits. *Neuron* (2012) **75**, 451–466.
- 255. A. V Blackman, T. Abrahamsson, R. P. Costa, T. Lalanne, P. J. Sjöström, Target-cell-specific short-term plasticity in local circuits. *Front Synaptic Neurosci* (2013) 5, 11.

9. BIBLIOGRAPHY OF PUBLICATIONS

9.1. Publications Related to the Thesis:

- Holderith, N., Aldahabi, M., & Nusser, Z. (2022). Selective Enrichment of Munc13-2 in Presynaptic Active Zones of Hippocampal Pyramidal Cells That Innervate mGluR1α Expressing Interneurons. Frontiers in Synaptic Neuroscience, 13. https://doi.org/10.3389/fnsyn.2021.773209
- Aldahabi, M., Balint, F., Holderith, N., Lorincz, A., Reva, M., & Nusser, Z. (2022). Different priming states of synaptic vesicles underlie distinct release probabilities at hippocampal excitatory synapses. Neuron, 110(24), 4144-4161.e7. https://doi.org/10.1016/j.neuron.2022.09.035
- Aldahabi, M., Neher, E., & Nusser, Z. (2024). Different states of synaptic vesicle priming explain target cell type-dependent differences in neurotransmitter release. Proceedings of the National Academy of Sciences of the United States of America, 121(18). https://doi.org/10.1073/pnas.2322550121

9.2. Publications Not Related to the Thesis:

- Heredi, J., Olah, G., Sumegi, M., Paul Lukacs, I., Aldahabi, M., Újfalussy, B. B., Makara, J. K., & Nusser, Z. (2025). Increased excitatory synapse size in hippocampal place cells compared to silent cells. Proceedings of the National Academy of Sciences, 122(23). https://doi.org/10.1073/pnas.2505322122
- Alzghoul, L., Abdelhamid, S. S., Yanis, A. H., Qwaider, Y. Z., Aldahabi, M., & Albdour, S. A. (2019). The association between levels of inflammatory markers in autistic children compared to their unaffected siblings and unrelated healthy controls. Turkish Journal of Medical Sciences, 49(4). https://doi.org/10.3906/sag-1812-16

10. ACKNOWLEDGMENTS

I would like to thank the contribution of my colleagues: Dr Noemi Holderith performed all immunolocalization experiments for data presented in Figures 7-9, the in vitro 2P imaging experiments (Figure 15), and the EM tomography work (Figure 18). Dr Andrea Lorincz conducted the SDS-FRL experiments and analysed her data using scripts written by Maria Reva (Figures 12 & 13). Flora Balint performed the *in vitro* paired recordings for data presented in Figure 16. Erwin Neher provided guide to the modelling presented in Figures 19 and 21. All remaining data presented in this work were conducted by Mohammad Aldahabi.

I thank Dóra Ronaszéki and Éva Dobai for their excellent technical assistance. I would also like to thank Dr Eszter Sipos and Bence Kókay for their help with the virus injection.